DEPARTMENT OF PHYSICS
UNIVERSITY OF JYVÄSKYLÄ
RESEARCH REPORT No. 8/2013

Development of the recoil-beta tagging method and recoil-beta tagging studies of ^{66}As and ^{66}Se

by

Panu Ruotsalainen

Academic Dissertation
for the Degree of
Doctor of Philosophy

To be presented, by permission of the
Faculty of Mathematics and Science
of the University of Jyväskylä,
for public examination in Auditorium FYS-1 of the
University of Jyväskylä on October 25, 2013
at 12 o'clock noon

Jyväskylä, Finland
October 2013

Abstract

Ruotsalainen, Panu
Development of the recoil-beta tagging method and recoil-beta tagging studies of ^{66}As and ^{66}Se
Jyväskylä: University of Jyväskylä, 2013, 137 p.
Department of Physics Research Report No. 8/2013
ISSN: 0075-465X; 8/2013
ISBN: 978-951-39-5416-1 (paper version)
ISBN: 978-951-39-5417-8 (electronic version)
Diss.

The structure of self-conjugate odd-odd $N = Z$ nucleus ^{66}As has been experimentally studied in detail. Prompt and isomeric excited states have been observed utilising recoil-β tagging and recoil-isomer tagging methods. Most importantly, candidates for the excited states in the $T = 1$ band were identified up to spin $J^\pi = 6^+$. Three new detectors *i.e.,* a charged-particle veto detector, a highly-pixelated DSSD and a phosphor sandwich device have been constructed and tested to enhance the sensitivity of the recoil-β tagging approach. The newly developed charged-particle veto detector in conjunction with the recoil-β tagging allowed excited states in the exotic neutron-deficient $N = Z - 2$ nucleus ^{66}Se to be identified up to spin $J^\pi = 6^+$. The newly obtained spectroscopic results both in ^{66}As and ^{66}Se permitted the derivation of energy differences between isobaric analogue states in the full $A = 66$ triplet. These results show that both the charge-symmetry and charge-independence characteristics of the strong nucleon-nucleon interaction are violated. Moreover, the experimental energy differences are larger than predicted by the shell-model calculations. This points towards a need for an additional isospin non-conserving interaction, whose fundamental origin cannot be explained on the basis of existing nuclear models.

Keywords: medium-mass nuclei, Coulomb energy differences, isospin-symmetry breaking, recoil-β tagging

Author's address Panu Ruotsalainen
Department of Physics
University of Jyväskylä
Finland

Supervisors Dr. Catherine Scholey
Department of Physics
University of Jyväskylä
Finland

Prof. Rauno Julin
Department of Physics
University of Jyväskylä
Finland

Reviewers Prof. Andreas Görgen
Department of Physics
The Faculty of Mathematics and Natural Sciences
University of Oslo
Norway

Dr. John F. Smith
School of Engineering
University of the West of Scotland
United Kingdom

Opponent Dr. Dariusz Seweryniak
Physics Division
Argonne National Laboratory
United States

Preface

This work has been carried out at the Accelerator Laboratory of the Department of Physics, University of Jyväskylä, Finland from 2008 to 2013. Financial support from the Magnus Ehrnrooth foundation, the Graduate School for Particle and Nuclear Physics and the University of Jyväskylä is gratefully acknowledged.

I want to thank my supervisor Dr. Catherine Scholey for guidance and support during the years of my PhD project and for the numerous common hours in the laboratory running experiments. It has certainly been fun! I want to also thank my other supervisor Professor Rauno Julin for accepting me in the research group as a summer student at first in 2006 and finally as a PhD student in 2008 along with his positive and encouraging attitude towards students. I would also like to thank Rauno for introducing me running and guitarism. I want to express my gratitude to Dr. Juha Uusitalo who has taught me a good lesson of nuclear physics.

Every soul of the Gamma-RITU group has contributed to this work in one way or the another, so you all deserve a warm thankyou. I'm especially grateful to my peers Mr. Pauli Peura and Ms. Ulrika Jakobsson, who have provided their valuable help related to physics, analysis, computers, paper publishing and many other everyday issues at work. I want to thank the former group members Dr. Pete Jones, Dr. Markus Nyman and Dr. Steffen Ketelhut for providing me with a basic schooling in γ-ray detection. I have been privileged to share the duties of the Swedish Consulate with the most cultivated and nicest person on earth. Thank you Mikael for the hilarious office hours and introducing me to the masterpieces of Eddie Meduza. Dr. Panu Rahkila is gratefully acknowledged for helping me acquire the laptop computer, which has been intensively used to prepare this thesis.

The major contributors of this work are the York colleagues Professor Bob Wadsworth, Professor Michael Bentley, Dr. David Jenkins and Mr. Jack Henderson. Without your ideas, comments and input this thesis would not exist. Thank you so much.

The boys of Holvi - Aki, Alex, Antti, Hannu, Ilkka, Jalmari, Joni, Jukka, Matti, Perttu, Timo, Tuomas, Ville and Ville, thank you all for the lunch breaks and fantastic conference cruises. I want to thank all my ice hockey and band mates for the common rehearsals, games and gigs, which have taken my thoughts away from work. My dear long-time friends Aleksi, Riku, Antti, Juho, Pekka and Olli, thank you for your sincere friendship and support.

Kiitokset isälle, äitille ja veli Pirkalle tuesta kaikkina näinä vuosina. En olisi päässyt tänne asti ilman teitä. Rakkaille Soilelle ja Sennille suurin kiitos kaikesta.

Panu Ruotsalainen,
Jyväskylä, October 2013

List of publications

This thesis is based on the contents of publications 1, 2 and 3. The author has also contributed to the experimental part of publications 4-35, which have employed the recoil tagging methods (except publication 6).

1. **P. Ruotsalainen**, C. Scholey, R. Julin, K. Hauschild, K. Kaneko, B.S. Nara Singh, R. Wadsworth, D.G. Jenkins, T.S Brock, P.T. Greenlees, J. Henderson, U. Jakobsson, P. Jones, S. Juutinen, S. Ketelhut, M. Leino, N.M Lumley, P.J.R. Mason, P. Nieminen, M. Nyman, I. Paterson, P. Peura, M.G Procter, P. Rahkila, J. Sarén, J. Sorri and J. Uusitalo
Recoil-β tagging study of the $N = Z$ nucleus ^{66}As
Phys. Rev. C **88**, 024320 (2013)

2. **P. Ruotsalainen**, D.G. Jenkins, M.A. Bentley, R. Wadsworth, C. Scholey, P. Joshi, P.J. Davies, J. Henderson, K. Auranen, T. Grahn, P.T. Greenlees, A. Herzáň, U. Jakobsson, R. Julin, S. Juutinen, J. Konki, M. Leino, G. Lotay, A.J. Nichols, A. Obertelli, J. Pakarinen, J. Partanen, P. Peura, P. Rahkila, M. Sandzelius, J. Sarén, J. Sorri, S. Stolze and J. Uusitalo
Spectroscopy of proton-rich ^{66}Se up to $J^{\pi} = 6^{+}$: isospin-breaking effect in the $A = 66$ isobaric triplet
Accepted for publication as a Rapid Communication in Phys. Rev. C (2013)

3. J. Henderson, **P. Ruotsalainen**, D.G. Jenkins, C. Scholey, K. Auranen, P.J. Davies, T. Grahn, P.T. Greenlees, T.W. Henry, A. Herzáň, U. Jakobsson, P. Joshi, R. Julin, S. Juutinen, J. Konki, M. Leino, G. Lotay, A.J. Nichols, A. Obertelli, J. Pakarinen, J. Partanen, P. Peura, P. Rahkila, M. Sandzelius, J. Sarén, J. Sorri, S. Stolze, J. Uusitalo and R. Wadsworth
Enhancing the sensitivity of recoil-beta tagging
J. Inst. **8**, P04025 (2013)

4. A. Vancraeyenest, C.M. Petrache, D. Guinet, P.T. Greenlees, U. Jakobsson, R. Julin, S. Juutinen, S. Ketelhut, M. Leino, M. Nyman, P. Peura, P. Rahkila, **P. Ruotsalainen**, J. Sarén, C. Scholey, J. Sorri, J. Uusitalo, P. Jones, C. Ducoin, P. Lautesse, C. Mancuso, N. Redon, O. Stezowski, P. Désesquelles, R. Leguillon, A. Korichi, T. Zerrouki, D. Curien and A. Takashima
Identification of new transitions feeding the high-spin isomers in ^{139}Nd and ^{140}Nd nuclei
Phys. Rev. C **87**, 064303 (2013)

5. U. Jakobsson, S. Juutinen, J. Uusitalo, M. Leino, K. Auranen, T. Enqvist, P. T. Greenlees, K. Hauschild, P. Jones, R. Julin, S. Ketelhut, P. Kuusiniemi, M. Nyman, P. Peura, P. Rahkila, **P. Ruotsalainen**, J. Sarén, C. Scholey, and J. Sorri
Spectroscopy of the proton drip-line nucleus ^{203}Fr
Phys. Rev. C **87**, 054320 (2013)

6. S.P. Bvumbi, J.F. Sharpey-Schafer, P.M. Jones, S.M. Mullins, B.M. Nyakó, K. Juhász, R.A. Bark, L. Bianco, D.M. Cullen, D. Curien, P.E. Garrett, P.T. Greenlees, J. Hirvonen, U. Jakobsson, J. Kau, F. Komati, R. Julin, S. Juutinen, S. Ketelhut, A. Korichi, E.A. Lawrie, J.J. Lawrie, M. Leino, T.E. Madiba, S.N.T. Majola, P. Maine, A. Minkova, N.J. Ncapayi, P. Nieminen, P. Peura, P. Rahkila, L.L. Riedinger, **P. Ruotsalainen**, J. Sarén, C. Scholey, J. Sorri, S. Stolze, J. Timar, J. Uusitalo and P.A.Vymers
Octupole correlations in the structure of 0_2^+ bands in the $N = 88$ nuclei ^{150}Sm and ^{152}Gd
Phys. Rev. C **87**, 044333 (2013)

7. M.G. Procter, D.M. Cullen, M.J. Taylor, J. Pakarinen, K. Auranen, T. Bäck, T. Braunroth, B. Cederwall, A. Dewald, T. Grahn, P.T. Greenlees, U. Jakobsson, R. Julin, S. Juutinen, A. Herzáň, J. Konki, M. Leino, R. Liotta, J. Partanen, P. Peura, P. Rahkila, **P. Ruotsalainen**, M. Sandelius, J. Sarén, C. Scholey, J. Sorri, S. Stolze, J. Uusitalo and C. Qi
Isomer-tagged differential-plunger measurements in $^{113}_{54}Xe$
Phys. Rev. C **87**, 014308 (2013)

8. M.J. Taylor, D.M. Cullen, A.J. Smith, A. McFarlane, V. Twist, G.A. Alharshan, M.G. Procter, T. Braunroth, A. Dewald, E. Ellinger, C. Fransen, P.A. Butler, M. Scheck, D.T. Joss, B. Saygi, C.G. McPeake, T. Grahn, P.T. Greenlees, U. Jakobsson, P. Jones, R. Julin, S. Juutinen, S. Ketelhut, M. Leino, P. Nieminen, J. Pakarinen, P. Peura, P. Rahkila, **P. Ruotsalainen**, M. Sandzelius, J. Sarén, C. Scholey, J. Sorri, S. Stolze and J. Uusitalo
A new differentially pumped plunger device to measure excited-state lifetimes in proton emitting nuclei
Nucl. Instrum. Methods Phys. Res. A **707**, 143 (2013)

9. P.T. Greenlees, J. Rubert, J. Piot, B.J.P. Gall, L.L. Andersson, M. Asai, Z. Asfari, D.M. Cox, F. Dechery, O. Dorvaux, T. Grahn, K. Hauschild, G. Henning, A. Herzáň, R.-D. Herzberg, F.P. Heßberger, U. Jakobsson, P. Jones, R. Julin, S. Juutinen, S. Ketelhut, T.-L. Khoo, M. Leino, J. Ljungvall, A. Lopez-Martens, R. Lozeva, P. Nieminen, J. Pakarinen, P. Papadakis, E. Parr, P. Peura, P. Rahkila, S. Rinta-Antila, **P. Ruotsalainen**, M. Sandzelius, J. Sarén, C. Scholey, D. Seweryniak, J. Sorri, B. Sulignano, Ch. Theisen, J. Uusitalo and M. Venhart
Shell-Structure and Pairing Interaction in Superheavy Nuclei: Rotational Properties of the $Z = 104$ Nucleus ^{256}Rf
Phys. Rev. Lett. **109**, 012501 (2012)

10. U. Jakobsson, J. Uusitalo, S. Juutinen, M. Leino, T. Enqvist, P.T. Greenlees, K. Hauschild, P. Jones, R. Julin, S. Ketelhut, P. Kuusiniemi, M. Nyman, P. Peura, P. Rahkila, **P. Ruotsalainen**, J. Sarén, C. Scholey and J. Sorri
Recoil-decay tagging study of ^{205}Fr
Phys. Rev. C **85**, 014309 (2012)

11. D. O'Donnell, R.D. Page, C. Scholey, L. Bianco, L. Capponi, R.J. Carroll, I.G. Darby, L. Donosa, M. Drummond, F. Ertuğral, T. Grahn, P.T. Greenlees, K. Hauschild, A. Herzáň, U. Jakobsson, P. Jones, D.T. Joss, R. Julin, S. Juutinen, S. Ketelhut, M. Labiche, M. Leino, A. Lopez-Martens, K. Mulholland, P. Nieminen, P. Peura, P. Rahkila, S. Rinta-Antila, **P. Ruotsalainen**, M. Sandzelius, J. Sarén, B. Saygi, J. Simpson, J. Sorri, A. Thornthwaite and J.Uusitalo
First observation of excited states of ^{173}Hg
Phys. Rev. C **85**, 054315 (2012)

12. J. Piot, B.J.-P. Gall, O. Dorvaux, P.T. Greenlees, N. Rowley, L.L. Andersson, D.M. Cox, F. Dechery, T. Grahn, K. Hauschild, G. Henning, A. Herzáň, R.-D. Herzberg, F.P. Heßberger, U. Jakobsson, P. Jones, R. Julin, S. Juutinen, S. Ketelhut, T.-L. Khoo, M. Leino, J. Ljungvall, A. Lopez-Martens, P. Nieminen, J. Pakarinen, P. Papadakis, E. Parr, P. Peura, P. Rahkila, S. Rinta-Antila, J. Rubert, **P. Ruotsalainen**, M. Sandzelius, J. Sarén, C. Scholey, D. Seweryniak, J. Sorri, B. Sulignano and J. Uusitalo
In-beam spectroscopy with intense ion beams: Evidence for a rotational structure in ^{246}Fm
Phys. Rev. C **85**, 041301(R) (2012)

13. M.G. Procter, D.M. Cullen, C. Scholey, **P. Ruotsalainen**, L. Angus, T. Bäck, B. Cederwall, A. Dewald, C. Fransen, T. Grahn, P.T. Greenlees, M. Hackstein, U. Jakobsson, P.M. Jones, R. Julin, S. Juutinen, S. Ketelhut, M. Leino, R. Liotta, N.M. Lumley, P.J.R. Mason, P. Nieminen, M. Nyman, J. Pakarinen, T. Pissulla, P. Peura, P. Rahkila, J. Revill, S.V. Rigby, W. Rother, M. Sandzelius, J. Sarén, J. Sorri, M.J. Taylor, J. Uusitalo, P. Wady, C. Qi and F.R. Xu
Electromagnetic transition strengths in $^{109}_{52}Te$
Phys. Rev. C **86**, 034308 (2012)

14. B. Sulignano, Ch. Theisen, J.-P. Delaroche, M. Girod, J. Ljungvall, D. Ackermann, S. Antalic, O. Dorvaux, A. Drouart, B. Gall, A. Görgen, P.T. Greenlees, K. Hauschild, R.-D. Herzberg, F.P. Heßberger, U. Jakobsson, P. Jones, R. Julin, S. Juutinen, S. Ketelhut, W. Korten, M. Leino, A. Lopez-Martens, M. Nyman, A. Obertelli, J. Pakarinen, P. Papadakis, E. Parr, P. Peura, J. Piot, P. Rahkila, D. Rostron, **P. Ruotsalainen**, J. Sarén, C. Scholey, J. Sorri, J. Uusitalo, M. Venhart and M. Zielińska
Investigation of high-K states in ^{252}No
Phys. Rev. C **86**, 044318 (2012)

15. M.J. Taylor, G.A. Alharshan, D.M. Cullen, M.G. Procter, N.M. Lumley, T. Grahn, P.T. Greenlees, K. Hauschild, A. Herzáň, U. Jakobsson, P. Jones, R. Julin, S. Juutinen, S. Ketelhut, M. Leino, A. Lopez-Martens, P. Nieminen, J. Partanen, P. Peura, P. Rahkila, S. Rinta-Antila, **P. Ruotsalainen**, M. Sandzelius, J. Sarén, C. Scholey, J. Sorri, S. Stolze, J. Uusitalo, F.R. Xu and Z.J. Bai
Identification of isomeric states in the $N = 73$ *neutron-deficient nuclei* ^{132}Pr *and* ^{130}La
Phys. Rev. C **86**, 044310 (2012)

16. A. Thornthwaite, D. O'Donnell, R.D. Page, D.T. Joss, C. Scholey, L. Bianco, L. Capponi, R.J. Carroll, I.G. Darby, L. Donosa, M.C. Drummond, F. Ertuğral, T. Grahn, P.T. Greenlees, K. Hauschild, A. Herzáň, U. Jakobsson, P. Jones, R. Julin, S. Juutinen, S. Ketelhut, M. Labiche, M. Leino, A. Lopez-Martens, K. Mullholland, P. Nieminen, P. Peura, P. Rahkila, S. Rinta-Antila, **P. Ruotsalainen**, M. Sandzelius, J. Sarén, B. Sayğı, J. Simpson, J. Sorri and J.Uusitalo
Characterizing the atomic mass surface beyond the proton drip line via α*-decay measurements of the* $\pi s_{1/2}$ *ground state of* ^{165}Re *and the* $\pi h_{11/2}$ *isomer in* ^{161}Ta
Phys. Rev. C **86**, 064315 (2012)

17. P.J. Sapple, R.D. Page, D.T. Joss, L. Bianco, T. Grahn, J. Pakarinen, J. Thomson, J. Simpson, D. O'Donnell, S. Ertürk, P.T. Greenlees, U. Jakobsson, P.M. Jones, R. Julin, S. Juutinen, S. Ketelhut, M. Leino, M. Nyman, P. Peura, A. Puurunen, P. Rahkila, **P. Ruotsalainen**, J. Sarén, C. Scholey and J. Uusitalo
In-beam γ-ray spectroscopy of the $N = 85$ isotones ^{159}W and ^{160}Re
Phys. Rev. C **84**, 054303 (2011)

18. H. Watkins, D.T. Joss, T. Grahn, R.D. Page, R.J. Carroll, A. Dewald, P.T. Greenlees, M. Hackstein, R.-D. Herzberg, U. Jakobsson, P.M. Jones, R. Julin, S. Juutinen, S. Ketelhut, T. Kröll, R. Krücken, M. Labiche, M. Leino, N. Lumley, P. Maierbeck, M. Nyman, P. Nieminen, D. O'Donnell, J. Ollier, J. Pakarinen, P. Peura, T. Pissulla, P. Rahkila, J.P. Revill, W. Rother, **P. Ruotsalainen**, S.V. Rigby, J. Sarén, P.J. Sapple, M. Scheck, C. Scholey, J. Simpson, J. Sorri, J. Uusitalo and M. Venhart
Lifetime measurements probing triple shape coexistence in ^{175}Au
Phys. Rev. C **84**, 051302(R) (2011)

19. T. Bäck, C. Qi, F. Ghazi Moradi, B. Cederwall, A. Johnson, R. Liotta, R. Wyss, H. Al-Azri, D. Bloor, T. Brock, R. Wadsworth, T. Grahn, P.T. Greenlees, K. Hauschild, A. Herzáň, U. Jakobsson, P.M. Jones, R. Julin, S. Juutinen, S. Ketelhut, M. Leino, A. Lopez-Martens, P. Nieminen, P. Peura, P. Rahkila, S. Rinta-Antila, **P. Ruotsalainen**, M. Sandzelius, J. Sarén, C. Scholey, J. Sorri, J. Uusitalo, S. Go, E. Ideguchi, D.M. Cullen, M.G. Procter, T. Braunroth, A. Dewald, C. Fransen, M. Hackstein, J. Litzinger and W. Rother
Lifetime measurement of the first excited 2^+ state in ^{108}Te
Phys. Rev. C **84**, 041306(R) (2011)

20. M.G. Procter, D.M. Cullen, C. Scholey, **P. Ruotsalainen**, L. Angus, T. Bäck, B. Cederwall, A. Dewald, C. Fransen, T. Grahn, P.T. Greenlees, M. Hackstein, U. Jakobsson, P.M. Jones, R. Julin, S. Juutinen, S. Ketelhut, M. Leino, R. Liotta, N.M. Lumley, P.J.R. Mason, P. Nieminen, M. Nyman, J. Pakarinen, T. Pissulla, P. Peura, P. Rahkila, J. Revill, S.V. Rigby, W. Rother, M. Sandzelius, J. Sarén, J. Sorri, M.J. Taylor, J. Uusitalo, P. Wady, C. Qi and F.R. Xu
Anomalous transition strength in the proton-unbound nucleus ^{109}I
Phys. Lett. B **704**, 118 (2011)

21. M.G. Procter, D.M. Cullen, **P. Ruotsalainen**, T. Braunroth, A. Dewald, C. Fransen, T. Grahn, P.T. Greenlees, M. Hackstein, K. Hauschild, U. Jakobsson, P.M. Jones, R. Julin, S. Juutinen, S. Ketelhut, A. Lopez-Martens, M. Leino, J. Litzinger, P.J.R. Mason, P. Nieminen, P. Peura, P. Rahkila, M.W. Reed, S. Rice, S. Rinta-Antila, W. Rother, M. Sandzelius, J. Sarén, C. Scholey, J. Sorri, M.J. Taylor, J. Uusitalo, A. Vitturi, Y. Shi and F. R. Xu
Lifetime measurements in the transitional nucleus ^{138}Gd
Phys. Rev. C **84**, 024314 (2011)

22. M.G. Procter, D.M. Cullen, C. Scholey, P.T. Greenlees, J. Hirvonen, U. Jakobsson, P. Jones, R. Julin, S. Juutinen, S. Ketelhut, M. Leino, N.M. Lumley, P.J.R. Mason, P. Nieminen, M. Nyman, P. Peura, P. Rahkila, J.-M. Regis, **P. Ruotsalainen**, J. Sarén, Y. Shi, J. Sorri, S. Stolze, J. Uusitalo and F.R. Xu
High-K four-quasiparticle states in ^{138}Gd
Phys. Rev. C **83**, 034311 (2011)

23. M. Scheck, P.A. Butler, L.P. Gaffney, N. Bree, R.J. Carrol, D. Cox, T. Grahn, P.T. Greenlees, K. Hauschild, A. Herzáň, M. Huyse, U. Jakobsson, P. Jones, D.T. Joss, R. Julin, S. Juutinen, S. Ketelhut, R.-D. Herzberg, M. Kowalczyk, A.C. Larsen, M. Leino, A. Lopez-Martens, P. Nieminen, R.D. Page, J. Pakarinen, P. Papadakis, P. Peura, P. Rahkila, S. Rinta-Antila, **P. Ruotsalainen**, M. Sandzelius, J. Sarén, C. Scholey, J. Sorri, J. Srebrny, P. Van Duppen, H.V. Watkins and J. Uusitalo
Combined in-beam electron and γ*-ray spectroscopy of* $^{184,186}Hg$
Phys. Rev. C **83**, 037303 (2011)

24. U. Jakobsson, J. Uusitalo, S. Juutinen, M. Leino, P. Nieminen, K. Andgren, B. Cederwall, P.T. Greenlees, B. Hadinia, P. Jones, R. Julin, S. Ketelhut, A. Khaplanov, M. Nyman, P. Peura, P. Rahkila, **P. Ruotsalainen**, M. Sandzelius, J. Sarén, C. Scholey and J. Sorri
Prompt and delayed spectroscopy of ^{199}At
Phys. Rev. C **82**, 044302 (2010)

25. P. Rahkila, D.G. Jenkins, J. Pakarinen, C. Gray-Jones, P.T. Greenlees, U. Jakobsson, P. Jones, R. Julin, S. Juutinen, S. Ketelhut, H. Koivisto, M. Leino, P. Nieminen, M. Nyman, P. Papadakis, S. Paschalis, M. Petri, P. Peura, O. J. Roberts, T. Ropponen, **P. Ruotsalainen**, J. Sarén, C. Scholey, J. Sorri, A.G. Tuff, J. Uusitalo, R. Wadsworth, M. Bender and P.-H. Heenen
Shape coexistence at the proton drip-line: First identification of excited states in ^{180}Pb
Phys. Rev. C **82**, 011303(R) (2010)

26. M.G. Procter, D.M. Cullen, C. Scholey, B. Niclasen, P.J.R. Mason, S.V. Rigby, J.A. Dare, A. Dewald, P.T. Greenlees, H. Iwasaki, U. Jakobsson, P.M. Jones, R. Julin, S. Juutinen, S. Ketelhut, M. Leino, N.M. Lumley, O. Möller, M. Nyman, P. Peura, T. Pissulla, A. Puurunen, P. Rahkila, W. Rother, **P. Ruotsalainen**, J. Sarén, J. Sorri and J. Uusitalo
Lifetime measurements and shape coexistence in ^{144}Dy
Phys. Rev. C **81**, 054320 (2010)

27. L. Bianco, R.D. Page, I.G. Darby, D.T. Joss, J. Simpson, J.S. Al-Khalili, A.J. Cannon, B. Cederwall, S. Eeckhaudt, S. Ertürk, B. Gall, M.B. Gómez Hornillos, T. Grahn, P.T. Greenlees, B. Hadinia, K. Heyde, U. Jakobsson, P.M. Jones, R. Julin, S. Juutinen, S. Ketelhut, M. Labiche, M. Leino, A.-P. Leppänen, M. Nyman, D. O'Donnell, E.S. Paul, M. Petri, P. Peura, A. Puurunen, P. Rahkila, **P. Ruotsalainen**, M. Sandzelius, P.J. Sapple, J. Sarén, C. Scholey, N.A. Smirnova, A.N. Steer, P.D. Stevenson, E.B. Suckling, J. Thomson, J. Uusitalo and M. Venhart
Discovery of ^{157}W *and* ^{161}Os
Phys. Lett. B **690**, 15 (2010)

28. P.J.R. Mason, D.M. Cullen, C. Scholey, P.T. Greenlees, U. Jakobsson, P.M. Jones, R. Julin, S. Juutinen, S. Ketelhut, M. Leino, M. Nyman, P. Peura, A. Puurunen, P. Rahkila, **P. Ruotsalainen**, J. Sorri, J. Sarén, J. Uusitalo and F.R. Xu
Spectroscopy of ^{144}Ho *using recoil-isomer tagging*
Phys. Rev. C **81**, 024302 (2010)

29. P.J.R. Mason, D.M. Cullen, C. Scholey, A. Dewald, O. Möller, H. Iwasaki, T. Pissulla, W. Rother, J.A. Dare, P.T. Greenlees, U. Jakobsson, P.M. Jones, R. Julin, S. Juutinen, S. Ketelhut, M. Leino, N.M. Lumley, B. Niclasen, M. Nyman, P. Peura, A. Puurunen, P. Rahkila, **P. Ruotsalainen**, J. Sorri, J. Sarén, J. Uusitalo and F.R. Xu
Isomer-tagged differential-plunger measurements in proton-unbound ^{144}Ho
Phys. Lett. B **683**, 17 (2010)

30. M.B. Gómez Hornillos, D. O'Donnell, J. Simpson, D.T. Joss, L. Bianco, B. Cederwall, T. Grahn, P.T. Greenlees, B. Hadinia, P. Jones, R. Julin, S. Juutinen, S. Ketelhut, M. Labiche, M. Leino, M. Nyman, R.D. Page, E.S. Paul, M. Petri, P. Peura, P. Rahkila, **P. Ruotsalainen**, M. Sandzelius, P.J. Sapple, J. Sarén, C. Scholey, J. Sorri, J. Thomson and J. Uusitalo
Gamma-ray spectroscopy approaching the limits of existence of atomic nuclei: A study of the excited states of ^{168}Pt *and* ^{169}Pt
Phys. Rev. C **79**, 064314 (2009)

31. D. O'Donnell, T. Grahn, D.T. Joss, J. Simpson, C. Scholey, K. Andgren, L. Bianco, B. Cederwall, D.M. Cullen, A. Dewald, E. Ganioğlu, M.B. Gómez Hornillos, P.T. Greenlees, B. Hadinia, H. Iwasaki, U. Jakobsson, J. Jolie, P. Jones, D.S. Judson, R. Julin, S. Juutinen, S. Ketelhut, M. Labiche, M. Leino, N.M. Lumley, P.J.R. Mason, O. Möller, P. Nieminen, M. Nyman, R.D. Page, J. Pakarinen, E.S. Paul, M. Petri, A. Petts, P. Peura, N. Pietralla, T. Pissulla, P. Rahkila, **P. Ruotsalainen**, M. Sandzelius, P.J. Sapple, J. Sarén, J. Sorri, J. Thomson, J. Uusitalo and H.V. Watkins
Spectroscopy of the neutron-deficient nucleus ^{167}Os
Phys. Rev. C **79**, 064309 (2009)

32. D. O'Donnell, J. Simpson, C. Scholey, T. Bäck, P.T. Greenlees, U. Jakobsson, P. Jones, D.T. Joss, D.S. Judson, R. Julin, S. Juutinen, S. Ketelhut, M. Labiche, M. Leino, M. Nyman, R.D. Page, P. Peura, P. Rahkila, **P. Ruotsalainen**, M. Sandzelius, P.J. Sapple, J. Sarén, J. Thomson, J. Uusitalo and H.V. Watkins
First observation of excited states in ^{175}Hg
Phys. Rev. C **79**, 051304(R) (2009)

33. S. Ketelhut, P.T. Greenlees, D. Ackermann, S. Antalic, E. Clément, I.G. Darby, O. Dorvaux, A. Drouart, S. Eeckhaudt, B.J.P. Gall, A. Görgen, T. Grahn, C. Gray-Jones, K. Hauschild, R.-D. Herzberg, F.P. Heßberger, U. Jakobsson, G.D. Jones, P. Jones, R. Julin, S. Juutinen, T.-L. Khoo, W. Korten, M. Leino, A.-P. Leppänen, J. Ljungvall, S. Moon, M. Nyman, A. Obertelli, J. Pakarinen, E. Parr, P. Papadakis, P. Peura, J. Piot, A. Pritchard, P. Rahkila, D. Rostron, **P. Ruotsalainen**, M. Sandzelius, J. Sarén, C. Scholey, J. Sorri, A. Steer, B. Sulignano, Ch. Theisen, J. Uusitalo, M. Venhart, M. Zielinska, M. Bender and P.-H. Heenen
Gamma-Ray Spectroscopy at the Limits: First Observation of Rotational Bands in ^{255}Lr
Phys. Rev. Lett. **102**, 212501 (2009)

34. R. Wadsworth, B.S. Nara Singh, A.N. Steer, D.G. Jenkins, M.A. Bentley, T. Brock, P. Davies, R. Glover, N.S. Pattabiraman, C. Scholey, T. Grahn, P.T. Greenlees, P. Jones, U. Jakobsson, R. Julin, S. Juutinen, S. Ketelhut, M. Leino, M. Nyman, P. Peura, J. Pakarinen, P. Rahkila, **P. Ruotsalainen**, J. Sorri, J. Uusitalo, C.J. Lister, P.A. Butler, M. Dimmock, D.T. Joss, J. Thomson, S. Rinta-Antila, B. Cederwall, B. Hadinia, M. Sandzelius, A. Atac, L. Betterman, A. Blazhev, N. Braun, F. Finke, K. Geibel, G. Ilie, H. Iwasaki, J. Jolie, P. Reiter, C. Scholl, N. Warr, P. Boutachkov, L. Caceres, C. Domingo, T. Engert, F. Farinon, J. Gerl, N. Goel, M. Gorska, H. Grawe, N. Kurz, I. Kojuharov, S. Pietri, C. Nociforo, A. Prochazka, H.-J. Wollersheim, K. Eppinger, T. Faestermann, C. Hinke, R. Hoischen, R. Kruecken, A. Gottardo, Z. Liu, P. Woods, J. Grebosz, E. Merchant, J. Nyberg, P.-A. Söderström, Z. Podolyak, P. Regan, S. Steer, M. Pfutzner, D. Rudolph
The Northwest Frontier: Spectroscopy of $N \sim Z$ Nuclei Below Mass 100
Acta Phys. Pol. B **40**, 611 (2009)

35. L. Bianco, R.D. Page, D.T. Joss, J. Simpson, B. Cederwall, M.B. Gómez Hornillos, P.T. Greenlees, B. Hadinia, U. Jakobsson, P.M. Jones, R. Julin, S. Ketelhut, M. Labiche, M. Leino, M. Nyman, E.S. Paul, M. Petri, P. Peura, A. Puurunen, P. Rahkila, **P. Ruotsalainen**, M. Sandzelius, P.J. Sapple, J. Sarén, C. Scholey, J. Thomson, J. Uusitalo
Alpha-decay branching ratios measured by γ-ray tagging
Nucl. Instrum. Meth. Phys. Res. A **597**, 189 (2008)

Contents

Chapter 1

Introduction

The atom, indivisible as the ancient Greek philosophers thought, consists of a small and dense nucleus surrounded by a cloud of electrons. The nucleus is a collection of individual nucleons orbiting relative to each other and is held together by a short-range strong force acting between the nucleons. These ideas are roughly 100 years old, but still the fundamental understanding of the strong nuclear force is limited. In other words, it is not possible to write down a single equation, which would be able to describe all the salient features of nuclear species ranging from hydrogen up to element 118. To put this into perspective, there are roughly 300 stable nuclei in nature and roughly 3000 unstable nuclei have been synthesised and studied in laboratories in different parts of the world. Moreover, there ought to be ∼4000 additional nuclei between the drip lines [1], which have not yet been studied or identified experimentally *i.e.,* the current experimental progress is roughly at the halfway mark.

Big scientific advances take time, effort and especially experimental data. A detailed study of a few exotic nuclear species, as has been carried out in the present work, may not necessarily seem very fruitful and is certainly not enough to answer any of the fundamental nuclear physics problems. However, when the same procedure, as carried out in the present work, is performed for the thousands of other nuclei in the nuclear chart, a *frail grasp on the big picture* eventually starts to materialise. Indeed, currently different theoretical nuclear models are able to successfully describe still larger groups of elements and their isotopes. In this thesis two nuclei, ${}^{66}_{33}\mathrm{As}_{33}$ and ${}^{66}_{34}\mathrm{Se}_{32}$, located near the proton drip line have been experimentally studied. The results are compared to theoretical predictions obtained by shell-model calculations. Moreover, an experimental method to perform spectroscopic studies in the $A \approx 70$ region is introduced and the new instrumentation to enhance its sensitivity is described.

1.1 Physics phenomena in the region of interest

The relevant part of the chart of nuclei for this work is shown in Fig. 1.1. Nuclei residing at or close to the $N = Z$ line are interesting for various reasons. In the case of self-conjugate odd-odd $N = Z$ nuclei, the protons and neutrons occupy the same single-particle orbits, which leads to maximal overlap of their wave functions. This gives rise to the enhanced neutron-proton (np) pairing correlations, which should happen, in principle, both in the isoscalar $T = 0$ and isovector $T = 1$ channels, whereas away from the $N = Z$ line, like nucleon pairing ($T = 1$ mode) is known to dominate. However, for medium-mass $N = Z$ nuclei there is no clear evidence for strong $T = 0$, np correlations until the $A \approx 90$ mass region is reached [2, 3]. It is still an open debate whether the isoscalar np pairing has any significant influence on the structure of medium-mass $N = Z$ nuclei below mass $A \approx 90$. In addition, theoretical studies have indicated that the presence of a strong isovector np pair field at low spins is found to dominate the structure in these nuclei [4, 5]. In the case of ^{66}As, the lowest $T = 0$, 1^+ state is observed to lie $\sim$1 MeV above the $T = 1$, 0^+ ground state, which is indicative of a reduced strength of the $T = 0$ pairing compared to the $T = 1$ mode. A similar observation has been made earlier for the heavier odd-odd $N = Z$ nucleus ^{70}Br [6].

Around the mass $A = 70$ region, nuclear structure is expected to become significantly more complex with more orbitals involved in comparison to the nuclei near mass $A = 40 - 50$, where the structure is dominated by one orbital only, namely $f_{7/2}$. In addition, there is evidence of a sudden structural change when going towards the mass $A = 70 - 80$ region and the phenomena of shape coexistence, driven by the increasing occupancy of the $g_{9/2}$ orbital, is observed [7, and references therein]. Aside from the pure nuclear structure interest, the nuclei in this region have an impact on related areas of physics including standard model tests [8] and nuclear astrophysics [9] since these nuclei are directly involved in the rapid-proton capture process.

Lastly, nuclei around the $N = Z$ line are grand examples of isospin symmetry and related phenomena. However, when ^{100}Sn is approached, the increasing Coulomb field starts to mix states with different isospin. This affects both the γ-ray transitions and β decays, because in the absence of the isospin mixing, both $E1$ γ-ray transitions and Fermi β decays are forbidden [10, 11]. In addition, isospin-symmetry breaking manifests itself in this region as will be extensively discussed in the following sections.

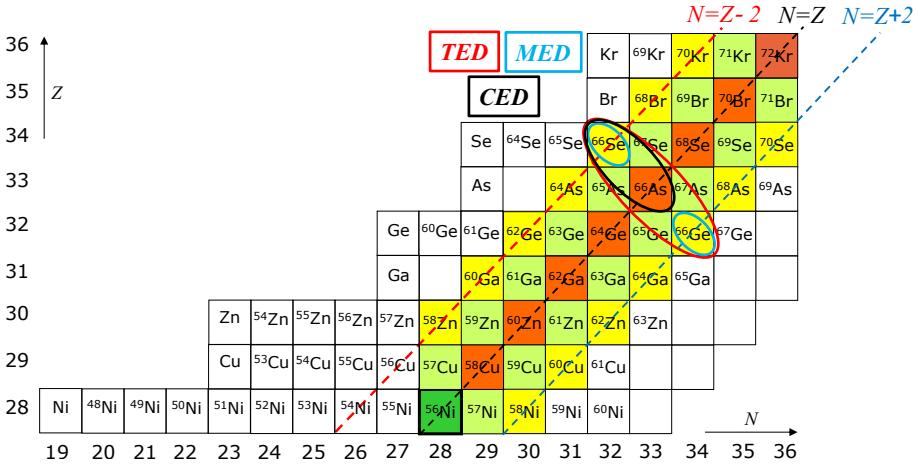

Figure 1.1: Illustration of the region of the nuclear chart studied in this thesis. The main focus is on the isobaric triplet with mass $A = 66$, where Coulomb energy differences (TED, MED and CED) between excited isobaric analogue states have been studied.

1.2 A theoretical description of the nucleus

A nucleus consists of Z protons and N neutrons and in total A nucleons, which defines the mass number of the nucleus by the relation $A = Z + N$. Nucleons are strongly interacting with each other and are confined within a potential V, which is itself produced by all the A nucleons. This picture gives rise to the nuclear shell model, which has passaged through from an independent particle model to a more realistic interacting shell model over the last 60 years. In general, the shell model has proven to be a very successful tool to describe nuclear structure and related effects. In the shell-model description the starting point is the construction of the nuclear many-body Hamiltonian operator H, which is traditionally divided into an unperturbed and a residual parts $H = H_0 + H_{RES}$. The next step is to solve the many-body eigenvalue equation

$$H\,|\Psi_n\rangle = E_n\,|\Psi_n\rangle\,, \tag{1.1}$$

where $|\Psi_n\rangle$ is a many-nucleon state corresponding to an eigenenergy E_n of a state. The solving of this quantum many-body problem can be carried out by using numerical methods and it yields predictions *e.g.,* for the level energies and wave functions of the states in the nucleus under study. These results are then compared to the available experimental data and corrections or refinements in the parameterisation of the Hamiltonian are carried out if necessary.

The modern shell-model calculations use effective Hamiltonians, which are derived from phenomenological potentials. A key feature is the use of modern effective two-body nuclear interactions such as JUN45 [12] employed in the present thesis. Here, the existing interaction is modified empirically to fit the existing experimental data and can be used to predict the properties of nuclei in the mass $A = 60 - 90$ region. Therefore, the experimental studies of exotic nuclei in the mass $A \approx 70$ region provide an excellent opportunity to test these interactions and model spaces.

The shell-model approach is a microscopic model, which can characterise nuclear structure effects induced by individual nucleons. Modern large-scale shell-model calculations are also able to reproduce more collective phenomena such as the rotation of a deformed nucleus with good accuracy [13, and references therein]. In this thesis, nuclear structure effects induced by the Coulomb interaction, which is generally regarded to be a lot weaker in comparison to the strong nuclear interaction, are of highest interest. The repulsive Coulomb interaction between protons gives rise to energy differences between isobaric analogue states (IAS) described later in detail in section 1.4 and violates both the charge-symmetry and charge-independence characteristics of the strong nuclear force. The calculations presented in the current work are based (to some extent) on the formalism developed in Refs. [14, 15]. The technical details are omitted as they are out of the scope of the present work, but the main points are outlined. The starting point in these calculations is that the effective Hamiltonian is divided into a monopole H_m and multipole H_M components. Especially, the Coulomb interaction V_C is separated into a monopole part V_{Cm} and a multipole part V_{CM}. Here, the monopole term accounts for the single-particle effects and bulk properties, whereas the multipole component describes the Coulomb contribution resulting from the angular momentum recoupling of the valence protons [16]. The monopole part V_{Cm} is further divided into the radial term V_{Cr}, the single-particle correction term ϵ_{ll} and the electromagnetic spin-orbit term ϵ_{ls}.

The radial term V_{Cr} accounts for the change of nuclear radius along the rotational band. In the shell-model approach, changes of nuclear radii do not necessarily depend on nuclear deformation [17]. The magnitude of the radial term is dependent on the occupation of shell-model orbitals as they tend to have different radii. Orbitals with smaller radii are nearer to the charged core and therefore protons occupying such orbitals feel an increased Coulomb repulsion and the corresponding states have more Coulomb energy. The monopole Coulomb radial contribution can be estimated by the relation [13]

$$V_{Cr}(J) = -\frac{3}{5} Z(Z-1) e^2 \frac{\Delta R(J)}{R_C^2}, \tag{1.2}$$

where $\Delta R(J) = R_C(J) - R_C(J=0)$, $R_C(J)$ is the radius of a uniformly charged sphere at spin J and e is the elementary charge. The two terms ϵ_{ll} and ϵ_{ls} effect the single-particle energies. The single-particle correction term ϵ_{ll} only effects the proton orbitals. This effect may be evaluated by the relation [18]

$$\epsilon_{ll} = \frac{-4.5 Z_{cs}^{13/12}[2l(l+1) - N(N+3)]}{A^{1/3}(N+3/2)} \text{ keV}, \tag{1.3}$$

where N is the principal quantum number of the oscillator shell and Z_{cs} is the nearest closed shell of the orbital occupied by the proton. For example, in the case of ^{66}As groundstate, the odd proton occupies the $1f_{5/2}$ orbit, thus $N = 3$ and $Z_{cs} = 28$. The other single-particle energy shift term ϵ_{ls} is the relativistic electromagnetic spin-orbit interaction. The effect of the nuclear spin-orbit interaction is well known and accounts for the splitting of levels with $l > 0$ resulting in the correct magic numbers. Although, the strength of the electromagnetic spin-orbit interaction is two orders of magnitude smaller than the nuclear spin-orbit force (several MeV), recent shell-model calculations show that the ϵ_{ls} term can be used to explain the experimentally observed energy differences between IAS [16, 13]. The reason is that the ϵ_{ls} has a different effect on neutron and proton orbitals, hence, it may lower the energy of the proton single-particle orbitals, while simultaneously raising the energy of the neutron orbital or vice versa. As a result, a gap of several hundreds of keV may be formed between the corresponding orbitals. This effect will be discussed more in section 3.3.3 when experimental data is interpreted. For completeness, the ϵ_{ls} term can be written in the simplified form as given in Ref. [19]

$$\epsilon_{ls} \cong (g_s - g_l)\frac{1}{2m_N^2 c^2}\left(-\frac{Ze^2}{R_C^3}\right)\left\langle \hat{l}\cdot\hat{s}\right\rangle, \tag{1.4}$$

where g_s and g_l are the gyromagnetic factors and m_N is the nucleon mass. From this relation one can deduce that the energy shift will have a different sign for a neutron orbital and a proton orbital. Moreover, the sign of the shift will depend on the spin-orbit coupling as discussed in [13].

The monopole Coulomb interactions described above will be discussed more in section 1.4 together with the multipole Coulomb interactions after the Coulomb energy differences have been formally introduced. In addition, these will be used to interpret the experimental data presented in chapters 3 and 5.

1.3 Isospin formalism

The building blocks of the nucleus *i.e.,* the protons and the neutrons are conventionally regarded as two different particle species differing in charge and slightly in mass. However, as these particles are affected similarly by the strong nuclear force, they can be viewed as two different quantum states of a generic particle, the nucleon. Another justification for this viewpoint arises from β decay, where a nucleon changes from a proton state to a neutron state with the emission of a positron and neutrino (or alternatively from a neutron state to a proton state with the emission of an electron and antineutrino). This approach leads to the concept of isospin in which nucleons are distinguished by a z-projection T_z of the isospin quantum number T. The isospin representation simplifies the treatment of the two-body nucleon-nucleon interaction and the classification of nuclear states. The effects of isospin and isospin symmetry are most apparent in the case of nuclei with $N \approx Z$.

The definition of the projection quantum numbers $T_{z_n} = +1/2$ for neutrons and $T_{z_p} = -1/2$ for protons are adopted from Ref. [20]. The total isospin projection T_z of a state is obtained by adding the single-nucleon contributions algebraically, hence, for the two-particle proton-proton (pp) system $T_z = -1$. Similarly, in the case of the two-particle neutron-neutron (nn) and neutron-proton (np) systems, the isospin projection quantum numbers are $T_z = +1$ and $T_z = 0$, respectively. The total isospin T of a multi-nucleon state is a vector sum of the isospins of the individual nucleons and can not be less than its projection $|T_z|$, but a given T can have projection quantum numbers $T_z = T, ...0, ... - T$. Therefore, states in the two-particle nn and pp systems can only have $T = 1$, whereas in the np system ($T_z = 0$) $T = 0$ and $T = 1$ states are allowed. The $T = 1$ state corresponds to the two-nucleon configuration where the intrinsic spins of the individual nucleons are coupled anti-parallel. The $T = 0$ state represents parallel coupling of the intrinsic spins and is allowed only in the np system as such a configuration is forbidden by the Pauli principle in the nn and pp systems. The three identically constructed $T = 1$ states in the pp, nn and np systems form an isospin triplet, whereas the $T = 0$ state in the np system is an isospin singlet. This labeling idea can be generalised and used also in the many-particle systems. Hence, a complete set of nuclei where the states are characterised by the same T, form an isobaric multiplet and these states are called isobaric analogue states (IAS). A given nucleus can have states with T values ranging from $|N - Z|/2$ up to $A/2$. However, in the case of the $N \approx Z$ nuclei, the $T > |N - Z|/2$ states lie significantly higher in excitation energy than the $T = |N - Z|/2$ states and hence, are not generally known experimentally [20].

1.4 Coulomb energy differences

The Coulomb field induces large differences in nuclear binding energies and its contribution to the nuclear mass is of the order of hundreds of MeV. The binding energy of the nucleus is lowered by the Coulomb interaction as illustrated in the Weizsäcker's formula

$$B = a_v A - a_s A^{2/3} - a_c Z(Z-1)A^{-1/3} - a_{sym}\frac{(A-2Z)^2}{A} + \delta, \qquad (1.5)$$

where the $a_c Z(Z-1)A^{-1/3}$ term corresponds to the Coulomb contribution [21]. The differences in binding energies are generally referred to as Coulomb displacement energies (CDE). However, in this work the relative differences between the excited states within an isobaric multiplet are investigated and so, the absolute binding energies of the ground states are normalised.

The charge-symmetry and charge-independence of the strong nuclear force resulted in the introduction of the isospin formalism, which couples these features together with the Pauli principle. Isospin symmetry, as described in section 1.3, implies that any state that can be constructed in the even-even pp and nn systems ($N = Z - 2$ or $N = Z + 2$) also has to exist in the odd-odd np ($N = Z$) system and the resulting analogue states with isospin $T = 1$ are degenerate. However, this degeneracy is lifted by isospin non-conserving (INC) forces, such as the Coulomb interaction discussed in section 1.2, and leads to differences in excitation energies between IAS [13]. These energy differences, generically named Coulomb energy differences (CED), can be used to probe the microscopic and macroscopic structure of nuclei. The CED have been used to provide information on the alignment of the valence nucleons [22], shape changes as a function of spin [23] and the evolution of nuclear radii along the yrast line [17].

The different CED computations used in this thesis are defined as follows (the definitions are adopted from Ref. [13]). In the case of the $N = Z$ and $N = Z + 2$ nuclei, which have the same mass number, but where one proton is interchanged with a neutron in the $T_z = 0$ partner, the CED are evaluated with the relation:

$$\mathrm{CED}_{J,T} = E^*_{J,T,T_z=0} - E^*_{J,T,T_z=+1}. \qquad (1.6)$$

Here, E^* is the excitation energy of the state with spin J and isospin projection quantum number $T_z = 0$ or $T_z = +1$. For a pair of mirror nuclei, which have the same mass number, but where the number of protons and neutrons is interchanged, the CED are specifically called the mirror energy differences (MED). The MED are defined by the relation:

$$\mathrm{MED}_{J,T} = E^*_{J,T,T_z=-1} - E^*_{J,T,T_z=+1}. \tag{1.7}$$

Analogue states in pairs of mirror nuclei, as discussed above, are subsets of complete isobaric multiplets. In the case of complete isobaric triplets, where $T_z = (N-Z)/2 = 0, \pm 1$, the triplet energy differences (TED) can be extracted. The TED are defined by the relation:

$$\mathrm{TED}_{J,T} = E^*_{J,T,T_z=-1} + E^*_{J,T,T_z=+1} - 2E^*_{J,T,T_z=0}. \tag{1.8}$$

To relate Eqs. 1.6, 1.7 and 1.8 to the shell-model description, some exhaustive mathematical formalism has to be used. Here, basically all the technical details are omitted and only the main points are outlined. The starting point is an isospin non-conserving and charge-dependent Hamiltonian operator $H^{\mathrm{INC}}_{\mathrm{tot}}$, which contains the Coulomb interaction acting between protons and charge-dependent forces of nuclear origin. The $H^{\mathrm{INC}}_{\mathrm{tot}}$ may be separated into isoscalar ($k = 0$), isovector ($k = 1$) and isotensor ($k = 2$) components [24]

$$H^{\mathrm{INC}}_{\mathrm{tot}} = \sum_{k=0}^{2} H^{(k)} = v_0^{(0)} I_0^{(0)} + \sum_{k=0}^{2} v_1^{(k)} I_1^{(k)}, \tag{1.9}$$

where $I_T^{(k)}$ are isospin operators. The tensor components $v^{(k)}$ of the interaction in Eq. 1.9 are related to the interactions between protons and neutrons [24]

$$v^{(0)} = \frac{1}{3}(v^{(pp)} + v^{(nn)} + v^{(pn)}), \tag{1.10}$$

$$v^{(1)} = v^{(pp)} - v^{(nn)}, \tag{1.11}$$

$$v^{(2)} = v^{(pp)} + v^{(nn)} - 2v^{(pn)}. \tag{1.12}$$

These equations are related to the charge-symmetry and charge-independence of the nucleon-nucleon interaction. Equation 1.11 implies that the isovector component of the nucleon-nucleon interaction is responsible for charge-asymmetry, whereas the charge-dependence is generated by an isotensor force as illustrated by the Eq. 1.12.

Comparing Eq. 1.11 with Eq. 1.7 (or with Eq. 1.6) reveals that the MED (CED) relate to the isovector energy differences. If the nucleon-nucleon interaction was charge-symmetric in the absence of the Coulomb force, then the MED (CED) ought to be zero. In practice, it is found in the $f_{7/2}$ shell that the MED vary

as a function of angular momentum on an energy scale of around ∼100 keV. In the case of lighter nuclei in the *sd* shell, larger values up to 300 keV have been encountered. The main mechanism of the MED as a function of spin relates to the multipole Coulomb effects, hence, alignment of nucleons along the rotational band. This means that the Coulomb interaction between two protons in time-reversed orbits is larger than for any other coupling [13]. When the angular momenta recoupling of two protons occurs, the Coulomb energy is reduced as the spatial overlap of the proton wave functions is decreased. This is reflected in the reduction of the excitation energy of a nuclear state. Naturally, if it is a neutron pair, which recouple their angular momenta, the Coulomb interaction has no effect. Hence, when the MED are computed, the decrease in the MED indicates that it is a proton pair aligning in the one member of the mirror partners and a neutron pair in the other. Similarly, if the MED is observed to increase, the picture is reversed. If only this mechanism is considered, the MED ought to reach its maximum value at the back-bend region *i.e.,* when the Coriolis anti-pairing interaction exceeds the nucleon-nucleon pairing force. In the case of the CED, one would expect a positive CED behaviour as there are always more proton pairs in the $N = Z + 2$ member of the multiplet.

Even on the assumption of perfect symmetry of the wave functions for IAS, calculating the MED for a specific case has proven to be complex. In addition to the multipole Coulomb effects discussed above, contributions to the MED are found from monopole Coulomb effects *i.e.,* from the changes in radius or shape as a function of spin, single-particle Coulomb shifts and the electromagnetic spin-orbit interaction. In cases of weak binding, the breakdown of the symmetry can also lead to further effects such as Thomas-Ehrman shifts [25, 26]. Where mirror states are well bound, there has been considerable success in calculating the MED and a good correspondence is found with experiments for nuclei in the $f_{7/2}$ shell [13]. This has been due to the fact that the different monopole contributions are identified and incorporated correctly in the shell-model calculations.

Comparing Eq. 1.12 with Eq. 1.8 shows that the TED probe the isotensor part of the nucleon-nucleon interaction. In other words, they are sensitive to charge-dependent effects, since they reflect the difference between the average of the proton-proton (pp) and neutron-neutron (nn) interactions and the neutron-proton (np) interaction. The TED have a special property that make them particularly attractive to study. That is, the TED are not expected to be strongly influenced by the single-particle contributions described earlier and, therefore, are more straightforward to compute theoretically. For instance, the radial term V_{Cr} (see Eq. 1.2), important for the MED and CED, is basically canceled in the TED calculation as the dependence on Z is removed. Thus, as a first approximation, the TED is dominated by the Coulomb multipole component only. However, it has been demonstrated previously in the $f_{7/2}$ shell that the multipole term is not sufficient to produce the experimental TED magni-

tude [13]. Therefore, an additional isospin non-conserving tensor component was added into the calculations. The origin of this charge-dependent interaction is still an open question and whether it is further needed in the upper part of the fp shell, is not clear at all.

Extensive information on the MED and TED exists for the *sd* shell, where the relevant nuclei lie close to or on the line of stability (for the most recent example see Ref. [27]). Over the last fifteen years, information on low-lying excited states has been gathered in the $f_{7/2}$ shell, allowing the MED and TED to be studied for the $A = 46$ [28] and $A = 54$ [29] triplets. However, in the upper *fp* shell the experimental information is extremely limited for odd-odd $N = Z$ nuclei between ^{56}Ni and ^{100}Sn and almost non-existent for $T_z = -1$ nuclei. This is undoubtedly due to the low production cross-sections for such nuclei as they lie very far from the line of stability (see Fig. 1.1). In order to test the current understanding of the isospin-breaking mechanisms and shell-model predictions, it would be of high interest to pursue the TED and MED investigations beyond ^{56}Ni. In this thesis the observations of $T = 1$ states up to spin $J^\pi = 6^+$ in the $N = Z$ nucleus ^{66}As and $N = Z - 2$ nucleus ^{66}Se are presented. This renders possible the most complete TED and MED studies to date above the $f_{7/2}$ shell. The isospin-symmetry breaking effects are discussed further in sections 3.3.3, 5.2.1 and 5.2.2.

Chapter 2

Experimental techniques

In recent decades the study of exotic nuclei has been driven by advances in experimental sensitivity concomitant with advances in detection technology. This has allowed nuclear structure to be studied at extreme limits of existence, both in the super-heavy region of the nuclear chart and near and beyond the proton drip line. In this chapter methods relating to the experimental study of the nuclear structure of neutron deficient nuclei will be presented. To begin with, formation and identification of these exotic nuclei will be briefly covered, followed by a description of the experimental set-up and methods used in the current thesis. In the last two sections, a new technique to study neutron deficient medium-mass nuclei in the mass $A \approx 70$ region is presented.

2.1 Nuclear formation and identification

The study of radioactive nuclei is primarily based on the use of particle accelerators. Here, the accelerated (stable or radioactive) ion beam impinges on a target consisting of a certain collection of (stable or radioactive) atoms. Depending on the kinetic energy of the beam, different kinds of nuclear reactions may occur upon the collision. In this thesis work, the nuclei of interest have been synthesised via fusion-evaporation reactions. This means that the (stable) beam particles are accelerated to an energy high enough to overcome the Coulomb barrier and consequently, fuse with the (stable) target nuclei. This leads to the formation of a rapidly rotating and highly excited compound nucleus which, in the first instance, releases excess energy by particle (neutron, proton or α particle) emission. After particle evaporation, the remaining excitation energy of the recoiling fusion residues (hereafter called a recoils) is

released by γ-ray emission. Initially, an emission of statistical γ rays occurs in a region of high level density followed by emission of γ rays from more discrete energy levels. The latter mentioned process typically proceeds via yrast levels, *i.e.,* lowest energy level for a given angular momentum, leading finally to the ground state of the nucleus. These γ-ray lines are commonly seen in an experiment and, thus, can provide an insight into the structure of the nucleus under study.

Very often the nuclei of interest are produced with very-low cross-sections of the order of $\sim$10 nb$-$100 μb in comparison to the strongest evaporation channels with $\sim$10 mb cross-sections from a total-fusion production cross-section of 100 mb or more. This presents an incredible challenge to observe the relevant signal embedded in a vast background. An example of a technique which can extract the signal of an exotic nucleus produced with a very-low cross-section with exquisite sensitivity is recoil-decay tagging (RDT) [30, 31]. This technique exploits the characteristic decay properties of the nucleus of interest to identify it at the focal plane of a recoil separator and then tag the associated prompt or delayed γ rays or conversion electrons. In the RDT method, the recoil is identified by its characteristic α, β or proton decay occurring within a certain time window (correlation or search time) in the same pixel as the recoil in the implantation detector. After the recoil has been successfully identified, a search for the preceding or subsequent radiation related to this particular recoil can be accomplished. If the radiation such as γ rays or conversion electrons detected at the focal plane of a recoil separator or at the target area in a germanium array are found to coincide with the recoil event within a suitable time interval, the recorded radiation signals can be linked to the source of the radiation. Hence, the γ-ray transitions or conversion electrons are "tagged". In the case of prompt γ radiation, a time interval corresponding to the average flight time of the recoils through the separator system needs to be taken into account in order to successfully tag the detected prompt γ rays. At the focal plane of a separator, a suitable time interval dictated by the half-life of the isomeric state in the recoil of interest, is required. In turn, if the delayed γ-ray emission following the recoil implantation is known, that can be used as a tag in a similar manner to the α, β or proton decay of the recoil. This method is called recoil-isomer tagging (RIT) [32, 33] and has been utilised in the present work.

Experimental studies of $N = Z$ and $N = Z - 2$ nuclei in the fpg shell region of the nuclear chart are very challenging as they lie rather close to the proton-drip line, where the production cross-sections in fusion-evaporation reactions become small compared to the lighter fp shell nuclei. In addition, in the case of odd-odd $N = Z$ nuclei, the $T = 1$ bands become rapidly non-yrast, which leads to the fact that they are weakly populated. As a result, new experimental approaches are required to study heavier $N \approx Z$ nuclei. The recent development of the recoil-β tagging (RBT) technique [23, 34, 35, 36]

provides a tool to extend the use of tagging methodology to the region of exotic medium-mass nuclei around the $N = Z$ line. In the RBT method, the recoil identification is carried out by detecting a positron (electron) originating from the β decay of the recoil. The obvious difficulty to cleanly tag with positrons (electrons) is the continuous energy distribution of these particles caused by the three-body decay nature of the β-decay process. Furthermore, the positron (electron) energy distributions originating from the recoils formed via different fusion-evaporation channels typically reach values of $\leq$3 MeV and, moreover, overlap with each other making the selection of a single evaporation channel extremely challenging. The β-decay processes are generally also rather slow, *i.e.,* the typical half-lives of the β decays extend from seconds to hours, which is not beneficial for tagging purposes as the tagging procedure starts to suffer from false correlations if the time difference between the recoil implantation and the decay is too long. However, a certain subgroup of nuclei are Fermi super-allowed β emitters, which have β-decay properties suitable for RDT due to their distinct high β-decay end-point-energies and short half-lives (see section 2.3).

2.2 Instrumentation

In order to achieve the goals described earlier, very special instrumentation is required on a large scale. The operation and maintenance of these devices involve a wide-ranging understanding and expertise of different areas of physics. Therefore, allocated groups of researchers working with each device and, especially, working seamlessly with each other, are needed. Moreover, continuous development work of equipment is an essential part in the production of new experimental data. A schematic illustration of the most relevant part of the experimental set-up used in the current work is illustrated in Fig. 2.1. In the following, a short description of each apparatus used in the experimental part of this thesis is given.

2.2.1 Beam production and acceleration

Before the ion beam enters into the research station, the beam must be produced, accelerated and transported. Ion beams are produced in Electron Cyclotron Resonance (ECR) ion sources. The Accelerator Laboratory at the University of Jyväskylä (JYFL) has two ECR ion sources, which are operated by a devoted research group. In the ECR ion source, the ions are produced inside a plasma, which is confined with a magnetic field and heated with microwaves. Here, the electrons are impacted on the initially neutral atoms by resonant microwaves resulting in the ionization of the atoms. After the desired average charge state is achieved, ions are extracted and selected from the plasma for

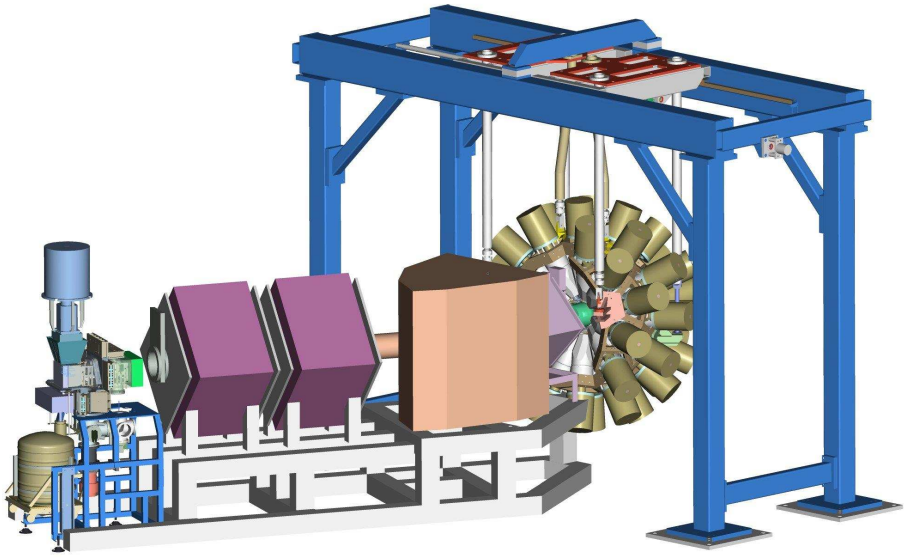

Figure 2.1: A schematic drawing of the GREAT + RITU + JUROGAM set-up (from left to right). In this particular figure, the JUROGAM germanium array, which has been replaced by the JUROGAM II germanium array, is shown.

further acceleration. An extensive and detailed presentation of the ECR ion sources employed at JYFL is provided in Ref. [37].

The ion beam is accelerated to the final energy with JYFL K-130 cyclotron. The beam is forced into a circular path by electromagnets, which are divided into three sectors. The particles orbit inside two semicircular metal chambers (called dees), which are coupled to alternating voltage power supplies. Each time the beam particles cross one of the four gaps between the dees, they feel an accelerating voltage and, hence, gain energy during each cycle. After the desired kinetic energy is reached, the beam is extracted from the cyclotron and steered to the research station where it impinges on a target foil. In the experimental part of this thesis, $^{28}Si^{+5}$ ions were accelerated to an energy of $\sim$ 80 MeV and bombarded ^{nat}Ca target.

2.2.2 The JUROGAM II germanium-detector array

The target area is surrounded by the JUROGAM II germanium-detector array to detect γ-ray transitions emitted by the reaction products. In the latter part of 2008 the JUROGAM II germanium array replaced the JUROGAM array,

which was used for nuclear structure studies at JYFL between 2002 and 2008. The author of this thesis was heavily involved in the construction phase of the JUROGAM II spectrometer and is honoured to be the first person (from Jyväskylä) to publish his thesis based on data collected solely with this device. The JUROGAM II spectrometer consists of 24 EUROGAM four-crystal clover [38] and 15 EUROGAM single-crystal phase 1 [39] or GASP [40] germanium detectors. All of the germanium detectors are Compton-suppressed (vetoed) with BGO shields. In addition, a software-based add-back algorithm [41] has been used with the clover detectors in this thesis. The major benefit of this approach is that it allows the reconstruction of Compton-scattered γ-ray events (assuming that the scattered γ ray has not escaped from the detector) and thereby increases the γ-ray detection efficiency of the clover detectors and improves the peak-to-background ratio. In the add-back process, only those γ-ray events, which occur within a 0 to 200 ns time gate in neighbouring crystals of the clover detector are considered. There is no explicit energy threshold for the γ rays in the add-back procedure, but the failed (*i.e.,* ADC conversion has failed), piled-up and vetoed events are rejected.

The JUROGAM II germanium detectors are divided into four rings at angles of 75.5° (12 clover detectors), 104.5° (12 clover detectors), 133.6° (10 phase 1 detectors) and 157.6° (5 phase 1 detectors) with respect to the beam direction. This enables investigations of angular distributions and angular distribution ratios of emitted γ rays as will be discussed in section 3.1.1. In order to perform an angular distribution analysis and to extract the (relative) intensities of the observed γ-ray transitions, the total γ-ray detection efficiency and the efficiencies for each individual ring were measured using standard ^{152}Eu and ^{133}Ba calibration sources. This is illustrated in Fig. 2.2 where the fits to the data are also presented. The fitted function is of the form

$$\epsilon = \exp\left\{[(A+Bx)^{-G} + (D+Ey+Fy^2)^{-G}]^{-1/G}\right\}, \tag{2.1}$$

where $x = \ln(E_\gamma/100)$ and $y = \ln(E_\gamma/1000)$ [42]. These fits provide information only on the relative efficiency of the array, but the commonly accepted absolute efficiency value of 6.1 % at 1.3 MeV has been used to normalise both the measured data and fits. The curves presented in Fig. 2.2 were used in the analysis of the ^{66}As data, but a similar type of efficiency determination was also carried out in the case of the ^{66}Se data.

The energy calibration *i.e.,* gain matching of JUROGAM II can be carried out by using standard calibration sources such as ^{60}Co, ^{152}Eu and ^{133}Ba. In this case, the energies of the γ rays measured in-beam need to be Doppler corrected as the source of radiation (the recoil) is flying out from the target with a velocity of $\sim$3 % of the speed of light. The Doppler-correction factor can be

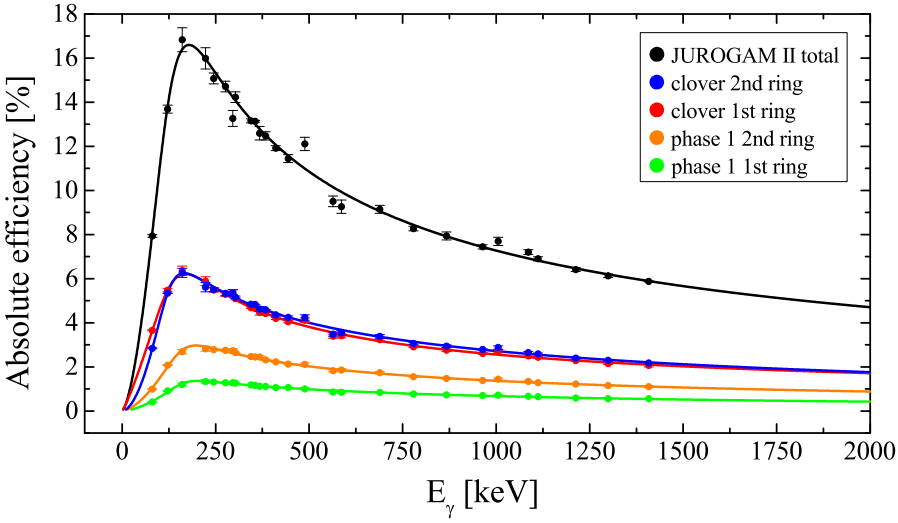

Figure 2.2: JUROGAM II total and ring efficiencies measured using ^{152}Eu and ^{133}Ba calibration sources. Solid curves represents the fits of Eq. 2.1 to the data. Initially relative values are normalised to 6.1 % at 1.3 MeV.

calculated from the reaction kinematics, but often the exact values of different variables such as the target thickness and the beam energy are not known with enough precision for an accurate calculation. There are two ways to overcome this issue. Firstly, the Doppler-correction can be determined using the known energies of (in-beam) measured γ rays. Here, the prompt γ rays are sorted without the Doppler correction into four spectra corresponding to each ring of detectors and plotted against $E_\gamma \times \cos(\theta)$, where E_γ is the literature value for the γ-ray energy in question. The Doppler-correction factor can be obtained from a linear fit to this plot. An alternative method is to perform the gain matching process using only in-beam data. Obviously this assumes that the γ-ray energies are well established in the literature. The advantage of this method is that the calibration coefficients are obtained as a by-product with the precise Doppler correction. It should be noted that the γ rays used in the computation or calibration should originate from a rather similar evaporation channel as the nucleus of interest. The latter mentioned calibration method has been used in the analysis of the ^{66}As data, whereas both methods described above have been employed in the analysis of the ^{66}Se data. The energy resolutions of individual germanium detectors are typically around $\sim$3 keV, but the total-energy resolution of the array is worsened by 1$-$2 keV attributable to the Doppler broadening of the γ-ray peaks.

2.2.3 The gas-filled recoil separator RITU

In fusion evaporation reactions, a notable part of the primary beam passes through the target without any interaction with the target nuclei. Moreover, several other nuclear reactions, such as transfer reactions, in addition to the fusion-evaporation reactions, occur within the target foil. In order to perform RDT, the primary beam and other unwanted reaction products need to be removed from the group of recoils of interest before the recoils are transported to the implantation detector. This has been carried out with the gas-filled recoil separator RITU (Recoil Ion Transport Unit) [43, 44]. In RITU, magnetic separation between the charged beam particles and recoiling ions is performed based on their differing magnetic rigidities. RITU's ion-optical configuration is QDQQ, where Q stands for quadrupole and D for dipole magnet. The first quadrupole in front of the dipole magnet is vertically focusing, which increases the angular acceptance of recoils. The second and third quadrupoles are horizontally and vertically focusing, respectively, and are used to fine-tune the recoil distribution on to the implantation detector. RITU is filled with steadily flowing helium gas, which causes the recoils to have an average charge state via multiple scattering of the recoiling ions with the gas molecules. This increases the transmission of the reaction products through the separator system significantly, but comes at the expense of mass resolution. In heavy-element studies, for which RITU was primarily designed, this feature is desirable as there are only a few evaporation channels open. However, in the mass $A \approx 70$ region tens of different reaction channels are open, so enhanced mass resolution, which is achieved with a vacuum mode separator, would be more favourable. In addition, as the reactions needed to synthesize medium-mass nuclei below tin region are more symmetric than those used in the heavy element studies, the beam suppression properties of RITU are reduced (see section 4.2.2) [45]. However, surprisingly over the last few years RITU has been employed successfully in the study of medium-mass nuclei and useful experimental information from those nuclei have been extracted [23, 34, 36].

2.2.4 The GREAT spectrometer

The GREAT [46] (Gamma Recoil Electron Alpha Tagging) spectrometer located at the focal plane of RITU was used to detect reaction products and to measure their subsequent decay properties. It was also used to determine the decay paths and the half-lives of the isomeric excited states in some of the reaction products. GREAT comprises, in its conventional configuration, a multi-wire proportional gas-counter (MWPC), two adjacent double-sided silicon strip detectors (DSSD), a segmented planar germanium detector (24 vertical and 12 horizontal strips, which can have different gain ranges) and an array of 28 silicon PIN-diode detectors. These detectors are located inside the

GREAT vacuum chamber. A large-volume segmented clover germanium detector is installed above the DSSDs, outside the GREAT chamber. In addition, two JUROGAM II clover detectors have been recently installed on either side of the DSSDs to increase the detection efficiency for delayed γ-ray transitions. Unfortunately, these were not available in the ^{66}As experiment.

The recoiling reaction products coming from RITU pass through the MWPC filled with isobutane gas and implant into the DSSDs, where their subsequent α, β or proton decays and conversion electrons can be observed. In order to separate the isobutane gas of the MWPC from the vacuum of the GREAT chamber and from the helium gas of RITU, mylar windows are used. In the special RBT experiments presented in this thesis, the reaction energy was kept low optimising for the two particle exit channel and reducing the focal plane rate, which in turn leads to rather low recoil energies. An important improvement to the GREAT setup was the installation of thin (0.5-μm thick) separation windows into the MWPC, which minimized any unnecessary energy loss of the recoils. Hence, it was possible to increase the helium gas pressure inside RITU from 0.5 mbar up to 1.2 mbar in order to obtain better separation between the recoils and the beam before they reached the DSSDs. Each of the DSSDs comprises an active area of 60 $\times$ 40 mm with a strip pitch of 1 mm, providing 4800 pixels in total. In the present work, a new higher-pixelated DSSD has also been utilised. The details of this device and its performance are covered in sections 4.2.2 and 4.4, respectively. The silicon PIN-diode array surrounds the DSSD and is used in detection of conversion electrons and escaped α particles, but it has not been employed in the present work. The planar germanium detector is an ideal device for detecting low-energy γ rays owing to its high detection efficiency between energies of 20$-$300 keV, whereas the clover detector is more efficient for γ-ray energies above 300 keV.

The calibration of the DSSDs was carried out using a ^{133}Ba conversion electron source and a triple α source consisting of ^{239}Pu, ^{241}Am and ^{244}Cm isotopes. The same ^{60}Co, ^{152}Eu and ^{133}Ba sources as used in the JUROGAM II calibrations were used to calibrate the RITU focal-plane germanium detectors. The point-like calibration sources are not practical for the efficiency determination as the recoils are distributed over the implantation detector. Therefore, the detection efficiencies of the planar and clover detectors were simulated with the GEANT4 toolkit [47, 48, 49] and the resulting curves are presented in Fig. 2.3.

2.2.5 Ancillary instrumentation

Over the last few years, several different ancillary detector systems have been developed to be used together with the JUROGAM II + RITU + GREAT setup. One of these is the SAGE (Silicon And Germanium) spectrometer designed to measure simultaneously in-beam conversion electrons and γ rays. Another

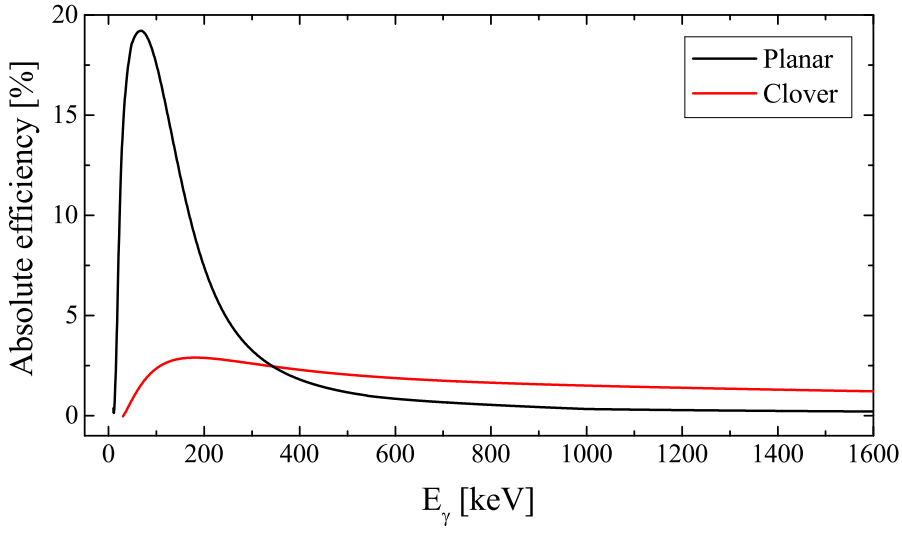

Figure 2.3: The simulated γ-ray detection efficiencies of the planar (black) and the clover (red) germanium detectors [49]. The simulation was performed with the GEANT4 toolkit [47, 48]. The experimental recoil distribution in the DSSDs (see Fig. 4.3) and the DSSD thickness (700 μm) were taken into account in the simulation.

recently developed piece of equipment is the LISA (Light Ion Spectrometer Array) spectrometer, which is used to detect fast proton and α decays at the target position. Relevant to this work are the charged-particle veto detector UoYtube (University of York tube), a phoswich scintillator and a highly-pixelated DSSD detector, which will be presented in detail in chapter 4. In the final chapter, an improved version of the UoYtube will be briefly discussed.

2.2.6 The Total Data Readout system

The electronic signals from each detector channel are handled by the triggerless total data readout (TDR) [50] system. The key idea of TDR is that there is no common hardware trigger, which allows the data from each detector channel to be recorded independently without loss of information due to a common trigger readout dead time. The common feature of the TDR system is the 100 MHz clock, which provides timestamping for the data items with 10-ns precision and synchronisation pulses to all ADCs. Data items are then arranged into a single time-ordered stream of data in collate and merge software. The data stream can be further processed in an event builder software before it is sent

to storage. Usually this is done to reduce the total amount of data, but is not necessarily required. The event builder software uses any focal plane signal as a trigger and then gathers all signals preceding the trigger signal up to $\sim$5 μs beforehand and writes them to disc.

The event parsing *i.e.,* the construction of the events is carried out in software and can be performed in variety of ways. Here, the starting point is a choice of software trigger and in this thesis, like generally with decay spectroscopy and tagging experiments, the trigger was chosen to be any signal obtained from the implantation detector. This means that a hit in the DSSD opens a time window, which defines the slice of the time-ordered data stream, covering data items both from the past and from the future with respect to the time stamp of the triggering signal, to be included in an event. Figure 2.4 shows the time structure of signals from different detector channels with respect to the time stamp of a DSSD signal. The distribution at the far left corresponds to the signals obtained from the JUROGAM II array and charged-particle detector UoYtube located at the target position. The distribution is centered around -700 ns and corresponds to the flight time of the recoils through the separator system. The peak at -150 ns originates from MWPC signals, which are generated by the recoils passing through the detector before their implantation in the DSSD. The distribution around 0 ns corresponds to the GREAT germanium detector signals, which are registered both before and after the DSSD event. The total width of the trigger can be tuned on the basis of experimental needs. The flight time of recoils depends on the reaction used and beam energy, so it may vary slightly. If the nucleus of interest contains isomeric excited states, then the trigger time window can be extended further to the future to cover the delayed γ-ray or conversion electron emission.

The event parsing is performed within the GRAIN software package designed specifically for the TDR acquisition system by P. Rahkila [51] and it is also used to sort, analyse and visualise the data either online or offline. GRAIN allows for very flexible and user-friendly data analysis by running a sorting code, which is generally written by the user. Here, the user has a variety of possibilities to visualise and extract results from the data using histograms, matrices and n-tuples. In this thesis GRAIN has been used exclusively to sort the collected data. The data analysis is also made with GRAIN for the most part, but the RADWARE software package [42, 52] has also been used to perform efficiency calibrations of JUROGAM II, $\gamma\gamma$ coincidence analysis (together with GRAIN) and peak fitting.

At present the TDR system is evolving and making use of state-of-the-art technology as a transition from analogue electronics to a fully digitized data acquisition system is in progress. The first upgrade was the installation of TNT2-D digital front-end electronics [53], which were used with the JUROGAM II clover germanium detectors in 2008. The remainder of the system, including phase 1

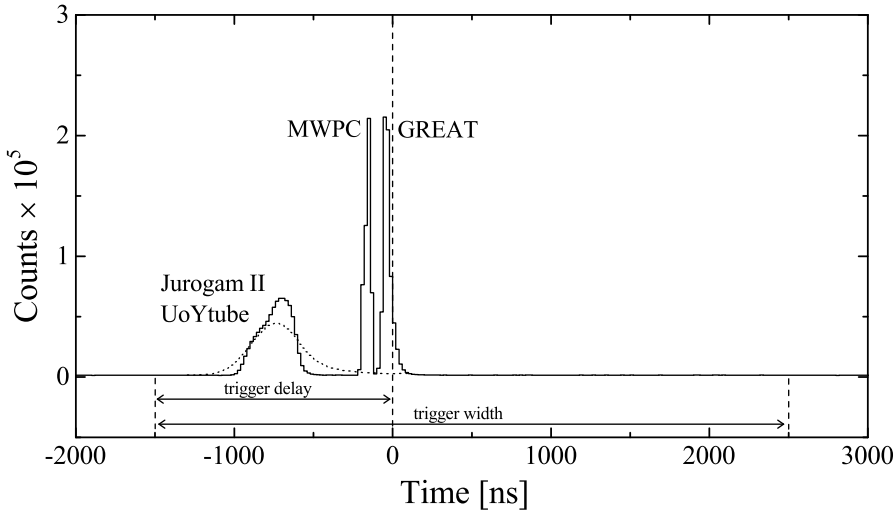

Figure 2.4: Time structure of different groups of detectors relative to the DSSD signal using a Si-OR trigger. Alternatively, the individual DSSD x-strips can be used as a trigger, but there is a positive shift of ∼100 ns in comparison to the present spectrum. Signals from the JUROGAM II (solid line) and the UoYtube (dashed line) are recorded ∼700 ns before a DSSD signal. This time difference corresponds to the flight time of the recoils through the RITU separator. Signals from the MWPC generated by the recoils passing through the detector are located ∼150 ns before a DSSD signal. The signals from the GREAT germanium detectors occur both before and after a DSSD signal.

germanium detectors, were instrumented with conventional analogue electronics (see *e.g.,* [54]). This set-up was used during the ^{66}As experiment (see chapter 3). From autumn 2009 onwards JUROGAM II has been fully equipped with commercial Lyrtech VHS-ADC cards. Here, the preamplifier signals from the detector channels are digitized in 10 ns sampling intervals with 14-bit resolution. A moving window deconvolution (MWD) algorithm [55] programmed in the FPGA of the ADC cards is used to extract the energy of the observed radiation. As more Lyrtech channels become available, more ancillary detectors are being digitised. In the most recent RBT experiment performed in spring 2013, nearly all detector channels were instrumented with Lyrtech electronics (some of the DSSD channels were still coupled to analogue electronics). The implementation of digital electronics allows higher counting rates, *i.e.,* a higher beam intensity to be used in comparison to analogue electronics, which had a 2−3 times lower data processing limit. In addition, the work presented in this thesis has benefited from the current possibility of recording pulse shapes (see section 4.2.3).

2.3 Recoil identification and recoil-β tagging

When the ^{28}Si beam was accelerated to an energy of 75 MeV and bombarded on the ^{nat}Ca target located at the center of JUROGAM II, the resulting total counting rate of the germanium array was of the order of 100 kHz. The nuclei of interest, such as ^{66}Se are produced roughly at a rate of only tens of atoms per hour, hence, the identification of the γ rays emitted by these nuclei is an enormous challenge. In order to do this, the RDT technique is used. Firstly, the reaction products are separated from the primary beam by RITU. After separation, reaction products enter the GREAT spectrometer where they first pass through the MWPC and implant into the DSSDs.

At first, the recoils are distinguished from scattered beam particles by their energy-loss (ΔE) in the MWPC and time-of-flight (ToF) obtained between the DSSD and MWPC. This is shown in Fig. 2.5(a) and (b) where the ToF is on the x axis and the ΔE on the y axis. The main recoil gate is illustrated as a red region in Fig. 2.5(a). As shown in Fig. 2.5(c) and (d), an alternative option is to plot the particle energy (E) deposited in the DSSD (x axis) against the time of flight (y axis). In these two figures the main recoil gate as defined in Fig. 2.5(a) has been employed *i.e.*, only those events falling inside this gate are plotted in Fig. 2.5(c) and (d). Here, the group of events regarded as recoils are enclosed by the green polygon. The difference between panels (a)/(c) and (b)/(d) in Fig. 2.5 is that in panels (b) and (d), reaction products associated with charged-particle evaporation have been vetoed (see section 5.1.1). As can be seen, the primary beam component is relatively enhanced in comparison to the main recoil distribution in Fig. 2.5(b) due to the fact that the beam has passed through the target without interaction; hence, charged particles are not produced. Similarly, the tail of the beam component is more pronounced in the upper left corner of Fig. 2.5(d) in comparison to the Fig. 2.5(c). Comparing Fig. 2.5(c) and (d) shows that certain parts of the particle distributions (highlighted with blue regions) are stronger in one than in the other. The enhanced distribution in Fig. 2.5(d) might be due to the transfer reaction products, which have not emitted charged particles. The corresponding distribution in Fig. 2.5(c), which is barely visible, is significantly enhanced if detection of one or more charged particles is demanded. This behaviour is not fully understood. The fact is, that the distributions enclosed by the blue polygons should not be included within the recoil gate if the nucleus of interest is produced via pure neutron evaporation. To conclude, the recoil definition made initially on the basis of the ToF$-\Delta E$ information does not provide the cleanest possible recoil gate in the case of the ^{28}Si + ^{nat}Ca reaction. Therefore, the $E-$ToF approach has been used solely in the analysis of ^{66}Se data as it provides a more detailed picture of the reaction product distributions. Moreover, as can be seen in Fig. 2.5(c) and (d), the energy distribution of the recoils extends from 1 MeV up to 6 MeV *i.e.,* they have lost $\sim$80 % of their initial energy after formation due to the

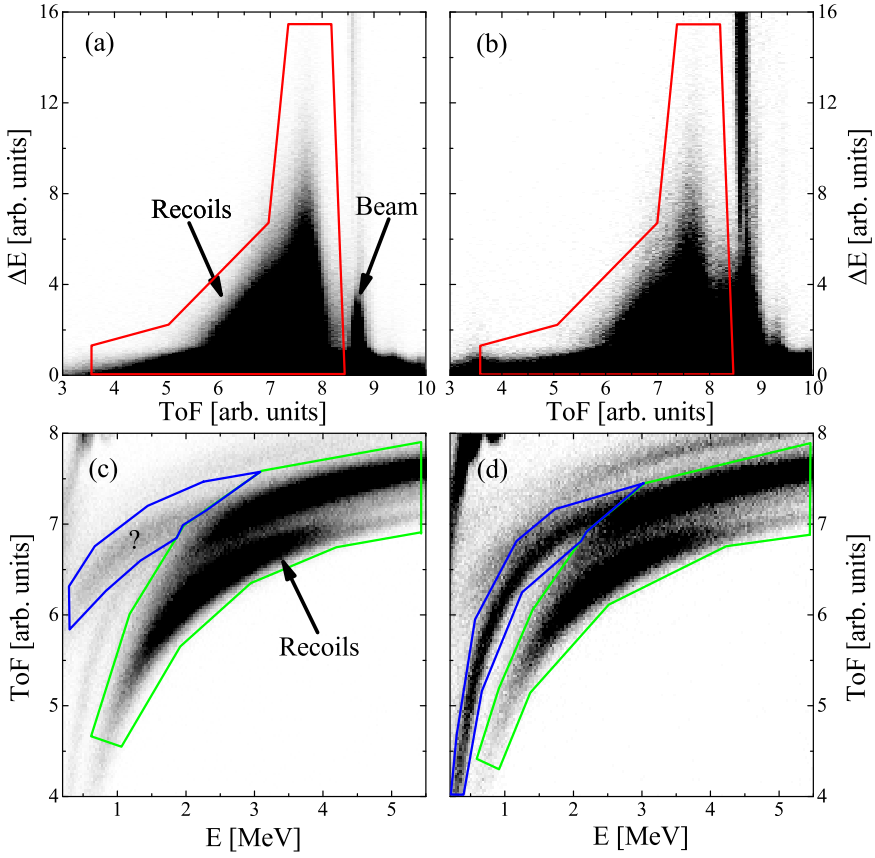

Figure 2.5: Recoil identification using: (a),(b) the ToF$-\Delta E$ method and (c),(d) $E-$ToF method. The red regions in panels (a), (b) and the green regions in panels (c), (d) indicate the group of events regarded as recoils. Further details are explained in the text.

collisions with RITU He gas molecules, passing through the MWPC and the pulse height defect of the DSSD. Therefore, the installation of the thinnest possible gas separation windows in the MWPC was crucial while the higher gas pressure in RITU helps to obtain a better separation (see section 2.2.4).

After successful recoil identification, the prompt γ rays observed at the target position were associated with the recoils. Here, the signals recorded in JUROGAM II within -1 to -0.5 μs before the recoil implantation are consid-

ered, hence, the γ rays are recoil gated. In Fig. 2.6(a) a triggered JUROGAM II singles γ-ray spectrum is illustrated, whereas in Fig. 2.6(b) the recoil gate, as defined in Fig. 2.5(c), has been employed. In both of these spectra the dominant peaks originate from γ-ray transitions in ^{65}Ga. As can be noted, the recoil gating does not provide a marked difference compared to the triggered spectrum. This differs significantly from the studies made in the very heavy mass region, where the recoil gating might be already enough to identify γ rays originating from the nucleus of interest (see *e.g.,* Ref. [56]). Therefore, an additional discriminating feature *i.e.,* a tag, arising from the radioactive decay of the product, has to be employed. In this thesis only β decaying nuclei are considered, but this poses a problem since, as stated earlier, β decay properties are not generally suitable for tagging purposes. However, the medium-heavy odd-odd $N = Z$ and even-even $N < Z$ nuclei have β-decay properties, which can provide a (clean) tag for prompt or delayed γ-ray transitions. Nuclei residing in this region of the nuclear chart are generally Fermi superallowed β emitters. They are characterised by relatively short half-lives ($\sim$100 ms) and high β-decay energies up to $\sim$10 MeV in comparison to other nuclei in this region, which have longer half-lives (from seconds to hours) and lower β-decay energies ($\leq$ 3 MeV). Therefore, the β-decaying nucleus of interest can be identified according to the three following conditions (in order of importance):

- The β decay of the recoil, occurring in the same pixel of the DSSD as the recoil implantation, takes place within the set correlation time, which is of the order of 100$-$300 ms. Here, ΔE signal is generated by a β-particle passing through the DSSD.
- The emitted β particle is recorded in coincidence with the DSSD signal in a detector element (planar germanium or plastic scintillator detector) located downstream from the DSSD. Here, the full E signal is generated by a β-particle.
- The full energy of the β particle measured in the planar germanium or plastic scintillator detector meets the energy conditions dictated by a 2 dimensional $\Delta E - E$ gate.

The identification of β particles is performed by detecting coincidences between the DSSD and the planar germanium (or plastic scintillator) detector within a short time gate of 0$-$200 ns. As the DSSDs are usually rather thin, *i.e.,* between 300$-$700-μm thick, the β particle penetrates through the silicon and deposits only part of its energy (ΔE) into the detector. In RBT experiments 700-μm thick DSSDs have always been preferred instead of the more common 300-μm ones to maximize the energy loss signals of the β particles. The energy loss of the β particles in the 700-μm thick DSSDs is around 400 keV and the stopping power of the emitted β particles in the DSSD is nearly constant due to their kinetic energy.

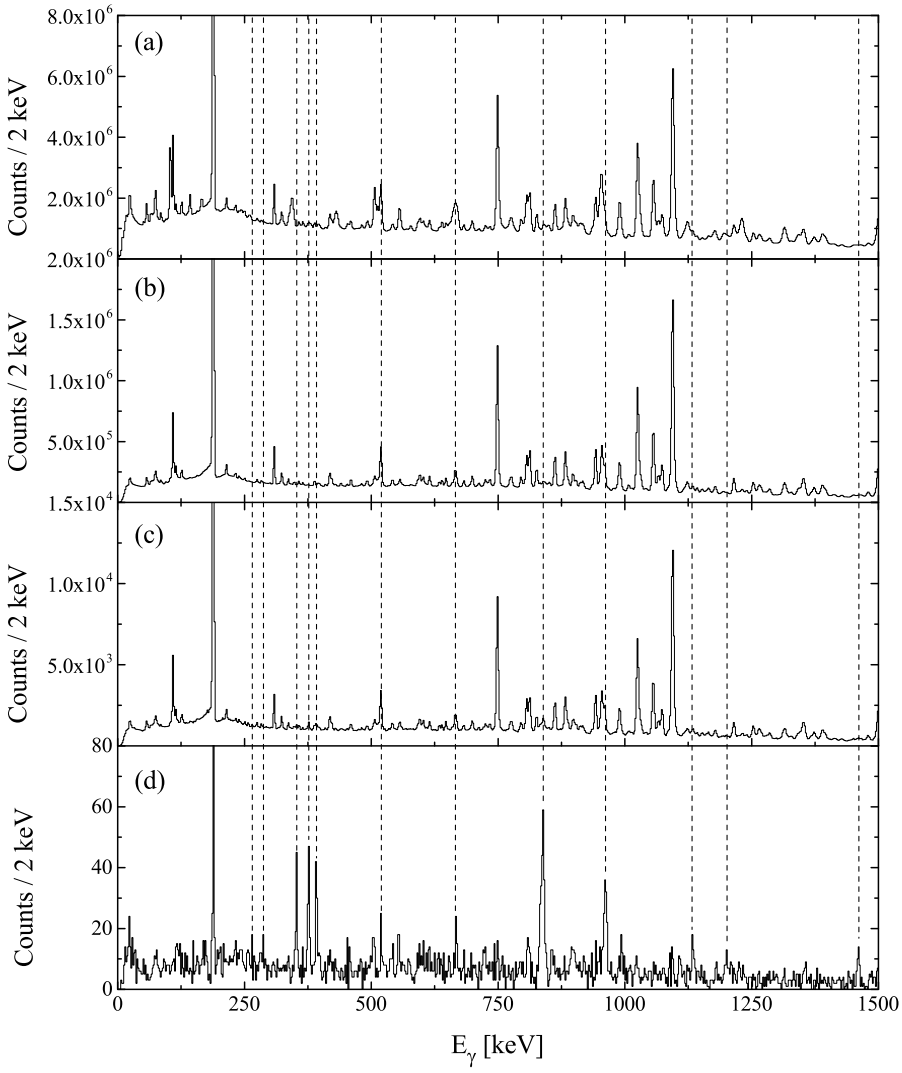

Figure 2.6: The JUROGAM II singles γ-ray spectra: (a) triggered, (b) recoil gated and (c) recoil-β tagged with 300 ms correlation time but without an energy requirement on the β particles. (d) same as (c) but using a β gate of 4.5−10 MeV. The dashed line indicates transitions from ^{66}As. See text for further details.

After passing through the DSSD, the β particle is fully stopped in the planar germanium (or plastic scintillator) detector, where the remaining energy (E) of the β particle is measured (using 12 horizontal strips with an effective gain range up to ∼14 MeV). It should be noted that the coincidence condition between the DSSD and the planar germanium detector suppresses the distracting γ-ray background in the planar germanium detector as the interaction of a γ ray both in the DSSD and in the planar is highly unlikely. A practical way to visualise the observed β-particle distribution is to form a $\Delta E - E$ matrix as illustrated in Fig. 2.7. Here, the β particles to be correlated with the recoils are selected by setting a two-dimensional energy gate (called β gate hereafter) around the desired part of the distribution. The size of the gate, or to be exact, only the low-energy threshold with respect to y axis can be conveniently varied to optimise for maximum statistics or cleanliness of the tagged radiation spectra.

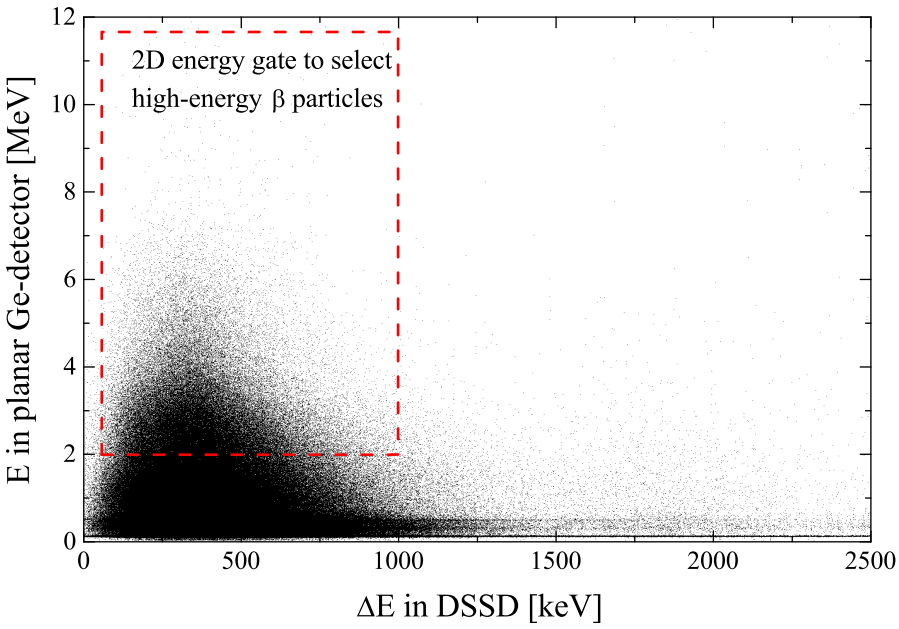

Figure 2.7: Identification matrix for high-energy β particles. The energy-loss information (ΔE) is obtained from the DSSD (x axis) and full energy information (E) from the planar germanium detector (y axis). A two-dimensional energy gate can be applied to select β particles to be correlated with recoils within a desired correlation time. The low-energy detection threshold can be varied in order to achieve better statistics or cleanliness of the tagged spectra.

The β-tagged JUROGAM II singles γ-ray spectrum is illustrated in Fig. 2.6(c). Here, all β particles that have been observed (both in the DSSD and in the planar detector) within 300 ms from the recoil implantation, regardless of their full energy, are used in the tagging process. The general shape of the spectrum does not differ significantly from the recoil-gated one shown in Fig. 2.6(b), but the γ-ray transitions originating from ^{66}As just start to exceed the background level. However, when the energies of the observed β particles are required to lie between $E = 4.5-10$ MeV (as measured in the planar detector), the identification of the ^{66}As γ-ray transitions is evident, while some contamination from ^{65}Ga still persists.

A similar type of procedure, as described above, is also possible for the delayed γ-ray transitions detected at the focal plane of RITU. The delayed γ rays measured with the planar germanium detector (using 24 vertical strips with an effective gain range up to $\sim$400 keV) are illustrated in Fig. 2.8. Here, the conditions in each panel are exactly the same as used in Fig. 2.6. The only difference is that in Fig. 2.8(b),(c) and (d), the planar signals occurring within $0-24$ μs after the DSSD signal are associated with the recoils. The large peak at 115 keV in Fig. 2.8(a) and (b) originates from the β decay of ^{65}Ga feeding an excited state in ^{65}Zn. As was observed earlier, with the recoil-β tagging, the identification of transitions originating from the isomeric states in ^{66}As is evident as illustrated in Fig. 2.8(d). It should be noted that the 114-keV transition in ^{66}As overlaps with the one in ^{65}Zn and therefore these two lines are mixed in Fig. 2.8(c). The delayed γ-ray transitions can be employed as a tag in similar fashion as the β particles for the prompt γ-ray transitions in JUROGAM II. Moreover, these two tagging methods can be combined to obtain ultimate selectivity.

2.4 Selectivity of recoil-β tagging

Tagging with β particles is a lot more complicated procedure when compared to conventional α tagging. The major difficulty relates to the clean identification of the nucleus of interest, which is hindered by two factors, namely false correlations and a fast reduction in statistics when the low-energy β threshold is raised. In the following section these two effects with other related details of the RBT analysis are discussed.

The search for correlated event chains *i.e.,* recoil-β pairs (or recoil-β-β triplets) in the DSSD always starts from a fixed event, such as recoil implant or β decay. In GRAIN the DSSD events are stored into the time-ordered list called a tagger, which can be read backwards with respect to time. If the good β-particle candidate, identified on the basis of the DSSD-planar energy and coincidence time conditions, is chosen as a starting point, then the search for the preceding

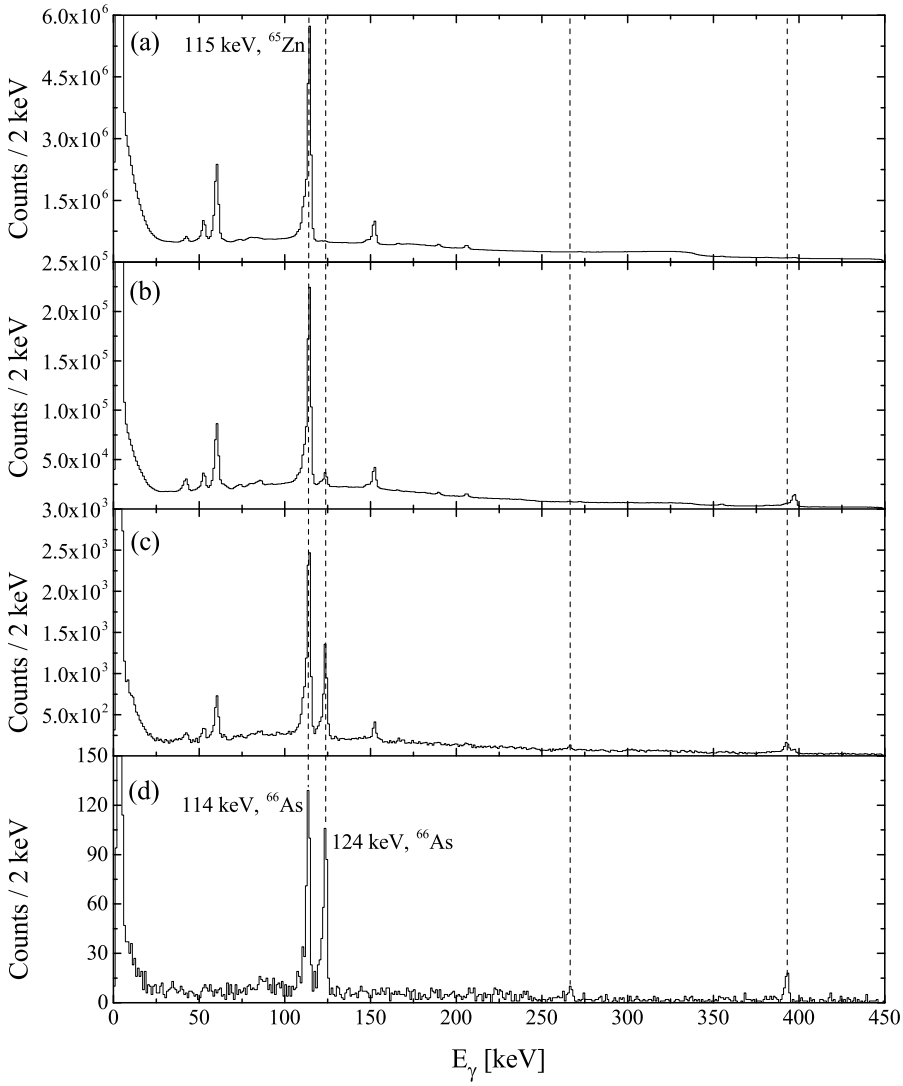

Figure 2.8: The planar germanium detector γ-ray spectra: (a) raw, (b) recoil gated and (c) recoil-β tagged with 300 ms correlation time but without an energy requirement on the β particles. (d) same as (c) but using a β gate of 4.5−10 MeV. The dashed line indicates transitions from ^{66}As. See text for further details.

DSSD event, which should be a recoil by nature, is performed. This event has to fulfill the search time, position, energy and ToF criteria in order to form a pair with the β particle. However, it is always possible that an acceptable recoil event has occurred between the true recoil-β pair. This scenario leads into the unpleasant occurrence of false correlations, which can not be corrected or eliminated within the analysis software. The false correlations become more probable when the counting rate in the DSSD is high ($\sim$6$-$10 kHz for the cases covered in this thesis) or if the nucleus of interest has a long half-life. Another form of false correlations is the coincidence summing of two low-energy β particles appearing as one high-energy β event.

In the case of heavy or super-heavy element studies, the number of possible evaporation channels is typically limited to one or two exit channels, whereas at the mass $A = 70$ region, tens of different evaporation channels are open with reasonably high cross-sections. This is illustrated in Table 2.1, where some of the residual nuclei produced in the ^{28}Si + ^{nat}Ca reaction are listed with their respective β-decay properties and calculated yields. The yields are calculated with the PACE4 code [57] and the obtained numbers give only a rough estimate of the relative strengths of different evaporation channels. According to the calculation (see Table 2.1), the strongest evaporation channels involve emission of charged particles and especially evaporation of α particles. However, since the α evaporation significantly broadens the angular cone of the recoils, which in turn causes suppression in the RITU transmission, the multiple proton exit channels appear to be the strongest in recoil-gated spectra. Taking into account the subsequent β decays of the various reaction products, the total counting rate at the focal plane of RITU increases rapidly as a function of the beam intensity and energy. This, in turn, increases the risk for false correlations and hinders the identification process based on the short half-life and high β-end-point energy of the nucleus of interest. This problem is evident, for example, in Fig. 2.6(d) where the relatively strong contamination from ^{65}Ga persists although the β threshold used exceeds the β-end-point energy of ^{65}Ga by 2 MeV. The influence of the beam intensity on the false correlations is shown in Fig. 2.9 as a solid and dashed blue curves. Here, the index of false correlations is defined to be the ratio of the ^{65}Ga 191-keV transition intensity and the number of β particles falling inside the energy gate. Clearly, when the beam intensity is reduced (dashed curve), the false correlations are on a more manageable level, although not removed completely.

The second difficulty in the identification process relates to the continuous energy distributions of β particles, which are originating from various evaporation channels and as discussed above, involving mostly charged-particle evaporation. Obviously, the β particle distributions are also overlapping with each other and hence, do not permit absolute selectivity. As mentioned earlier, the identification of the nucleus of interest relies partly on the high-energy of the β particles (in addition to the short half-life), but the usage of a high β threshold dimin-

Table 2.1: The calculated relative yields (Y) of residual nuclei for some of the (strongest) evaporation channels in the ^{28}Si + ^{nat}Ca reaction. The calculation has been carried out using the PACE4 code [57]. The natural abundance [$A(^{xy}\mathrm{Ca})$] of each Ca isotope is given after the reaction equation (^{46}Ca is omitted due to the low abundance of 0.004 %). The decay properties ($t_{1/2}$ and Q_{EC}) of the reaction products are obtained from Ref. [58].

Nucleus	Channel	$t_{1/2}$	Q_{EC} [MeV]	Y [%]
		^{28}Si + ^{40}Ca, $A(^{40}\mathrm{Ca})$ = 96.943 %		
^{66}As	pn	95.8 ms	9.6	2.6
^{66}Se	2n	35.0 ms	10.7	0.002
^{62}Zn	α2p	9.2 h	1.6	36.3
^{65}Ga	3p	15.2 m	3.3	27.9
^{63}Ga	αp	32.4 s	5.7	8.1
^{59}Cu	2αp	81.5 s	4.8	6.6
^{65}Ge	2pn	30.9 s	6.2	6.4
^{66}Ge	2p	2.3 h	2.1	6.2
^{62}Ga	αpn	116.1 ms	9.2	1.1
^{64}Zn	4p	stable	stable	0.5
		^{28}Si + ^{42}Ca, $A(^{42}\mathrm{Ca})$ = 0.647 %		
^{64}Zn	α2p	stable	stable	26.8
^{67}Ge	2pn	18.9 m	4.2	17.8
^{61}Cu	2αp	3.3 h	2.2	12.8
^{64}Ga	αpn	2.6 m	7.2	11.7
^{67}Ga	3p	3.3 d	1.0	9.8
^{65}Ga	αp	15.2 m	3.3	4.7
		^{28}Si + ^{43}Ca, $A(^{43}\mathrm{Ca})$ = 0.135 %		
^{68}Ge	2pn	271 d	0.1	24.4
^{65}Ga	αpn	15.2 m	3.3	19.3
^{62}Cu	2αp	9.7 m	4.0	12.7
^{65}Zn	α2p	243.9 d	1.4	12.7
^{68}As	p2n	151.6 s	8.1	6.4
^{62}Zn	2αn	9.2 h	1.6	5.0
		^{28}Si + ^{44}Ca, $A(^{44}\mathrm{Ca})$ = 2.086 %		
^{66}Ga	αpn	9.5 h	5.2	25.1
^{69}Ge	2pn	39.1 h	2.2	19.8
^{69}As	p2n	15.2 m	4.0	12.4
^{66}Zn	α2p	stable	stable	8.0
^{63}Cu	2αp	stable	stable	7.6
^{63}Zn	2αn	38.5 m	3.4	5.8
		^{28}Si + ^{48}Ca, $A(^{48}\mathrm{Ca})$ = 0.187 %		
^{70}Ge	α2n	stable	stable	19.2
^{73}As	p2n	80.3 d	0.3	17.9
^{73}Se	3n	7.2 h	2.7	14.5
^{72}As	p3n	26.0 h	4.4	14.0
^{72}Se	4n	8.4 d	0.4	7.6
^{70}Ga	αpn	21.1 m	0.7	6.8

ishes the amount of statistics. This is illustrated in Fig. 2.9, where the amount of statistics (black curve) in the case of the ^{66}As JUROGAM II singles γ-ray data is plotted as a function of the β-threshold energy. Here, the amount of statistics is derived simply from the intensity of the 963 keV line ($2^+ \rightarrow 0^+$ transition in ^{66}As) at each threshold energy. For example, if the threshold is raised from 1 MeV to 2 MeV, the drop in statistics is ∼60 %. Moreover, if the nucleus of interest is produced with a very-low cross-section of the order of 100 nb, the number of detected high-energy β particles can be expected to be nearly non-existent on the basis of the shape of the Fermi-Kurie distribution. Therefore, almost the entire distribution of β particles ranging from a few hundred keV up to the calculated or measured end-point energy has to be considered in the tagging process. This does not necessarily pose an insurmountable problem if the evaporation channel can be selected with sufficient sensitivity. It should also be noted that the discrimination between the odd-odd $N = Z$ ($T_z = 0$) and even-even $N = Z - 2$ ($T_z = -1$) nuclei in the mass $A = 70$ region is challenging as the β-decay properties in both cases are very similar. This behaviour can be understood on the basis of the odd-odd and even-even mass parabolas.

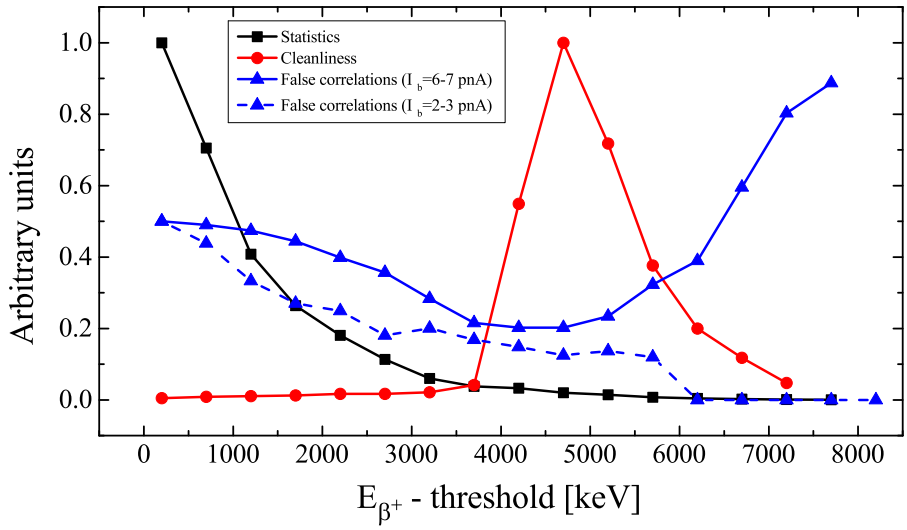

Figure 2.9: Illustration of the RBT data quality in the case of the β-tagged JUROGAM II γ-ray spectrum. The available ^{66}As statistics as a function of the β-threshold energy is shown as a black curve. The cleanliness is defined as the ratio of ^{66}As and ^{66}Ge. The false correlations (dashed and solid blue curves) are defined as ratio of the ^{65}Ga 191-keV line intensity and the number of β particles within the tagging gate.

In practise the analysis of the β-tagged γ ray data proceeds so that at first, the candidates for the γ-ray transitions originating from the nucleus of interest are resolved with a high β threshold (if allowed by the cross-section of the reaction channel) from the JUROGAM II singles spectrum. The usage of n-tuples in GRAIN is very convenient and speeds up the identification process as re-sorting the data is not needed upon a change in the tagging conditions. After successful identification, it is still advisable to check and exclude the possibility of contaminating transitions as the falsely correlated events may still remain in the γ spectrum despite the strict tagging conditions. In the mass $A = 70$ region, the 3 proton (3p) evaporation channel, such as ^{65}Ga in the case of the ^{28}Si + ^{40}Ca reaction, is generally the strongest observed in the RBT experiments. This is followed by the 2p (^{66}Ge) and 2pn (^{65}Ge) channels, respectively. Hence, it is desirable that the level schemes of the nuclei produced via the aforementioned reaction channels are well established in the literature in order to avoid false assignments. When using the ^{nat}Ca target, it is also important to be aware of the possible contamination originating from the reactions with heavier Ca isotopes (see Table 2.1). However, since the abundances of the ^{42,43,44,46,48}Ca isotopes are not so significant and the reaction products are around the line of stability, the contribution from these reactions is typically removed by the applied β-tagging conditions. In the present study only one nucleus originating from such a reaction channel was identified. This was ^{69}Ge produced from 2pn channel of the ^{28}Si + ^{44}Ca reaction.

The accurate identification of ^{66}As γ rays was achieved with a β threshold of $\sim$4.5 MeV. In Fig. 2.9 the cleanliness is defined as the ratio of the ^{66}As and ^{66}Ge $2^+ \rightarrow 0^+$ transitions, and as can be seen, the maximum cleanliness is achieved at 4.7 MeV. The ^{66}Ge is used to define the cleanliness as the cross-section for the 2p channel is $\sim$5 times smaller than the one for the 3p channel and, therefore, the γ rays originating from ^{66}Ge are significantly less falsely correlated if at all in contrast to the ^{65}Ga. It should be noted that when the maximum cleanliness is achieved, only 2 % of the initial ^{66}As statistics is available. In the next phase, if permitted by the statistics, a $\gamma\gamma$ analysis can be performed, but this may necessitate that the tagging conditions are significantly "relaxed". Here, it is advisable to start from a rather low β threshold to maximise the statistics and then gradually raise the threshold in a few hundred keV steps until a clean gated spectrum is achieved. Typically, a better cleanliness can be achieved earlier in the gated spectrum *i.e.,* with a lower threshold energy in comparison to the singles spectrum (only if the gating transition is not overlapping with any of the contaminant transitions). However, the candidate coincident γ rays should be examined again and carefully to avoid misassigning them to the contaminant transitions. These key principles have been employed in the analysis of the ^{66}As data discussed in chapter 3.

Many of the problems presented in this section hampered the analysis of the ^{66}As data (as well as preceding data sets) and led to a discovery of development

needs in the instrumentation. The new devices to enhance the sensitivity and selectivity of the RBT approach are discussed in chapter 4. The most recent development in the instrumentation together with the new experimental data on the $N = Z - 2$ nucleus ^{74}Sr are presented in the final chapter.

Chapter 3

Recoil-β tagging study of the $N = Z$ nucleus ^{66}As

In this chapter the experimental details and results of an in-beam and isomer-decay study of $N = Z = 33$ nucleus ^{66}As will be presented. The main goal of this experiment was to identify the $T = 1$ excited states, which led to the observation of candidates for the $4^+ \rightarrow 2^+$ and $6^+ \rightarrow 4^+$ transitions in the $T = 1$ band. These results have allowed the computation of Coulomb energy differences between the analogue states in ^{66}Ge. In addition, the properties of the isomeric structures have been measured with improved accuracy and several prompt γ-ray transitions from excited states, both bypassing and decaying to the isomeric states in ^{66}As, have been observed for the first time. The experimental results are compared with shell-model calculations using the modern JUN45 interaction in the $pf_{5/2}g_{9/2}$ model space.

3.1 Experimental details

The experiment was performed in 2009 at the Accelerator Laboratory of the University of Jyväskylä, where the beam was delivered by the K-130 cyclotron. The ^{40}Ca(^{28}Si,pn)^{66}As reaction was employed at beam energies of 83 MeV (40 h of irradiation time) and 75 MeV (120 h of irradiation time) to populate excited states in ^{66}As. The ^{28}Si beam impinged on a $^{\mathrm{nat}}$Ca target rolled to a thickness of 800 μg/cm^2, with an average beam intensity of 5 pnA. Prompt γ rays were detected at the target position by the JUROGAM II γ-ray spectrometer. Fusion-evaporation recoils were separated from the primary beam and other unwanted reaction products by the gas-filled recoil separator RITU. Good sep-

aration between the beam and the recoils was obtained with a RITU gas pressure of 1.2 mbar. After separation, reaction products were further identified using methods described in the section 2.3 *i.e.,* using ToF$-\Delta E$ and $E-$ToF information obtained from the MWPC and DSSD detectors. The GREAT clover- and planar-type germanium detectors installed around the DSSDs were used to observe delayed γ-ray transitions at the focal plane of RITU. The planar germanium detector was also used for detecting the high-energy β particles in coincidence with the energy-loss signal obtained from the DSSD within a 0$-$200-ns time gate. The software packages GRAIN [51] and RADWARE [42, 52] were used to analyse the collected data.

The exceptional β-decay properties of ^{66}As are suitable for successful tagging due to the short half-life of $\sim$96 ms [59, 60, 61] and high β-end-point energy of $\sim$9.6 MeV [62, 63]. This results from the fact that the ground state of ^{66}As has a Fermi superallowed β decay to the daughter ^{66}Ge. The selection of high-energy β particles was performed in similar manner as explained in the section 2.4. The correlation time of 300 ms, which is approximately three times the β-decay half-life of ^{66}As as reported in Refs. [59, 60, 61], was used in the analysis. Shorter correlation times such as 150 to 200 ms were investigated but this did not significantly help to increase the cleanliness of the tagged spectra. The low-energy threshold for the β particles was varied between 0.5$-$5 MeV during the analysis of the correlated γ-ray transitions in order to optimise for maximum statistics or for the cleanliness of the tagged spectra. The transitions originating from excited states in ^{66}As were first identified with very strict tagging conditions, *i.e.,* with high β-particle energy threshold of the order of $\sim$3$-$5 MeV. The threshold was then relaxed to $\sim$0.5$-$3 MeV in order to perform prompt $\gamma\gamma$ and angular distribution analysis with sufficient statistics.

3.1.1 Angular distributions of γ-ray transitions

The multipolarities of the strongest γ-ray transitions originating from ^{66}As were deduced by means of angular distributions [64, 65] and angular distribution ratios [66, 67]. For γ-ray angular distributions, β-tagged, β- and isomer-tagged, or only isomer-tagged prompt events were sorted separately into four spectra corresponding to different rings of detectors (see section 2.2). The intensities of the γ rays of interest were extracted from each spectrum and normalised by the detection efficiency of the corresponding ring. The angular distribution function in the case of partially aligned nuclei can be expressed as [65]:

$$W(\theta) = 1 + \alpha_2 A_2^{\max} P_2(\cos\theta) + \alpha_4 A_4^{\max} P_4(\cos\theta), \tag{3.1}$$

where $A_2^{\max}$ and $A_4^{\max}$ are the angular distribution coefficients when the spins are completely aligned, α_2 and α_4 are the attenuation coefficients, which take

into account the partial alignment. $P_2(\cos\theta)$ and $P_4(\cos\theta)$ are the second and fourth order Legendre polynomials, respectively. Precise determination of the $A_2^{\max}$ and $A_4^{\max}$ coefficients yields information on the spins and parities of the states involved in the transition and multipole mixing, but this requires plenty of γ-ray data. If the possible multipole mixing is ignored, which is equivalent to setting the $A_4^{\max}$ to zero [68], a first order estimate of the transition multipolarity can be achieved by fitting the reduced angular distribution function

$$W(\theta) = A_0[1 + A_2 P_2(\cos\theta)], \tag{3.2}$$

to the detection angle vs γ-ray intensity plot. In Eq. 3.2 the parameter A_0 reflects the amount of data whereas parameter A_2 can be used to deduce the transition multipolarity: a positive value indicating a quadrupole character and a negative value a dipole character. Examples of measured angular distributions and fits for the ^{66}As γ rays are illustrated in Fig. 3.1.

The angular distribution ratios (R) were deduced by two methods depending on the γ-ray transition intensity and cleanliness. The R values were extracted from three $\gamma\gamma$ matrices, which were formed by sorting β-tagged coincidence events with (133.6° + 157.6°) vs (all angles), (104.5°) vs (all angles) and (75.5°) vs (all angles) combinations. By setting the same energy gates on the y axis (all angles) in each matrix, three coincidence spectra were formed representing the aforementioned detection angles. The intensity of the γ ray to be studied was again extracted from the spectra and normalised for the detection efficiency. The angular distribution ratio was calculated with the formulae

$$R_1 = \frac{I_\gamma(133.6° + 157.6°)}{I_\gamma(104.5°)} \quad \& \quad R_2 = \frac{I_\gamma(133.6° + 157.6°)}{I_\gamma(75.5°)}, \tag{3.3}$$

thus providing two R values for each transition from which the final value was calculated as a weighted average (see Table 3.2). Alternatively, two β-tagged (or β- and/or isomer tagged) singles γ-ray spectra corresponding to the sum of angles (133.6° + 157.6°) and (104.5° + 75.5°) with two different β-particle energy gates (large gate = 0.5−10 MeV and small gate = 3−10 MeV) were used to compute the R value. The resulting R values with error estimates for the ^{66}As γ-ray transitions are listed in Table 3.2, where the method used is also indicated. Transitions of known multipolarities originating from nuclei populated via other reaction channels were analysed with the methods described above, yielding, on average, angular distribution ratios of 1.30(7) for stretched $\Delta I = 2$, $E2$ and 0.70(6) for stretched $\Delta I = 1$, $M1$ and $E1$ type of transitions. It should be noted that the method described above can not unambiguously distinguish between either pure $\Delta I = 0$ dipole and stretched $E2$ transitions or stretched dipole and unstretched/mixed $E2$ transitions [66].

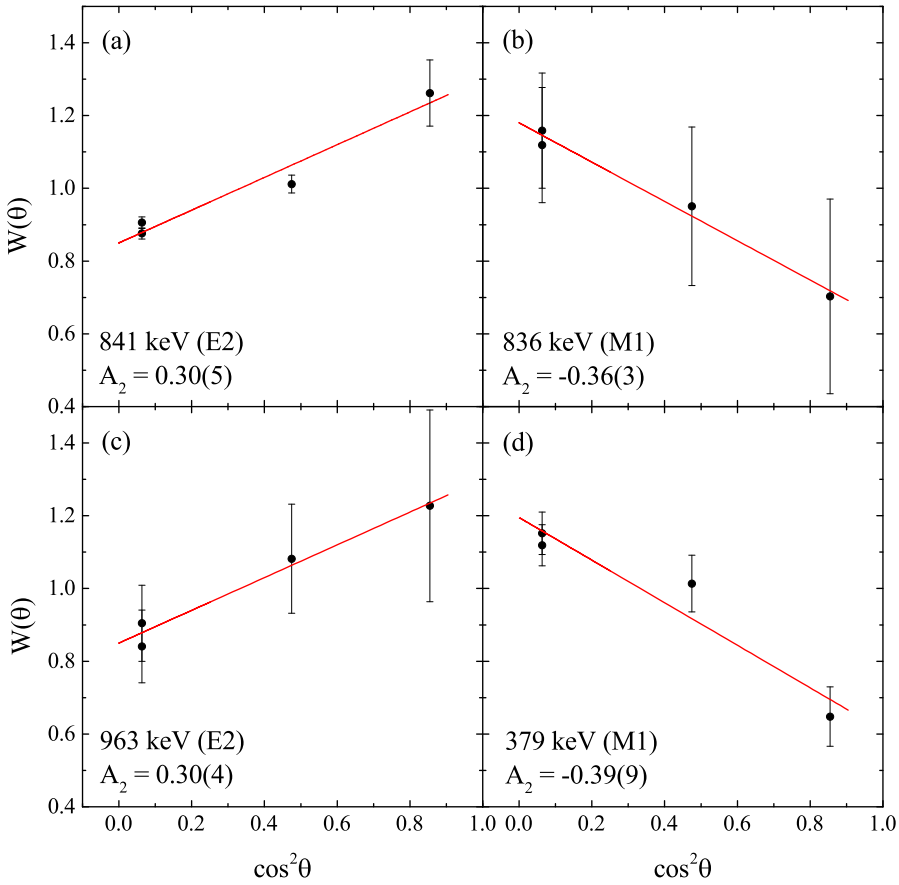

Figure 3.1: Typical angular distributions measured for ^{66}As γ-ray transitions. Angular distribution data and fits (see Eq. 3.2) are illustrated for (a) 841-keV, (b) 836-keV, (c) 963-keV and (d) 379-keV transitions. The data and fitted curves are normalised by the A_0 coefficient in each case. Due to the symmetry of the JUROGAM II rings at the angles of 104.5° and 75.5°, the data points at the left in each panel fall on top of each other. Full details of the method are explained in the text.

3.2 Results

The level scheme of ^{66}As constructed in the present work is shown in Fig. 3.2. Details of the measured γ-ray transitions are listed in Tables 3.1 and 3.2. These results are based on the prompt, delayed and delayed-prompt $\gamma\gamma$ coincidence analysis. Isomeric structures in ^{66}As have been previously studied by Grzywacz *et al.*, leading to the discovery of two isomeric states and nine connecting γ-ray transitions [69]. Recently an in-beam study performed by de Angelis *et al.,* [70] provided information on several new γ-ray transitions bypassing the isomeric states. In the following section, results from the present data concerning both the isomeric and prompt structures are presented. A comparison to the previous works is carried out and discrepancies are discussed.

3.2.1 Isomeric states in ^{66}As

The delayed γ-ray transitions, which were identified in Ref. [69], were also observed in the present study. This is illustrated in Fig. 3.3(a) and 3.3(b) where the β-tagged delayed ^{66}As singles γ-ray spectra recorded in the planar and GREAT clover detectors, respectively, are presented. Coincidence relations between transitions below the isomeric states can be seen in Fig. 3.4, where β-tagged and gated γ-ray spectra from a planar-clover matrix are illustrated. The γ rays detected in the clover detector in coincidence with the 114-keV γ rays seen in the planar detector are shown in panel (a). Similarly, in panel (c) γ rays seen in the clover detector coinciding with the γ rays at 124 keV seen in the planar detector are presented. In panels (b) and (d) the same data are illustrated as in panels (a) and (c) but there is now a narrow $\gamma\gamma$ time window of 100 ns added to identify only prompt coincidences. The time gate on the γ_{planar}-recoil time difference was set to 0$-$21 μs ($\approx 3 \times t_{1/2}^{114\ \text{keV}}$) in all panels of Fig. 3.4. A comparison between panels (a) and (b) immediately reveals that the 124-keV transition is directly depopulating one of the isomeric states as the line at 124 keV disappears when imposing the prompt coincidence time gate. All of the other seven γ-ray peaks still remain in prompt coincidence with the 114-keV line when the $\gamma\gamma$ time gate is applied, indicating that the 114-keV transition is also directly de-exciting the other isomeric state. Comparing panels (c) and (d) confirms the conclusions made above, since the 124-keV line is no longer to be seen in coincidence with the 114- and 1553-keV lines after the narrow $\gamma\gamma$ time gate is added. In addition, the isomeric state depopulated by the 124-keV line has to lie lower in excitation energy as it is fed from above by the 1553-keV γ-ray transition. The ordering of the 114- and 124-keV transitions was further confirmed by comparing the time stamps of these decay events. This was possible due to the time stamping with 10-ns precision of each data event in the TDR system. A comparison of the time stamps for the

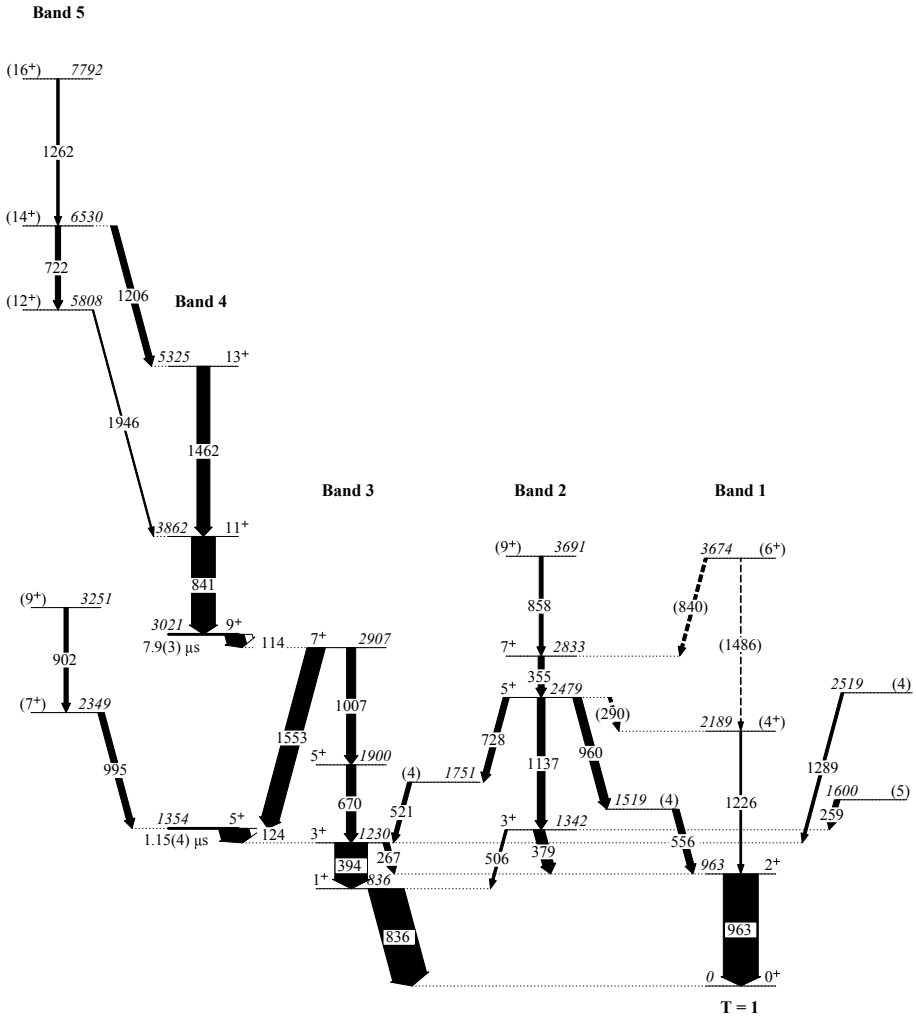

Figure 3.2: Level scheme of ^{66}As derived from the present data. The width of the arrow corresponds to the intensity of the transition. The intensities of the γ-ray transitions observed only in JUROGAM II are extracted from β-tagged JUROGAM II singles data with 1−10-MeV β gate and are used in this figure (see Table 3.2). The illustrated intensities for the 114-, 124-, 267-, 394-, 670-, 836-, 1007- and, 1553-keV γ-ray transitions are obtained from the RITU focal plane data (see Table 3.1).

114- and 124-keV $\gamma\gamma$ coincidences leads to the conclusion that in 98 % of the detected coincidences, the 114-keV transition precedes the 124-keV transition. The missing 2 % is due to random coincidences with the background events, which are unavoidably included to some extent in the energy gates.

The 1007- and 670-keV γ-ray transitions are seen in coincidence only with the 114-keV γ-ray transition, which indicates that they bypass the lower-lying isomeric state. On the other hand, the 1553-keV line is seen in coincidence with both the 114- and 124-keV lines and, as stated earlier, the 1553-keV transition precedes the 124-keV transition, as does the 114-keV transition. This leads to the conclusion that the isomeric states are connected by the consecutive 114- and 1553-keV γ rays. The sum of energies of the 124- and 1553-keV γ-ray transitions equals the sum of the 670- and 1007-keV transitions, which are assigned to form a parallel cascade with the 124- and 1553-keV transitions. When imposing the narrow $\gamma\gamma$ time gate on the spectrum gated by the 124-keV γ-ray transition, coincidences are only observed with the 267-, 394-, 836- and 963-keV transitions as illustrated in Fig. 3.4(d). This confirms that the previously mentioned transitions must originate from states lying below the lower-lying isomeric state.

Recoil-gated spectra from the planar-clover matrix are presented in Fig. 3.5 showing γ-ray transitions observed in the clover detector in coincidence with the 394- and 267-keV transitions detected in the planar. The reduction in statistics from β-tagging added to the drop in γ-ray detection efficiency of the planar detector above 150 keV did not permit a β-tagged $\gamma\gamma$ analysis for these transitions. Observed coincidences presented in Fig. 3.5 show that the 670-, 836- and 1007-keV γ-ray transitions are in coincidence with the 394-keV transition and that the 670-, 963- and 1007-keV transitions are in coincidence with the 267-keV transition. As the 267- and 394-keV lines are not seen in mutual coincidence and the sum of energies of the 267- and 963-keV transitions equals the sum of the 394- and 836-keV transitions, it can be concluded that they form parallel cascades depopulating a state at 1230 keV. This state is fed by the 670-keV / 1007-keV cascade from a state at 2907 keV. The ordering of the γ-ray transition pairs with energies of 670 keV / 1007 keV, 394 keV / 836 keV and 267 keV / 963 keV cannot be unambiguously assigned at this stage. This will be established later on by prompt $\gamma\gamma$ analysis (see section 3.2.2).

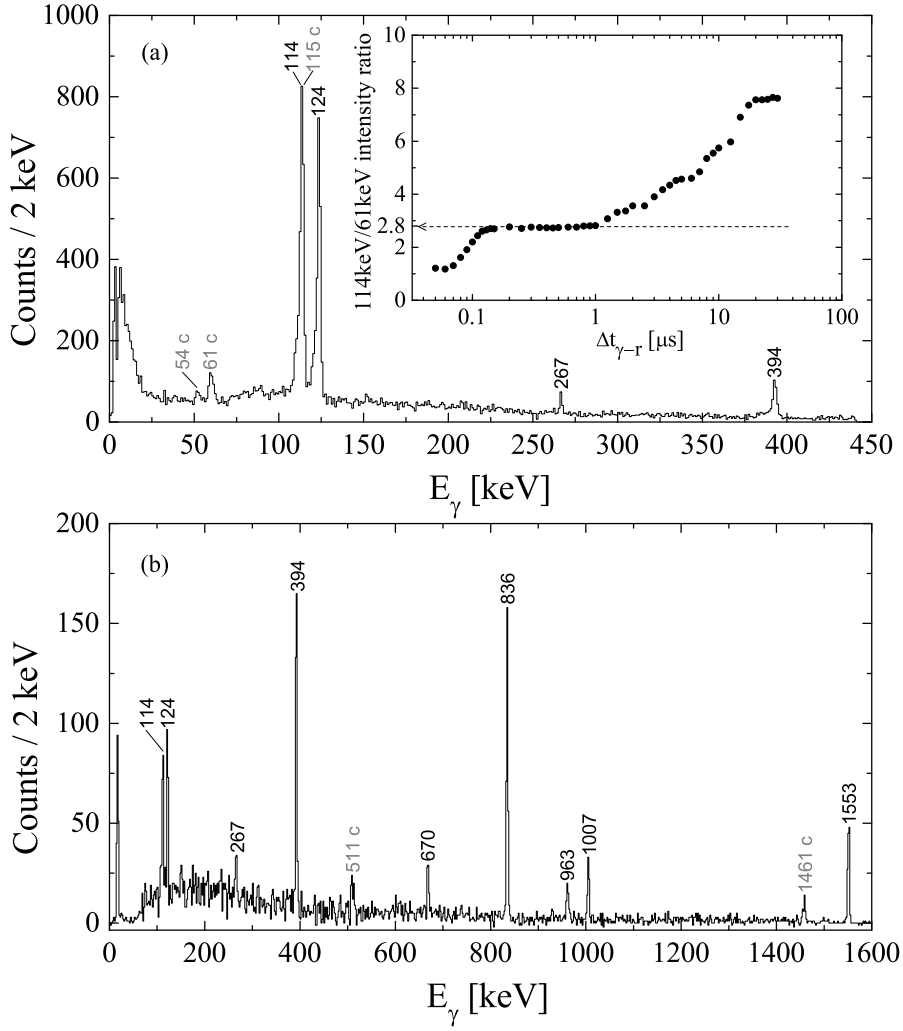

Figure 3.3: β-tagged delayed ^{66}As γ rays detected in the (a) planar and (b) clover germanium detectors. The low-energy threshold for the β particles was set to 1 MeV. Transitions with grey labels (and marked with a "c") in panel (a) are contaminants from the ^{65}Ga β decay feeding the excited states of ^{65}Zn. The time gate for γ-recoil time difference is 0−21 μs. Inset in panel (a): The intensity ratio of β-tagged 114- and 61-keV γ rays observed in the planar detector as a function of γ-recoil time difference. Information on the ^{65}Ga contamination in the ^{66}As 114-keV peak can be obtained from the flat part of the curve (see section 3.2.1 for details).

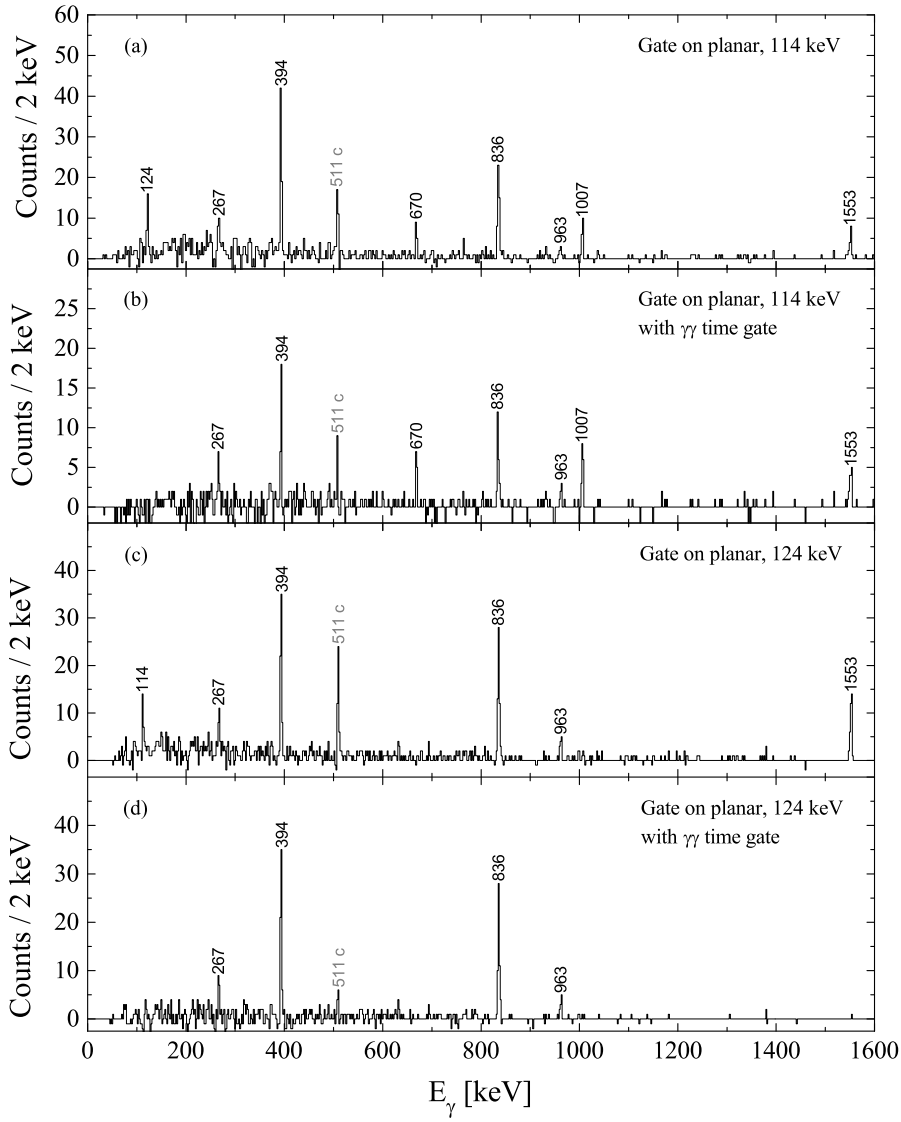

Figure 3.4: β-tagged and gated delayed γ-ray spectra from planar-clover matrices. In panels (a) and (b) the gate is set on the 114-keV transition detected in planar, whereas in panels (c) and (d) the gate is set on the 124-keV transition. In all panels the β gate was set to 0.5−10 MeV and γ_{planar}-recoil time gate to 0−21 μs. In panels (b) and (d), a narrow $\gamma\gamma$ time gate up to 100 ns is applied to identify only prompt γ-ray coincidences.

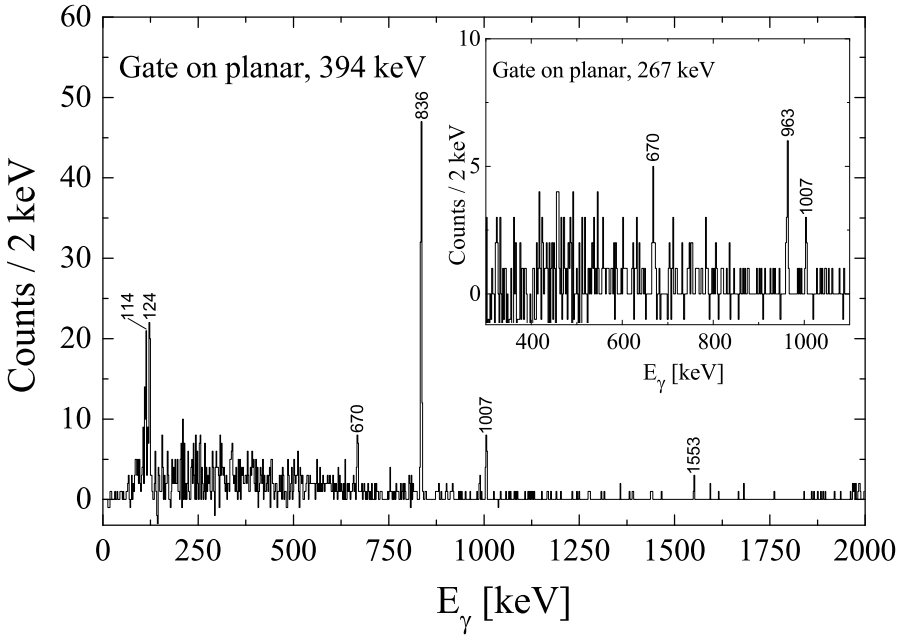

Figure 3.5: Recoil-gated delayed γ rays from the planar-clover matrix. The gate is set on the 394-keV transition detected in the planar, whereas in the inset the gate is set on the 267-keV transition. The time gate for γ_{planar}-recoil time difference is set to 0−21 μs in the main figure and to 0−5 μs in the inset in order to avoid random coincidences with contaminant γ rays. In addition, a narrow $\gamma\gamma$ time gate up to 100 ns is applied in both panels.

Table 3.1: The γ rays measured for ^{66}As at the focal plane of RITU. Intensities are relative to the $1_1^+ \rightarrow 0_1^+$ 836-keV transition.

E$_\gamma$ [keV]	I_{rel} [%]	E$_i$ [keV]	I_i^π	I_f^π	α_{tot}	t$_{1/2}$ [μs]
114.4(2)	54(4)	3021.4(6)	9_1^+	7_3^+	0.41(13)	7.9(3)
124.4(2)	84(2)	1354.3(5)	5_1^+	3_1^+	0.31(16)	1.15(4)
267.1(3)	17(5)	1229.9(4)	3_1^+	2_1^+		
393.6(3)	93(4)	1229.9(4)	3_1^+	1_1^+		
670.1(5)	27(3)	1899.9(5)	5_3^+	3_1^+		
836.3(4)	100(6)	836.3(4)	1_1^+	0_1^+		
963.1(5)	17(3)	963.0(4)	2_1^+	0_1^+		
1006.7(5)	26(3)	2907.0(5)	7_3^+	5_3^+		
1553.0(4)	51(4)	2907.0(5)	7_3^+	5_1^+		

Table 3.2: The prompt γ-ray transitions measured for ^{66}As. The energy of the γ rays (E_γ), relative γ-ray intensity (I_{rel}) normalized to 100 for the $2_1^+ \rightarrow 0_1^+$ transition, level energy (E_i), assigned spin and parity of the initial and final levels (I_i^π and I_f^π) and angular distribution information (A_2 and R) are listed.

E_γ [keV]	I_{rel} [%]	E_i [keV]	I_i^π	I_f^π	A_2	R
258.6(6)	15(1)	1600.3(9)	(5)	3_2^+	0.37(7)	1.56(13)[a]
266.7(7)	5(2)	1229.9(4)	3_1^+	2_1^+		0.69(18)[b]
290.0(12)	<10	2478.6(6)	5_4^+	(4_3^+)		0.40(18)[c]
354.6(5)	17(1)	2833.2(7)	7_2^+	5_4^+	0.23(11)	1.46(14)[a]
378.5(5)	31(2)	1341.7(6)	3_2^+	2_1^+	-0.39(9)	0.77(6)[a]
393.6(5)	28(1)	1229.9(4)	3_1^+	1_1^+	0.13(2)	1.22(9)[a]
506.0(11)	7(1)	1341.7(6)	3_2^+	1_1^+		
521.1(8)	12(1)	1751.0(9)	(4)	3_1^+		1.29(25)[d]
556.3(7)	19(1)	1519.3(8)	(4)	2_1^+	0.47(16)	1.15(10)[a]
669.7(6)	14(1)	1899.9(5)	5_3^+	3_1^+	0.59(20)	1.33(28)[b]
722.4(7)	15(4)	6530.4(11)	(14_1^+)	(12_1^+)		1.49(28)[b]
727.7(7)	17(4)	2478.6(6)	5_4^+	(4)		0.60(14)[b]
836.2(6)	42(3)	836.3(4)	1_1^+	0_1^+	-0.36(3)	0.70(12)[e]
839.6(13)	<10	3673.6(12)	(6_1^+)	7_2^+		0.60(21)[f]
840.9(5)	68(3)	3862.3(8)	11_1^+	9_1^+	0.30(5)	1.17(3)[g]
858.2(6)	11(3)	3691.4(10)	(9_3^+)	7_2^+		1.55(52)[h]
902.2(6)	12(3)	3251.0(11)	(9_2^+)	(7_1^+)		1.35(23)[i]
959.6(12)	24(8)	2478.6(6)	5_4^+	(4)		
962.8(5)	100(5)	963.0(4)	2_1^+	0_1^+	0.30(4)	1.27(15)[j]
994.5(7)	18(3)	2348.8(9)	(7_1^+)	5_1^+		1.38(29)[i]
1136.6(5)	22(4)	2478.6(6)	5_4^+	3_2^+	0.27(20)	1.25(12)[a]
1205.6(11)	18(2)	6530.4(11)	(14_1^+)	13_1^+		0.50(21)[k]
1226.0(11)	6(1)	2189.0(12)	(4_3^+)	2_1^+		1.64(58)[l]
1262.0(11)	7(1)	7792.4(16)	(16_1^+)	(14_1^+)		
1288.6(9)	8(3)	2518.5(10)	(4)	3_1^+		0.45(24)[d]
1462.3(6)	37(2)	5324.6(10)	13_1^+	11_1^+	0.51(7)	1.17(14)[g]
1486.0(16)	<3	3673.6(12)	(6_1^+)	(4_3^+)		
1553.0(11)	5(1)	2907.0(5)	7_3^+	5_1^+		
1946.0(11)	4(1)	5808.3(14)	(12_1^+)	11_1^+		

[a] Summed β-tagged rings
[b] Summed β-tagged rings with small β gate only
[c] Gate on 355 keV and 840 keV
[d] Gate on 394 keV and 836 keV
[e] Gate on 394 keV and 670 keV
[f] Gate on 290 keV and 355 keV
[g] Summed recoil-isomer-tagged rings
[h] Gate on 355 keV and 1137 keV
[i] Summed recoil-isomer and β-tagged rings
[j] Weighted average of gated (gate on 379 keV and 1137 keV) and summed β-tagged rings with 4.5−10-MeV β-gate
[k] Gate on 841 keV and 1462 keV
[l] Gate on 963 keV

Half-lives of the isomeric states

Half-lives of the isomeric states were determined by using the logarithmic binning method described by Schmidt *et al.* [71, 72]. This method is very convenient for discriminating between different radioactive species and is applicable especially in the cases where only limited statistics are available. In this method, the number of radioactive decay events are plotted against the natural logarithm of the time differences giving rise to a bell-shaped distribution. The half-life can be extracted from the centroid of this distribution. The two-component function fitted to the half-life data is of the form

$$\left|\frac{dn}{d\Theta}\right| = (n_1\lambda_1 e^{-\lambda_1 e^{\Theta}} + n_2\lambda_2 e^{-\lambda_2 e^{\Theta}})e^{\Theta}, \tag{3.4}$$

where a substitution $\Theta = \ln(\Delta t)$ is introduced, n_i and λ_i, where $i = \{1, 2\}$ are the number of counts and decay constants of two different activities, respectively. Figure 3.6 presents the half-life data and the fitted two-component functions under various gating conditions. The black and red data points correspond to recoil-correlated and β-tagged delayed γ-ray data, respectively. The solid curves represent fits of Eq. (3.4) to the data. Recoil-gated data provide the desired statistics for reliable half-life determinations, but in order to verify the accuracy of the results, the β tagging was also employed. The larger distributions in the time spectra presented in Figs. 3.6(a) and 3.6(b) correspond to real activities caused by the decay of the isomeric states, whereas the smaller components are due to random background. In the case of the higher-lying isomeric state, the half-life can be extracted from γ-recoil time differences gating with the 1553-keV γ rays detected in the clover detector. Other γ rays such as the 1007- and 670-keV transitions below the higher-lying isomeric state could have been used. However, this causes the random component to become the dominant part of the distribution due to the increased background at lower energies. Using a single γ-ray energy gate to extract γ-recoil time differences for the lower-lying isomeric state does not work due to feeding of the higher-lying isomer. To overcome this issue, the time difference of two or more γ rays detected in the planar and clover detectors can be resolved. The time-difference spectrum presented in Fig. 3.6(b) shows the time difference between the 114- or 1553-keV transition recorded in the clover and the 124-keV transition observed in the planar. This method provides a low background time distribution in both recoil-correlated and β-tagged cases to accurately determine the half-life of the lower-lying isomeric state. A very clean time distribution can be obtained using the β-tagging condition without any random background events for the lower-lying isomeric state by excluding the detection of the 114-keV γ ray in the clover from the gating conditions. The time distribution obtained in this way is shown in Fig. 3.6(b) as a grey histogram and the half-life was derived from the data by using the maximum likelihood method [71].

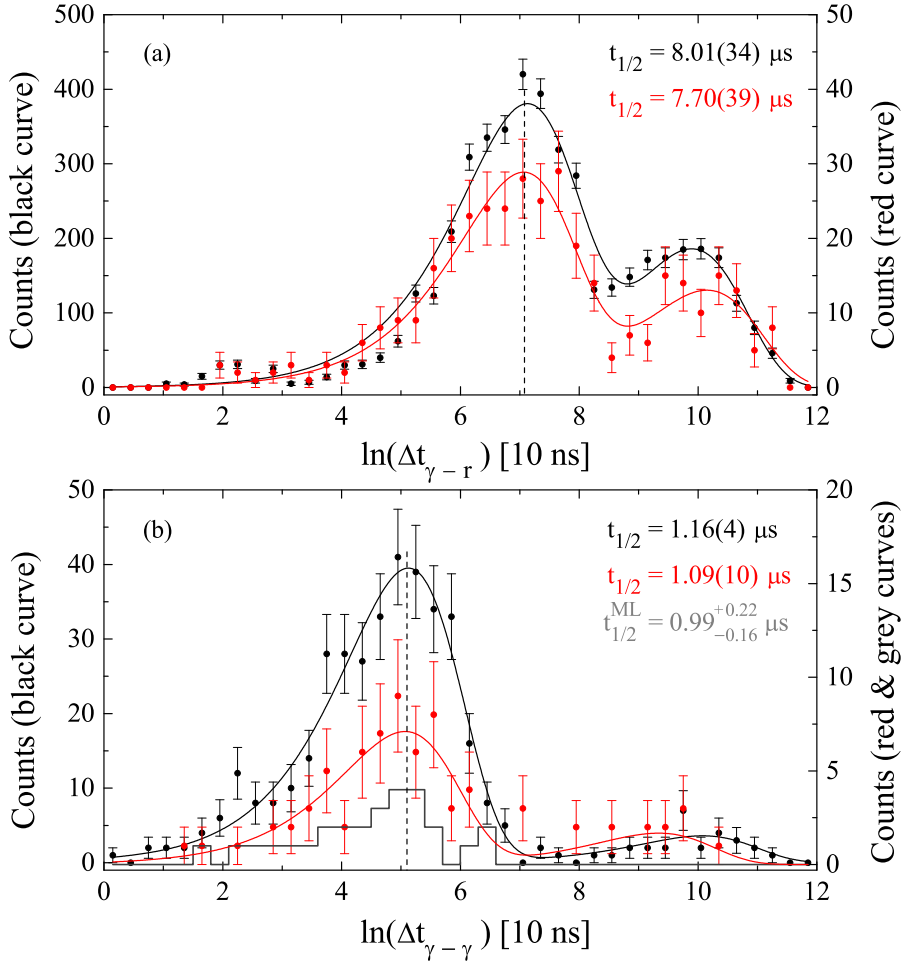

Figure 3.6: Half-life data and fits used to extract the half-lives of the (a) 3021-keV and (b) 1354-keV isomeric states, respectively. The dashed line indicates the centroid of the time distribution, which corresponds to the half-life of the isomeric state and fitted λ_1 parameter in Eq. 3.4. The smaller distributions at higher $\ln(\Delta t)$ values are due to the random background and corresponds to the fitted λ_2 parameter in Eq. 3.4. Details of the time spectra and determination of the half-lives are explained in the text.

Half-lives for the ^{66}As isomeric states can be extracted from the fitted λ_1 parameter which yields $t_{1/2} = 8.01(34)$ μs from the recoil-correlated data and $t_{1/2} = 7.70(39)$ μs from the β-tagged data for the higher-lying isomeric state. Corresponding values for the lower-lying isomeric state are $t_{1/2} = 1.16(4)$ μs from the recoil-correlated and $t_{1/2} = 1.09(10)$ μs from the β-tagged data. Applying the maximum likelihood method to the data, presented in Fig. 3.6(b) as a grey histogram, produces a value of $t_{1/2} = 0.99^{+0.22}_{-0.16}$ μs for the lower-lying state. The values obtained from differently conditioned data are consistent within error limits and can be considered to give accurate values for the isomeric half-lives. To combine the final values for the half-lives, a weighted average was calculated for each isomer, yielding $t_{1/2} = 7.9(3)$ μs and $t_{1/2} = 1.15(4)$ μs for the higher- and lower-lying isomeric states, respectively. These values are somewhat smaller than the ones reported in [69]. In Ref. [69] the half-life determination was performed by fitting a single-component exponential function to the decay data in the case of the higher-lying isomeric state. This yields a significantly inconsistent result of $t_{1/2} = 17.5(15)$ μs compared to the value presented in the current study. Such a substantially longer value of the half-life may result from the fact that the decay data visualised in the regular linear form contained a longer-lived background or another component, which inevitably causes the fitted single-component function to overestimate the half-life of the state. In Ref. [73] the half-lives are reported to be $t_{1/2} = 8.2(5)$ μs and $t_{1/2} = 1.1(1)$ μs for the higher- and lower-lying isomeric states, respectively. These values and the ones obtained from the present study are in agreement within error limits.

In the present study data were also produced for the ^{69}Ge and ^{65}Zn nuclei, which both contain long-lived states. Previously reported half-lives for the $9/2^+$ state at 398 keV in ^{69}Ge are 2.79(6) μs, 2.84(7) μs and 3.2(6) μs [74]. The ones for the $(1/2)^-$ state at 54 keV in ^{65}Zn are 1.52(9) μs and 1.65(5) μs [75]. The recorded delayed γ rays originating from ^{69}Ge and ^{65}Zn provide a perfect test for the validity of the half-life determination method described above. Similar analysis as carried out for the ^{66}As yields half-life values of 2.70(8) μs for the $9/2^+$ state in ^{69}Ge and 1.51(7) μs for the $(1/2)^-$ state in ^{65}Zn. These values are in agreement within error limits with the weighted averages of the previously reported values [2.81(5) μs for ^{69}Ge and 1.62(6) μs for ^{65}Zn].

Internal conversion coefficients of transitions from isomeric states

The total internal conversion coefficients can be determined for the two transitions de-exciting the isomeric states by demanding the preservation of the transition intensity through a cascade. Experimentally obtained values can then be compared to the theoretical total internal conversion coefficients obtained from Ref. [76] to see which transition types are possible. To evaluate the intensity balance, detailed information on the detector efficiencies is crucial. As was discussed earlier, efficiency curves for the planar and the clover germanium

detectors were simulated with a GEANT4 toolkit [47, 48] according to the experimental circumstances (see section 2.2.4). The distribution of implanted recoils in the DSSD and the thickness of the implantation detector were taken into account in these simulations. As RITU is designed to operate in heavier mass region, the separation of fusion residues from the primary beam and other unwanted products is challenging in the mass $A \approx 70$ region. For this reason, the optimal settings for RITU could not be used, which caused the recoil distribution to be focused more on the right-hand side of the DSSDs. Clearly, if the recoil distribution is not uniform across the DSSD, the γ-ray detection efficiencies of the planar and clover detectors placed around the DSSD will be affected by this geometrical deviation. Therefore the previous simulations by Andreyev *et. al.,* [77] could not be used.

The total intensity of the 114-keV transition feeding a state, which is depopulated by the 1007- and 1553-keV transitions, has to equal the sum of the intensities of the latter mentioned transitions. The internal conversion of the 1007- and 1553-keV transitions is negligible due to the high energies, so there is no need to make assumptions about the transition characteristics nor correct the experimental intensities for conversion. The efficiency-corrected intensity of the β-tagged 114-keV γ-ray transition observed in the planar is thus compared to the sum of the efficiency-corrected intensities of the β-tagged 1007- and 1553-keV γ rays detected in the clover in order to resolve the total internal conversion coefficient for the 114-keV transition. Despite the β-tagging conditions, there is always a certain amount of contaminant events in the 114-keV planar peak originating from random correlations of the ^{65}Ga β decay to the excited states in ^{65}Zn, where one of the states is depopulated by a 115-keV γ-ray transition. Fortunately, the magnitude of contamination can be estimated and corrected for, as there is also a 61-keV γ-ray transition depopulating the same state as the 115-keV transition in ^{65}Zn. The intensity ratio of these transitions can be resolved as a function of γ-recoil time differences in order to obtain a correction factor for the 114-keV γ-ray intensity. This is shown in Fig. 3.3(a) as an inset. At time differences between 0.1−1 μs, the intensity ratio of the 114- and 61-keV peaks remains at a constant value, as it should before the ratio starts to increase monotonically due to the decay of the higher-lying isomeric state in ^{66}As, which increases the intensity of the 114-keV peak rapidly. The correction factor 2.8 can be obtained from the plateau in the curve, which is then used to subtract the intensity corresponding to the contamination ($2.8 \times I_{61\ \mathrm{keV}}$) from the total intensity of the 114-keV peak. After this correction, the total internal conversion coefficient can be determined, yielding the value of $\alpha_{\mathrm{exp}} = 0.41(13)$ for the 114-keV transition in ^{66}As. The closest total internal conversion coefficients for this transition energy obtained from Ref. [76] are $\alpha_{\mathrm{th}}^{\mathrm{E2}} = 0.48(1)$ and $\alpha_{\mathrm{th}}^{\mathrm{M2}} = 0.59(1)$, hence suggesting the transition has an $E2$ character. The error of the theoretical value originates from the uncertainty in the energy measurement of the 114-keV γ ray.

The total intensity of the 124-keV transition has to equal the sum of the 267- and 394-keV transition intensities as they feed and de-excite the same state. The problem is that this state is also fed from the higher-lying isomer via the 1007- and 670-keV transitions. As there is a large difference between the isomeric half-lives, setting a strict 0−1-μs time gate on the γ-recoil time difference, the additional feeding from above can be eliminated. The validity of the time gate can be verified from the plot presented in the inset of Fig. 3.3(a). Theoretical total internal conversion coefficients for the 267- and 394-keV transitions are practically negligible for any of the multipolarities below $\lambda = 4$. Therefore, no assumptions on their character are needed nor corrections to the intensity for conversion. The efficiency-corrected intensity of the β-tagged 124-keV transition detected in the planar is thus compared to the sum of the efficiency-corrected intensities of the β-tagged 267- and 394-keV transitions detected also in the planar giving rise to the total internal conversion coefficient of $\alpha_{\mathrm{exp}} = 0.31(16)$. Relevant coefficients obtained from Ref. [76] are $\alpha_{\mathrm{th}}^{\mathrm{E2}} = 0.35(1)$ and $\alpha_{\mathrm{th}}^{\mathrm{M2}} = 0.43(1)$, confirming the 124-keV transition multipolarity to be $\lambda = 2$ and suggesting an electric character.

The experimental conversion coefficients reported in Ref. [69] are 1.3(4) for the 114-keV transition and 0.7(3) for the 124-keV transition. The discrepancies probably result from the underestimation of the γ-ray intensities in Ref. [69] due to a large Compton background.

3.2.2 Short-lived states in ^{66}As

The prompt γ rays measured with JUROGAM II originating from ^{66}As can be observed already with a large 1−10-MeV β gate as illustrated in Fig. 3.7(a). This is essential when statistics are needed for the $\gamma\gamma$ analysis and angular distributions. However, the spectrum tagged with majority of detected β particles suffers from heavy contamination caused by stronger reaction channels such as ^{66}Ge and ^{65}Ga. By raising the β-particle detection threshold by 2 MeV and adding a background subtraction condition, allows for clean identification of ^{66}As γ rays as illustrated in Fig 3.7(b). The background subtraction condition is based on the events in the planar with energies between 10−14 MeV and on the constant fraction of background within the main β gate (the value used in the GRAIN matrix slicer was ∼0.001). The background subtraction condition can be best illustrated with a $E_\gamma - E_\beta$ matrix shown in Fig. 3.8. Here, the intensities of the γ-ray lines from ^{66}As die off near the upper limit of the main β gate (blue rectangle), which corresponds to the ∼10-MeV β-end-point energy of ^{66}As. However, as ^{65}Ga has been falsely correlated, the contribution of the ^{65}Ga γ-ray lines is visible throughout the detected β distribution and especially in the region between $E_\beta = 10-14$ MeV. Therefore, the background subtraction gate was placed in this region to reduce the ^{65}Ga contamination.

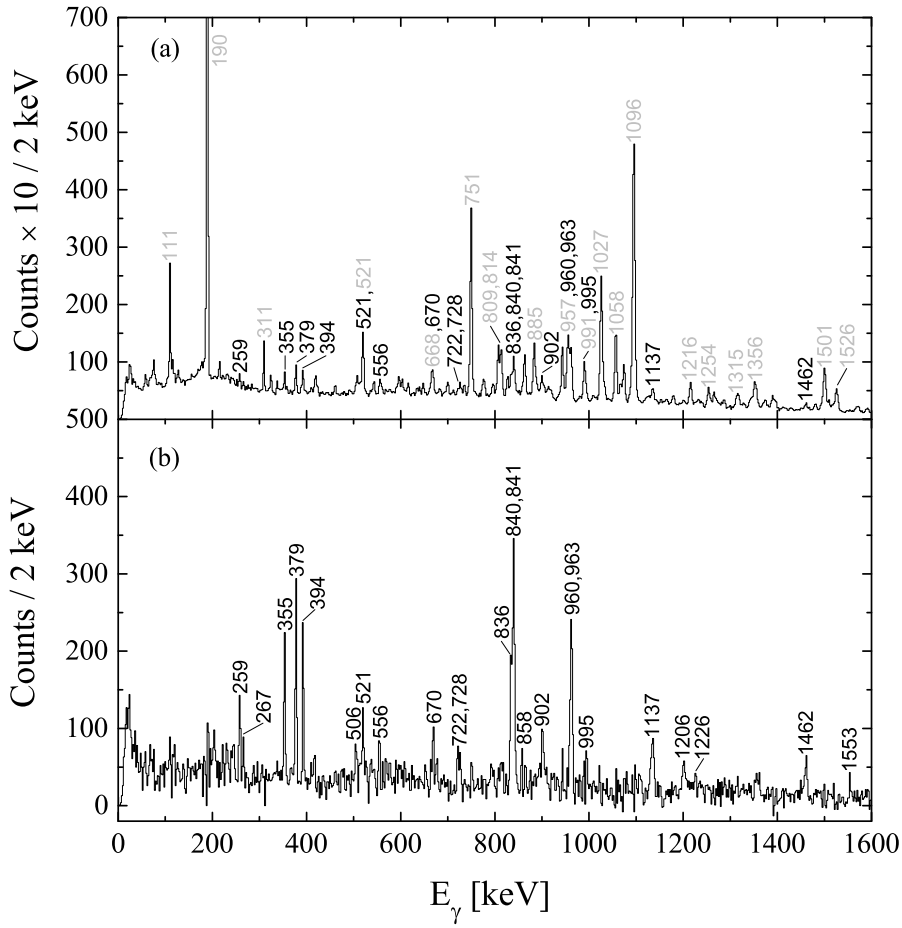

Figure 3.7: Recoil-β tagged JUROGAM II singles spectra using a 300-ms correlation time with (a) 1−10-MeV β gate and (b) 3−10-MeV β gate. In panel (b) a background subtraction condition is employed to reduce falsely correlated γ rays. Peaks labeled in black are transitions associated with ^{66}As, while grey labels are for transitions originating from other reaction channels such as ^{66}Ge, ^{65}Ge, ^{65}Ga and ^{64}Zn.

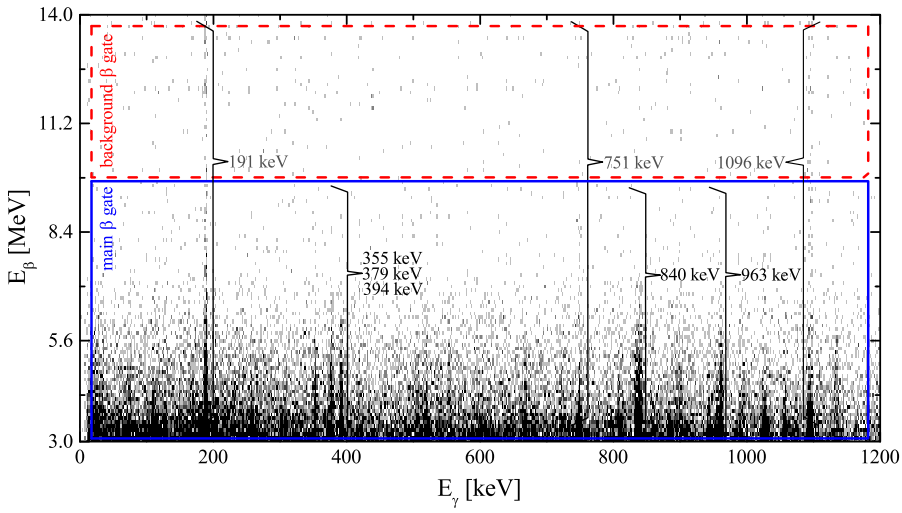

Figure 3.8: The energy of a tagged prompt γ ray in JUROGAM II (x axis) vs β-particle energy in the planar detector (y axis) to illustrate the background subtraction condition employed in Fig. 3.7(b). The events between $E_\beta = 10-14$ MeV contain only falsely tagged ^{65}Ga γ rays. See text for details.

From the β-tagged singles spectrum shown in Fig. 3.7(b), five prominent peaks located at energies of 355 keV, 379 keV, 394 keV, 836−841 keV and 960−963 keV can be observed. These transitions have to originate from levels rather close to the ground state of ^{66}As because one would expect a rapid increase in the level density, hence strong fragmentation of the γ-ray transition intensity, when going to higher excitation energy. The prominent peaks listed represent decays from both the $T = 0$ and the $T = 1$ states in ^{66}As. In the following discussion the results concerning the prompt γ-ray transitions are presented. The experimentally observed excited states in ^{66}As have been divided into isospin $T = 1$ and $T = 0$ structures. The illustrated $\gamma\gamma$ coincidence spectra represent cases where rather strict β gates (∼3−10 MeV) have been used in order to show the cleanest coincidences. This excludes some of the "good" events, which are more pronounced with relaxed gating conditions along with the contaminant γ-ray transitions. Coincidence spectra illustrated in Figs. 3.9(a) and 3.9(b) represent the effect of the size of the β gate on the observed coincidences. In panel (b), the low-energy threshold is raised by 1.5 MeV, which produces a clean and low-background spectrum, but the coincidence with the 1137-keV transition seems to be missing although it can be clearly identified in panel (a). In the other spectra shown in Figs. 3.10 and 3.11, all the transitions, which have been found to coincide with the gating transition with relaxed tagging conditions are labeled even if they do not clearly stand out from the background in these particular figures.

$T = 1$ states

The ground state of ^{66}As is expected to be $T = 1$, $I^\pi = 0^+$ [78, 69, 73, 70], which is known to β decay to the $T = 1$, $I^\pi = 0^+$ ground state of ^{66}Ge via a Fermi superallowed transition [59, 62, 60, 61]. Taking into account the isospin symmetry between isobaric multiplets, the closest transition in ^{66}As, energy-wise, to the ^{66}Ge, $2_1^+ \rightarrow 0_1^+$ 957-keV transition is the 963-keV transition [79]. The angular distribution information [$A_2 = 0.30(4)$] and the value of the angular distribution ratio [$R = 1.27(15)$] obtained for the 963-keV peak suggests a stretched $E2$ character. Thus, on the basis of intensity and energy arguments, the 963-keV transition is assigned as the $2_1^+ \rightarrow 0_1^+$ transition in ^{66}As. Analysis of the $\gamma\gamma$ coincidences, with a gate set on the 963-keV transition and simultaneously varying the size of the β gate, reveals a peak located at 1226 keV (see Fig. 3.9). When the gate is set on the 1226-keV transition, the most intense coincidence is seen with the 963-keV transition (see inset in Fig. 3.9(a)). Thus, these two transitions can be concluded to form a cascade. The energy of the $4_1^+ \rightarrow 2_1^+$ transition found in ^{66}Ge is 1216 keV, which is rather close to 1226 keV. These arguments along with the deduced angular distribution ratio of $R = 1.64(58)$ for the 1226-keV transition suggests that it is the second transition in the ^{66}As $T = 1$ band de-exciting a 4_3^+ state at 2189 keV in agreement with Ref. [70]. Further investigation of the coincidence events gated by the 1226-keV transition reveals a γ-ray peak at an energy of 1486 keV. This transition stands out from the background with a rather large β gate of the order of 2−10 MeV and it can be distinguished as a separate peak from the ^{66}Ge, $6_1^+ \rightarrow 4_1^+$ 1481-keV transition. The 1486-keV transition is tentatively assigned to de-excite the $T = 1$, 6_1^+ state at 3674 keV, because of the similarity with the corresponding transition found in ^{66}Ge and observed coincidence relations. Coincident events with the 963- and 1226-keV lines are illustrated in Fig. 3.9(c), where the low-background region containing the candidates for the $4_3^+ \rightarrow 2_1^+$ and $6_1^+ \rightarrow 4_3^+$ transitions is shown in the inset. The peak at 1272 keV is a contaminant from ^{64}Zn. Further proof for the existence of the level at 3674 keV can be obtained from the other observed coincidences as will be discussed in section 3.2.2. The candidate for the 6^+ state reported in Ref. [70] is 37 keV lower than the corresponding state identified in the present study.

$T = 0$ states

The 836-keV transition seen in both delayed and prompt spectra is assigned to de-excite the lowest $T = 0$, 1_1^+ level. This fact is supported by the observed high intensity of prompt γ rays and the conclusions made from the delayed coincidence data. Furthermore, both the extracted angular distribution coefficient [$A_2 = -0.36(3)$] and the value of angular distribution ratio [$R = 0.70(12)$] are indicative of a stretched $\Delta I = 1$, $M1$ transition. The prompt coincidences

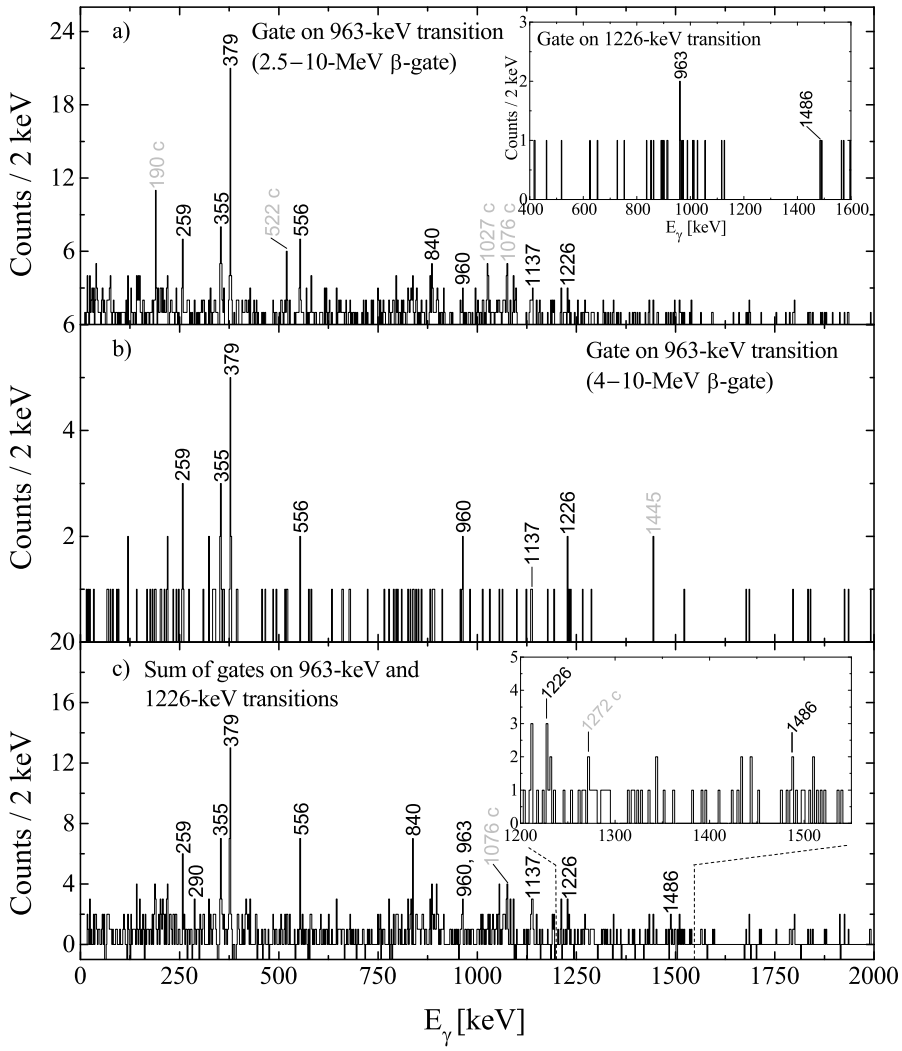

Figure 3.9: β-tagged and gated JUROGAM II spectra showing coincidences within the $T = 1$ band and between $T = 0$ and $T = 1$ bands. In (a) and (b) the gate is set on the 963-keV transition with β gates of 2.5−10 MeV and 4−10 MeV, respectively, to illustrate the effect of the size of the β gate on the gated spectra. The inset in (a) shows the coincidences with the 1226-keV transition with 3−10-MeV β gate. In (c) the gates are set on the 963- and 1226-keV transitions with a 2.5−10-MeV β gate. The inset in (c) shows the low-background region where the 1226- and 1486-keV lines are identified. In each panel background subtraction is employed by setting a background gate with the same width as the main gate, near the gating transition. Peaks labeled in grey and marked with a "c" are contaminants from ^{66}Ge, ^{65}Ga and ^{64}Zn.

seen with a gate on the 836-keV transition are shown in Fig. 3.10(a). The most intense coincidences, when the β gate is relaxed slightly, occur with the 394- and 670-keV transitions. Both of these transitions were also seen in the delayed spectra; thus, it can be assumed that these three transitions form a $T = 0$ cascade (Band 3). Angular distribution information obtained for the 394- and 670-keV lines suggests that they are both stretched $\Delta I = 2$, $E2$ transitions. Taking into account the γ-ray intensities deduced from the delayed data (see Table 3.1), the 394- and 670-keV transitions are assigned to de-excite a 3_1^+ state at 1230 keV and a 5_3^+ state at 1900 keV, respectively. It was confirmed earlier that the isomeric 124-keV γ-ray transition, with experimental conversion coefficient corresponding to an $E2$ character, is feeding the state at 1230 keV. Therefore, the isomeric state at 1354 keV is assigned as 5_1^+. The non-observation of the 1007-keV transition, which clearly belongs to the same $T = 0$ cascade with the 836-, 394- and 670-keV transitions, in the prompt data might be due to the non-yrast nature of the level at 2907 keV added to the favoured branching of the 1553-keV transition, which de-excites the same state. Remembering the experimental conversion coefficient, which suggests $E2$ character for the isomeric 114-keV γ-ray transition feeding the state at 2907 keV, the states at 2907 keV and 3021 keV can be assigned as 7_3^+ and 9_1^+, respectively.

The most intense coincidence with the 963-keV transition appears to be the 379-keV line, as illustrated in Fig. 3.9; hence, the 379-keV transition is concluded to feed the 2_1^+ state at 963 keV from another $T = 0$ sequence. The angular distribution coefficient [$A_2 = -0.39(9)$] and the angular distribution ratio [$R = 0.77(6)$] obtained for the 379-keV transition strongly imply a stretched $\Delta I = 1$, $M1$ character for this γ ray; therefore, a spin assignment of 3_2^+ is made for the $T = 0$ level at 1342 keV. The 379- and 355-keV transitions are seen in strong mutual coincidence. The 355-keV line is seen also in coincidence with the 728-, 521- and 394-keV mutually coinciding transitions, which in turn are seen from below by the $1_1^+ \rightarrow 0_1^+$ 836-keV transition. This supports the fact that the 1137-keV transition lies between the 355- and 379-keV transitions. Both of these γ-ray transitions naturally see the 1137-keV line, as can be noted from Figs. 3.11(a) and 3.11(b). The 379-, 1137- and 355-keV transitions are concluded to belong to the same $T = 0$ band (Band 2). The angular distribution coefficients and ratios suggest an $E2$ character for both the 1137- and the 355-keV transitions. Therefore, spin assignments of 5_4^+ and 7_2^+ are made for the $T = 0$ levels at 2479 keV and 2833 keV, respectively. It should be noted that the γ-ray energies of the parallel branches consisting of the transitions of 963 keV, 379 keV and 1137 keV and 836 keV, 394 keV, 521 keV and 728 keV add to the same sum energy of 2479 keV. The angular distribution ratio obtained for the 728-keV transition partially de-exciting the 5_4^+ level at 2479 keV has a value expected from an $M1$ character, whereas the R value of the subsequent 521-keV transition is consistent with a mixed $M1/E2$ transition. Based on these numbers, the level at 1751 keV is tentatively assigned as $I = 4$.

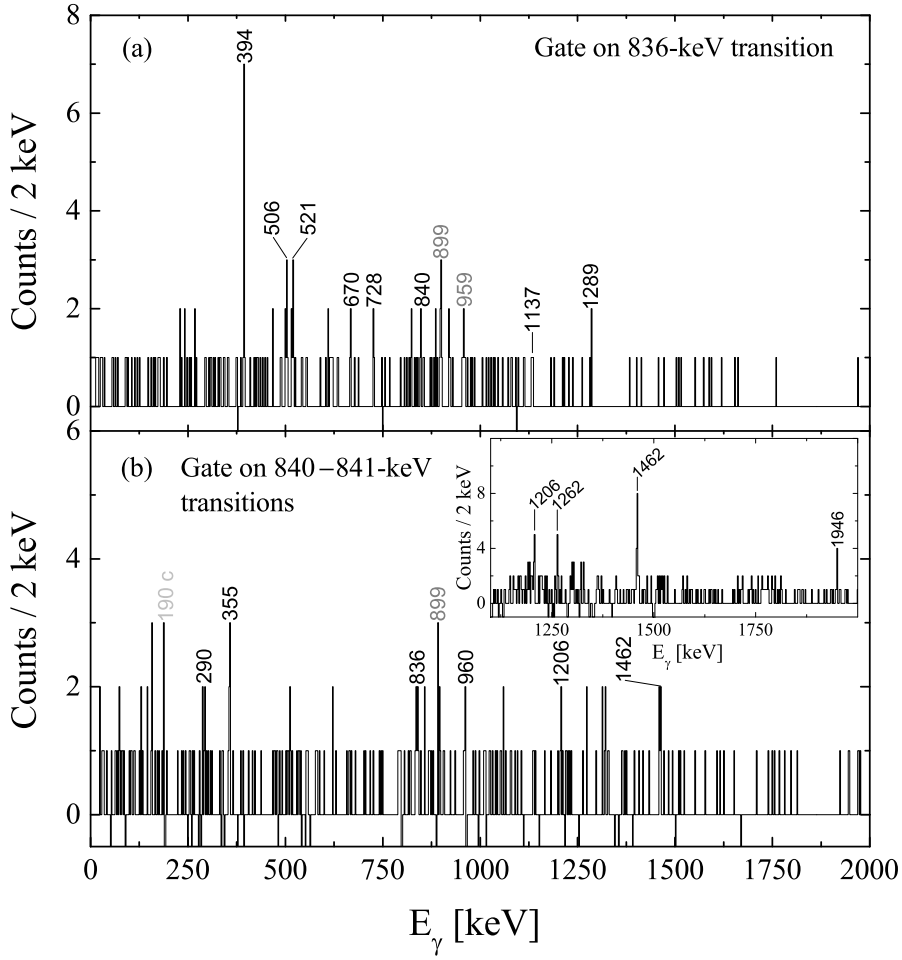

Figure 3.10: β-tagged and gated prompt JUROGAM II coincidence spectra. In panel (a) the gate is set on the 836-keV transition with 2.75−10-MeV β gate. In panel (b) the gate is set on the 840−841-keV transitions with 3.25−10-MeV β gate. The inset in panel (b) illustrates a part of the coincidence spectrum gated by the 840−841-keV transitions with 1.5−10-MeV β gate. Peaks labeled in dark grey are unidentified transitions while the one labeled in grey and marked with a "c" is a contaminant from ^{65}Ga.

The 556-keV transition is seen in coincidence with the 355- and 963-keV transitions, where the coincidence with the latter γ ray seems to be more intense. For this reason the 556-keV transition is assigned to feed the 2_1^+ state at 963 keV from a $T = 0$ state located at 1519 keV. Observed coincidences illustrated in Figs. 3.9(a) and 3.9(b) and in Fig. 3.11(a) all show a peak at 960 keV, which corresponds exactly to the energy difference between the 2479- and 1519-keV levels. The angular distribution coefficient and ratio suggest $E2$ character for the 556-keV transition, which implies that the state at 1519 keV is 4_1^+. This would lead to the fact that the 960-keV transition from the 2479-keV, 5_4^+ state to the 1519-keV, 4_1^+ state should be $M1$ type. Unfortunately, it was not possible to extract the R value with small-enough uncertainty to fix the multipolarity of the 960-keV transition. Therefore, the level at 1519 keV is only tentatively assigned as $I = 4$.

The ($T = 1$, 6^+) state at 3674 keV

One of the most prominent peaks shown in Fig. 3.7(b), located at 836−841 keV, is a triplet. As mentioned earlier, the 836-keV line originates from the decay of the 1_1^+ state in Band 3 and the formerly known 841-keV transition feeds the isomeric 9_1^+ state in Band 4 [73]. Inspecting the coincidences shown in Figs. 3.9(a), 3.9(c) and in Fig. 3.11(a), a line at 840 keV can be observed in each spectra, which cannot be associated with either of the two previously mentioned γ rays. Moreover, the 840-keV line is found to coincide with the 355-, 290- and 960-keV lines as shown in Fig. 3.10(b). After fixing most of the levels within the $T = 1$ and different $T = 0$ bands, the 840-keV transition fits within error limits between the $T = 0$, 7_2^+ and tentative $T = 1$, 6_1^+ levels located at 2833 keV and 3674 keV, respectively, and satisfies the observed coincidences. The angular distribution ratio $R = 0.60(21)$, which is consistent with a stretched $M1$ transition, is derived for the 840-keV line as it can be separated from the other members of the triplet by clean $\gamma\gamma$ coincidence relations.

Recoil-isomer tagging

The recoil-isomer tagging method [32, 33] was employed both alone and in conjunction with the β-tagging method. Prompt structures above the isomeric 9_1^+ state, previously reported in Ref. [73], were also observed in the present study and the ordering confirmed on the basis of $\gamma\gamma$ analysis. The 841-keV transition is clearly the most intense as can be noted from Fig. 3.12(a). Therefore, it is assigned to feed the isomeric 9_1^+ state at 3021 keV. Both the angular distribution coefficient [$A_2 = 0.30(5)$] and ratio [$R = 1.17(3)$] deduced for the 841-keV transition are typical for an $E2$ transition. This leads to a spin assignment of 11_1^+ for the level at 3862 keV. A second intense transition in Fig. 3.12(a) is

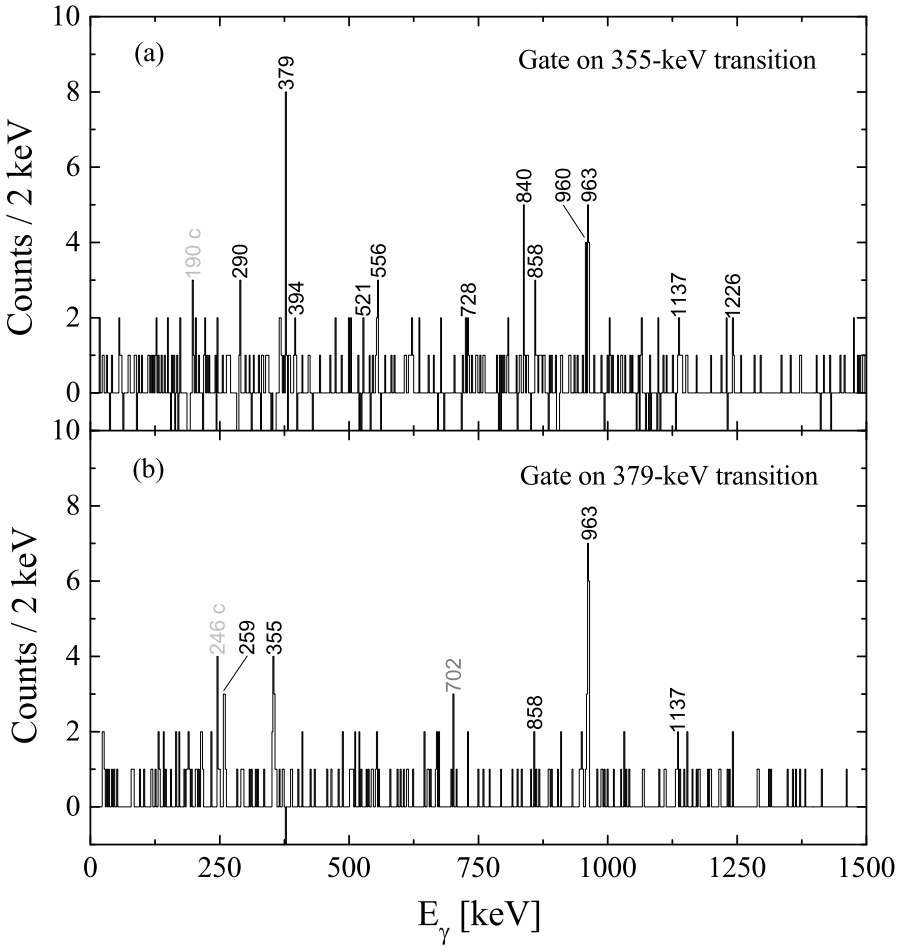

Figure 3.11: β-tagged and gated prompt JUROGAM II spectra with gate on the (a) 355-keV and (b) 379-keV γ-ray transitions. The size of the β gate is 3.25−10 MeV in the both panels. Peaks labeled in grey and marked with a "c" are contaminants from ^{65}Ga and ^{62}Ga while the one labeled in dark grey is an unidentified transition.

the 1462-keV line with an angular distribution value indicating an $E2$ character. A strong mutual coincidence observed between the 841- and 1462-keV lines suggests that the latter transition feeds the 11_1^+ state and depopulates a 13_1^+ level at 5325 keV; hence, they belong to the same $T = 0$ band. The 1206-keV transition is observed in coincidence with both of the previously mentioned lines and the extracted angular distribution ratio implies $M1$ character. The 1206-keV transition is therefore assigned tentatively to depopulate a 14_1^+ state at 6530 keV in good agreement with Ref. [73]. The 722-keV transition [$R = 1.49(28)$] is observed to be in coincidence with the 841-keV line and simultaneously with the 1946- and 1262-keV transitions, but not with the relatively strong 1206- and 1462-keV transitions. The 722-keV transition is tentatively assigned to de-excite the 14_1^+ state at 6530 keV and to feed a 12_1^+ state at 5808 keV, which in turn is de-excited by the 1946-keV transition.

Peaks labeled in grey in Figs. 3.12(a) and 3.12(b) are γ-ray transitions, which could not be associated with any of the competing reaction products or linked with the other observed ^{66}As γ-ray transitions. The 894-, 909- and 1133-keV transitions were also reported in Ref. [73], but the authors were unable to place them in the level scheme.

Figure 3.12(b) shows a β- and isomer-tagged JUROGAM II singles spectrum with 0−3-μs γ-recoil time gate suitable for the lower-lying 5_1^+ isomeric state. Three intense peaks at 841 keV, 902 keV and 995 keV are observed. The latter two were confirmed to be in mutual coincidence, but could not be connected to any other prompt γ-ray transitions found in ^{66}As. The 902- and 995-keV transitions were investigated with very strict β and time gates and can be unambiguously associated with ^{66}As. As the 995-keV transition is found to be slightly more intense than the 902-keV transition, the 995-keV line is assigned to feed directly to the isomeric 5_1^+ state. The angular distribution ratios obtained both for the 902- and 995-keV lines, favour $E2$ type of transitions; thus, the levels at 2349 keV and 3251 keV are tentatively assigned as 7_1^+ and 9_2^+, respectively. There seems to be a small peak at 835 keV right next to the 841-keV peak as illustrated in Fig. 3.12(b). In addition, there are some events detected around 1486 keV, which are visible in both panels of Fig. 3.12. One could speculate that a 835-keV $M1$ transition from a $T = 1$, 4_3^+ state could directly feed the isomeric 5_1^+ state. However, this scenario could not be confirmed unambiguously during the data analysis; hence, it will be left as an open question.

3.3 Discussion

The structure of ^{66}As has been studied theoretically by Hasegawa *et al.*, [78] and Honma *et al.*, [12]. Both of these studies were based on shell-model calculations

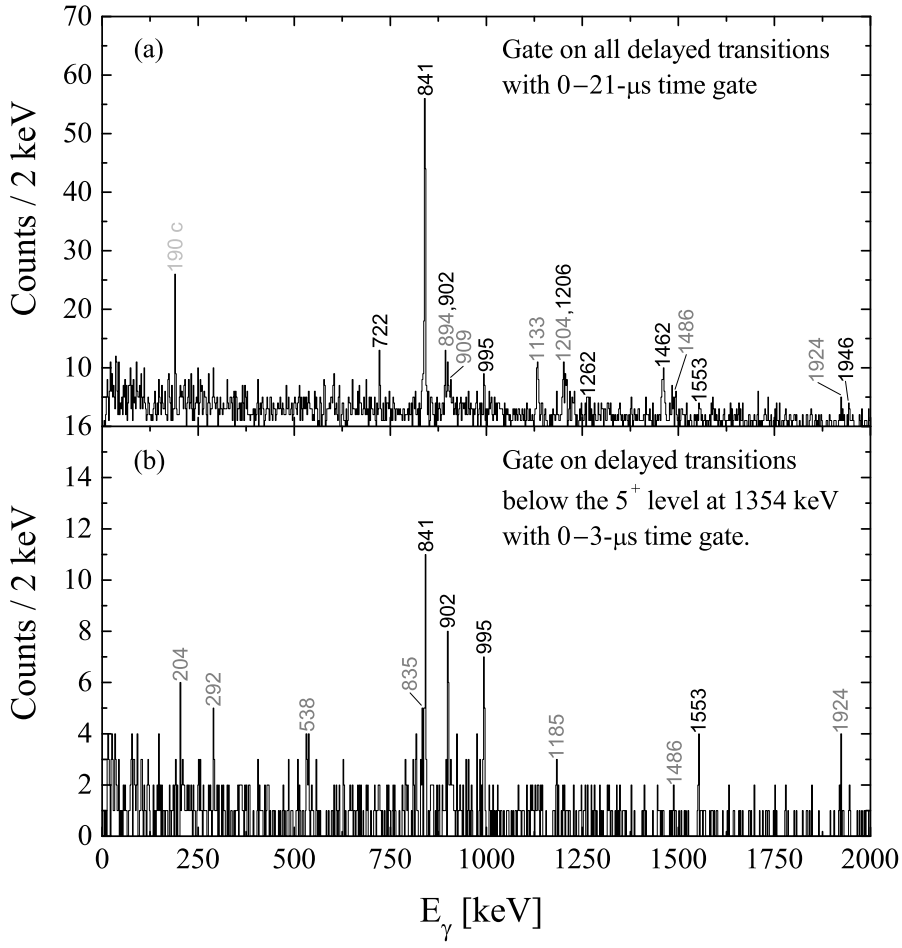

Figure 3.12: Recoil-isomer and β-tagged JUROGAM II singles spectra. In panel (a) all delayed γ-ray transitions associated with ^{66}As are used as a tag with the β-energy gate of 1.5−10 MeV. In panel (b) only the delayed γ-ray transitions originating from states below the lower-lying isomeric 5_1^+ state in ^{66}As are used as a tag along with a β gate of 1.5−10 MeV. Peaks labeled in dark grey are unidentified transitions while the peak labeled in gray and marked with a "c" is a contaminant from ^{65}Ga.

using the $p_{3/2}$, $f_{5/2}$, $p_{1/2}$ and $g_{9/2}$ single-particle orbits as a model space. Differences between these studies arise from the interaction used and the single-particle energies. Identical calculations as applied in Ref. [12] using the modern effective JUN45 interaction have been employed in the present work to compare with the experimental data. These calculations were extended beyond the isomeric structures to include properties of all states and $E2/M1$ transition strengths. The predicted level energies are illustrated in Fig. 3.13.

3.3.1 Isomeric states and $E2$ transition strengths

Studies presented in Refs. [78] and [12] both suggest that the structure of the experimentally observed isomeric 9^+_1 and 5^+_1 states can be interpreted as fully aligned proton-neutron pairs in the $g_{9/2}$ and $f_{5/2}$ orbitals, respectively. This conclusion seems to be valid according to the experimentally confirmed spins and parities of these states. It is interesting to compare the different theoretical $E2$ transition strengths for the $9^+_1 \rightarrow 7^+_3$ and $5^+_1 \rightarrow 3^+_1$ transitions with the ones derived from the experimental life times and conversion coefficients. The corresponding $B(E2)$ values are listed in Table 3.3, where experimental $B(E2)$ values, as reported in Ref. [69], are also included for comparison. It should be noted that those values are derived from experimental half-lives (superseded later in Ref. [73]) and conversion coefficients.

The extended P + QQ interaction with monopole corrections (hereafter called EPQQM) used in Ref. [78] produces $B(E2)$ values, which differ approximately by factors of 0.1 and 10 with the respective experimental values. The experimental level energies of the isomeric 9^+_1 and 5^+_1 states are, however, roughly reproduced by the calculation. The present calculation using the JUN45 interaction produces a $B(E2;\ 5^+_{1,th} \rightarrow 3^+_{2,th})$ value, which agrees well with the experimental one, suggesting that the model correctly describes the wave functions of the states involved in the transition. Nevertheless, the predicted level energy for the isomeric $5^+_{1,th}$ state is 0.95 MeV below the experimental counterpart. The theoretical $B(E2;\ 9^+_{1,th} \rightarrow 7^+_{2,th})$ is again too low by a factor of 10 and the $9^+_{1,th}$ level energy is 0.52 MeV below the experimental isomeric 9^+_1 state.

Nucleon occupancies of orbitals from the present shell-model calculation are presented in Table 3.4. This theoretical study and the one presented in Ref. [78] both predict $\sim$20 % occupation of valence nucleons in the $g_{9/2}$ orbit in the case of the isomeric $9^+_{1,th}$ state, while for the other calculated levels the $g_{9/2}$ occupation is on average only 3–6 %. This is especially true for the theoretical $7^+_{2,th}$ state, which the isomeric $9^+_{1,th}$ state is expected to decay into. This result implies that the isomerism of the $9^+_{1,th}$ state is indeed due to its structural difference compared to the $7^+_{2,th}$ state. However, the present shell-model calcu-

lation predicts another $7^+_{1,th}$ state with an almost identical orbital occupancy as obtained for the isomeric $9^+_{1,th}$ state. This structural similarity is naturally reflected in the pronounced $E2$ transition strength, which is of the order of 460 e^{2}fm^4. Taking this fact into account and remembering the theoretical underestimation of the $B(E2;\ 9^+_{1,th} \rightarrow 7^+_{2,th})$ value, one can speculate whether the mixing of the different 7^+ states is correctly reproduced by the theory. Alternatively, the effect of the $g_{9/2}$ orbit on the structure of excited states in ^{66}As could possibly be refined. The isomerism of the 5^+_1 is not likely to originate from major structural differences, at least in light of the calculated orbital occupation numbers, but can simply be explained by the low decay energy.

Table 3.3: Comparison of experimental and shell-model-predicted γ-ray transition strengths for ^{66}As.

$I^\pi_i \rightarrow I^\pi_f$	$B(E2;\ I^\pi_i \rightarrow I^\pi_f)$ [e^{2}fm^4]			
	Exp.	JUN45	EPQQM	Ref. [69]
$9^+_1 \rightarrow 7^+_3$	2.6(3)	0.22	0.36	0.7(1)
$5^+_1 \rightarrow 3^+_1$	13(2)	16.02	117.24	5.4(14)
	$B(E2;\ I^\pi_i \rightarrow I^\pi_f)$ [W.u.]			
	Expt.	JUN45	EPQQM	Ref. [69]
$9^+_1 \rightarrow 7^+_3$	0.16(2)	0.014	0.023	0.044(6)
$5^+_1 \rightarrow 3^+_1$	0.8(1)	1.01	7.40	0.34(9)

Table 3.4: Nucleon occupation numbers of orbitals in the four model-space orbits for low-lying $T = 1$ and $T = 0$ states in ^{66}As.

I^π_i,T	n^π_{lj}=n^ν_{lj}			
	$p_{3/2}$	$f_{5/2}$	$p_{1/2}$	$g_{9/2}$
9^+_1,0	1.606	1.857	0.461	1.076
9^+_2,0	2.081	2.189	0.537	0.194
7^+_1,0	1.589	1.869	0.474	1.068
7^+_2,0	2.198	2.037	0.528	0.237
6^+_1,1	2.300	1.825	0.569	0.306
5^+_1,0	2.739	1.230	0.853	0.178
5^+_2,0	2.320	1.855	0.575	0.250
4^+_3,1	2.416	1.643	0.623	0.318
3^+_2,0	2.460	1.682	0.612	0.246

3.3.2 Oblate 3^+ shape isomer

The existence of a $3^+_{1,th}$ shape isomer was predicted in Ref. [78]. The prediction of the isomerism arises from the calculated quadrupole moments from which one can infer an oblate shape for the $3^+_{1,th}$ state and prolate shapes for the other low-lying states. However, the predicted isomeric state was not found in the present study. The experimental setup used in this work has certain limitations to observe fast decays. This is due to the ∼700-ns flight time of fusion residues through the RITU separator. This limit is cross-section dependent, but if the isomer exists, the life time of the state should be of the order of > 100 ns to be observed at the focal plane of RITU. Also, the 10-ns time resolution of the TDR does not permit the investigation of small time differences of the γ rays measured at the JUROGAM II target position.

Recent experimental work on ^{66}As reported in Ref. [70], led to the discovery of a 3^+_2 state with a 1.1(3)-ns half-life, which was determined on the basis of the centroid-shift method [80]. This state is proposed to be the predicted oblate shape isomer and is de-excited by a strong 379-keV $M1$ and a weaker 506-keV and a non-observed 112-keV γ-ray transitions. In the present study a 3^+_2 state, which is de-excited similarly by the strong 379-keV $M1$ and weaker 506-keV ($E2$) γ-ray transitions, was identified. It is reasonable to assume that it is the same 3^+_2 state, which has been successfully discovered in both experiments. However, no 112-keV γ rays originating from ^{66}As were observed in the present study. In Ref. [70] the non-observation of the 112-keV transition is explained by the germanium array detection efficiency, which was reduced due to the strong absorption in the CsI charged particle ancillary detectors used in that experiment. With the JUROGAM II array such limitations were not present and therefore the reported 112-keV transition with 6 % intensity should have been observed.

If the 3^+_2 state has ∼1-ns half-life, the γ-ray emission should take place 0−30 mm downstream from the JUROGAM II target position. This would cause a slight drop in the detection efficiency of the 379- and 506-keV γ rays, but more importantly, the change in the detection angle would lead to an incorrect Doppler correction or a shift of a few keV in the measured γ-ray energy in the 75.5° and 104.5° JUROGAM II rings. This should be observable in the γ-ray spectrum as a broadened or skewed peak shape. The peak shapes of the 355-, 379- and 394-keV transitions were examined but no differences in their respective shapes were observed. This might be due to the fact that the energy broadening is not strong enough in the case of the 379 keV transition or the 3^+_2 state has a shorter half-life than that reported in Ref. [70].

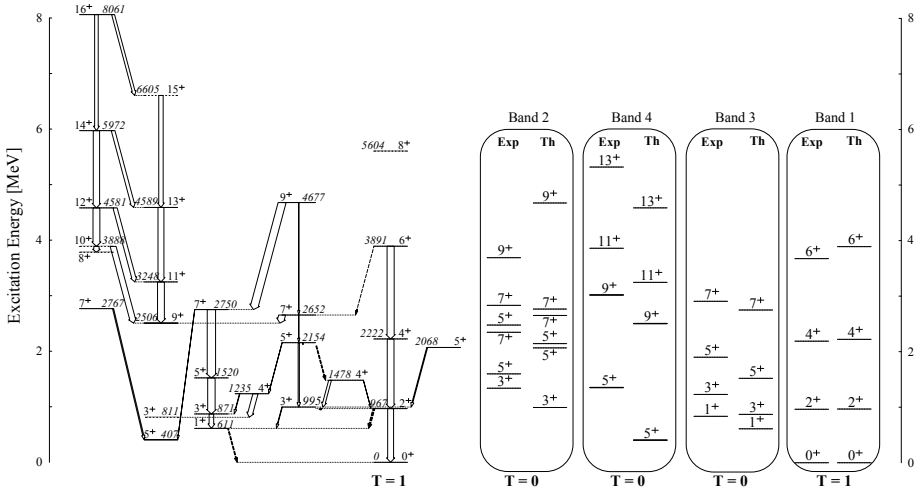

Figure 3.13: (Left) The energy levels of ^{66}As predicted by the present shell-model calculation. The width of the arrow corresponds to the relative value of the calculated $E2$ (solid arrow) and $M1$ (dashed arrow) transition strengths. The dashed levels are theoretically predicted but not observed in the experiment. (Right) Comparison of the experimental (Exp) and theoretical (Th) level energies for the $T = 1$ (right) and different $T = 0$ sequences.

3.3.3 T = 1 and T = 0 states

The present shell-model calculation reproduces the level energies of the $T = 1$, 2_1^+ (967 keV), 4_3^+ (2222 keV) and 6_1^+ (3891 keV) states in relatively good agreement with the experimental 2_1^+ (963 keV), 4_3^+ (2189 keV) and (6_1^+) (3674 keV) states (see Fig. 3.13). Recent theoretical work by Kaneko *et al.*, [16], which again is based on calculations identical to those used in the present work, predicts the Coulomb energy differences (CED, see Eq. 1.6) between the $T = 1$ states in odd-odd $N = Z$ systems and their analogue even-even partners. Recent experimental work on ^{66}As [70] proposes a $T = 1$, 6_1^+ state at an energy of 3637 keV, which results in the initially positive CED trend between ^{66}As/^{66}Ge having a sudden negative gradient at spin $6\hbar$. In Ref. [70] this unusual behaviour, along with the unique negative CED trend observed within the $A = 70$ pair (^{70}Br/^{70}Se), was accounted for by the different mixing of competing shapes between the isobaric analogue states. However, in Ref. [16] the shell-model calculations correctly reproduce the negative CED trend for the $A = 70$ pair with a nearly static oblate deformation in ^{70}Se. The main reason for the anomalous trend in the latter work is found to be the enhanced neutron and reduced proton excitations to the $g_{9/2}$ orbit due to the electromagnetic spin-orbit interaction ϵ_{ls}, which shifts the corresponding single-particle orbitals in opposite directions

(see Eq. 1.4). In the present work, the candidate for the $T = 1$, 6_1^+ state is found to lie at 3674 keV, 37 keV higher than proposed in Ref. [70]. This leads to a moderately positive CED behaviour within the $A = 66$ pair as illustrated in Fig. 3.14. A similar trend is also predicted by the present theoretical calculation, if one particularly considers the first $6_{\rm th}^+$ states (see Fig. 3.14). Figure 3.14 shows also heavier systems for comparison. In the case of the mass $A = 74$ and 78 pairs, large positive and almost flat CED trends are observed, respectively. Generally, the positive CED trends are explained by multipole Coulomb effects such as the Coriolis antipairing, *i.e.,* breaking of valence nucleon pairs when angular momentum is generated [23]. This causes the even-even $N = Z - 2$ partner to have a greater reduction in Coulomb energy since it has more pp pairs than the odd-odd $N = Z$ partner of the multiplet. In the case of the $A = 78$ pair, an almost flat CED is attributed to the deformed shell gap at Z, $N = 38$, which inhibits shape changes and suppresses pairing effects [81]. The observed CED trend for the $A = 66$ pair is only slightly steeper than the one observed for the $A = 78$ pair. Clearly, the Z, $N = 38$ shell gap will not have any significant influence in the case of ^{66}As. In addition, taking into account the recent theoretical result for the mass $A = 70$ pair, coexisting shapes may not necessarily be the origin of the observed flatness in the CED behaviour in the case of the mass $A = 66$ pair. In Ref. [16] the single-particle energy-shift component, which is greatly affected by the electromagnetic spin-orbit interaction, is found to flatten the CED trend for the $A = 66$ system, as it is purely negative as in the case of the $A = 70$ pair. This hints toward the importance of the $g_{9/2}$ orbit and its interplay with the fp-shell orbits in the structure of the ^{66}As.

In Fig. 3.2 the tentative 840-keV γ-ray transition connecting the supposed 6_1^+ state and the 7_2^+ is very interesting. The quasideuteron description [85] can be used to estimate and predict the isovector $M1$ transition strengths in odd-odd $N = Z$ nuclei. According to this approximation, the $M1$ transition strength is greatly dependent on the characteristics of the single-particle orbits contributing to the level configuration. In the case of $j = l + 1/2$ orbitals, the spin of the nucleon and orbital angular momentum are aligned and strong isovector $M1$ transitions are favoured. If the single-particle orbital is of type $j = l - 1/2$, the spin and orbital parts are out of phase, resulting in small $M1$ matrix elements. Obviously, as the low-lying excitations in ^{66}As are presumably mainly based on the $f_{5/2}$ ($j = l - 1/2$) and $p_{3/2}$ ($j = l + 1/2$) configurations, a strong $M1$ transition between the lowest $T = 0$ and $T = 1$ states, *i.e.,* between 2_1^+ and 1_1^+, is experimentally missing. The situation, however, might be different at higher values of angular momentum. As already noticed in the case of the 9_1^+ isomeric state, the importance of the $g_{9/2}$ ($j = l + 1/2$) orbit is evident. If one considers the situation where the amplitude of the $g_{9/2}$ component increases along with spin within the $T = 1$ band, $M1$ transitions may become the dominant decay mechanism over $E2$ transitions. This appears to be the case for the 6_1^+ state where the 840-keV γ-ray branch to the $T = 0$, 7_2^+

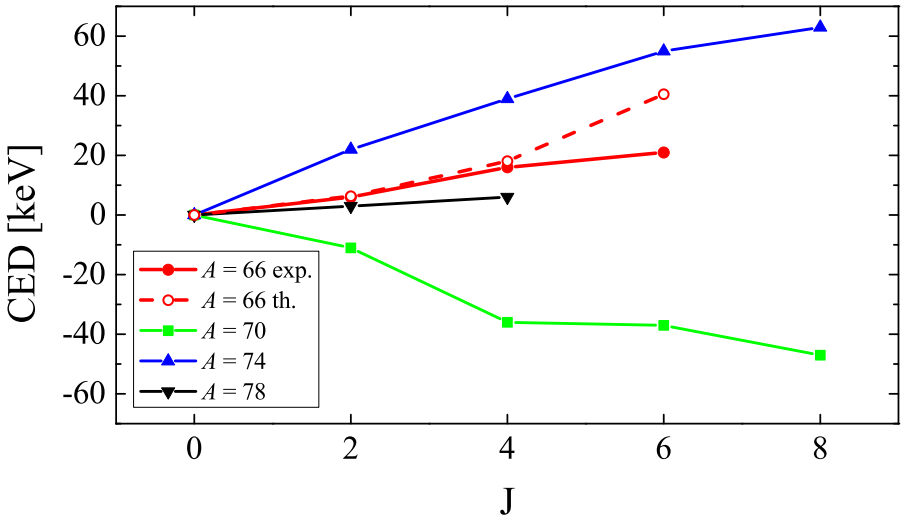

Figure 3.14: The experimental CED systematics for the mass $A = 66$, 70, 74 and 78 systems (solid lines). The shell-model predicted CED for the mass $A = 66$ pair is shown as dashed line. Data are taken from Refs. [79, 82, 83, 23, 84].

state is greater (82 %) than the 1486-keV γ-ray branch feeding the $T = 1$, 4_3^+ state (18 %). The $B(M1)$ value for the $6_1^+ \rightarrow 7_2^+$ transition can be estimated in a manner similar to that used in Ref. [86] by using the experimental branching ratio and recently measured $B(E2; 2_1^+ \rightarrow 0_1^+)$ value in ^{66}Ge [87]. Assuming the $B(E2)$ value does not significantly change between higher lying $T = 1$ states in ^{66}Ge, the $B(M1; 6_1^+ \rightarrow 7_2^+)$ value is estimated to be $\sim 1\mu_N^2$, which is surprisingly large. The present shell-model calculation does not support this scenario in terms of $M1$ transition strengths and $g_{9/2}$ occupancy (see Table 3.4). If the monopole matrix elements are correctly described by the theory, this should lead to a rather high $M1$ transition strength in the case of the 3_2^+ state decay in order to explain the experimentally observed favouring of the $M1$ branch over the $E2$ branch, but such an enhancement was not predicted.

The theoretically predicted level energies of the low-lying $T = 0$ states are in relatively good agreement with the experimental ones. The agreement is particularly good in the case of Band 3 ($T = 0$), which is connected to the isomeric states. The theory predicts three 7^+ states with similar energies, which agrees extremely well with the experimental data. The theoretical description fails in the case of Band 4 and 5 in terms of excitation energy and level spacings. Despite the daunting task of theoretically describing odd-odd $N = Z$ systems, the current model is found to be in relatively good agreement in the case of the low-lying excitations of ^{66}As. This fact is reflected in the experimental and theoretical $B(E2; 5_1^+ \rightarrow 3_1^+)$ values, which are in remarkable agreement.

Chapter 4

Enhancing the sensitivity of recoil-β tagging

The RBT technique was first validated in 2005 by Steer *et al.,* [34] by studying ^{74}Rb. The level structure of this nucleus had been studied previously using more conventional techniques. Selecting high-energy positrons detected in the planar germanium detector within a 100 ms correlation window of the recoil implantation allowed γ-ray transitions associated with the decay of excited states in ^{74}Rb to be cleanly identified. Following on from this verification of the RBT approach, it was applied to the identification, for the first time, of excited states in ^{78}Y in 2006 [23]. The RBT program was continued in order to gain information of even more exotic cases such as ^{70}Kr and ^{71}Kr. However, these experiments failed to shed light on the structure of these nuclei due to technical difficulties. The analysis of these data led to the identification of development needs in order to study the exotic neutron-deficient nuclei residing at or beyond the $N = Z$ line. Despite the initial success of the RBT technique, it has proved challenging to apply it to more than a handful of cases. The challenge relates to achieving the sensitivity needed to cleanly select the channel of interest, since a β decay does not provide a discriminating tag in the same way as a characteristic α decay does as discussed in section 2.4. In this chapter, the issues related to improving the sensitivity, both in terms of modifying the way that the RBT technique is applied and specific instrumentation developed to enhance the sensitivity are reviewed.

4.1 The challenge to increase sensitivity

It is desirable to push the RBT technique to the limits and identify excited states in exotic nuclei on and beyond the $N = Z$ line. To allow for this advance, the technique of double-RBT has been devised. Consider, for example, ^{74}Sr, which decays by superallowed β decay to ^{74}Rb, which will in turn β decay to ^{74}Kr. Detecting two fast β decays in a single pixel of the DSSD would provide a unique tag to select such extremely exotic nuclei with cross-sections of only 100 nb. This approach was found to be unviable with the original detector setup, because the false correlation rate was simply too high due to the very large difference in cross-section between such exotic channels and the total fusion cross-section, which is of the order of 100 mb. This is perhaps unsurprising in light of the γ-ray spectra presented in chapter 3, where contaminants are visible in some of the spectra despite the rigorous cleaning attempts. The obvious conclusion was that to expand the applicability of these techniques, the experimental sensitivity needed to be enhanced. As a first step to improve the RBT approach, the suppression of dominating charged-particle evaporation channels was performed. Secondly, in order to reduce the rate of false correlations, the pixellation of the DSSD was increased. Thirdly, identification and discrimination of high-energy β particles over low-energy and randomly coinciding low-energy β events was improved. A major improvement, still awaiting completion, is the mass selection of the recoils. A new vacuum-mode recoil separator MARA [88], which is presently under construction at JYFL, will undoubtedly help to further suppress the contaminating reaction channels.

4.2 New detector elements

4.2.1 The charged-particle veto device - UoYtube

The major contributors to contamination in RBT studies in the proton rich $A \approx 70$ region are multiple charged-particle evaporation channels, while the channel leading to the odd-odd $N = Z$ nucleus is typically pn evaporation, or 2n evaporation for production of $N = Z - 2$ nuclei. Detecting evaporated charged particles with high efficiency can be used to reduce contamination for both the pn and 2n fusion evaporation channels. A veto barrel detector called UoYtube (the University of York tube) was designed and constructed at the University of York, UK. It comprises 96 CsI(Tl) detectors arranged on six faces of a hexagonal barrel (see Fig. 4.1). Each CsI(Tl) crystal is 20 x 20 mm^2 and 2 mm thick. The dopant thallium is used as it shifts the emission spectrum of light in the long wavelength region (>500 nm) and is thereby well-suited for compact photodiode readout. The scintillator crystals are glued on top

of the light guides (see Fig. 4.2), which are coupled to S3590-08 PIN diodes from Hamamatsu. The photodiodes were biased through the Mesytec MPR-16 preamplifiers to +50 V by Mesytec MHV-4 power supplies. The negative signals from each detector channel were fed to preamplifiers, which were powered by Mesytec MNV-4 NIM voltage supplies. The preamplifier signal was fed through a gain and offset box with signals then interpreted with a moving-window deconvolution algorithm [55] in Lyrtech ADCs. Whilst at present no attempt is made to separate protons from α-particles, this will be useful in regions where channels such as the αpn have significant cross-sections. In principle, pulse-shape analysis could be implemented into the digital electronics. This would allow charged-particle discrimination, without the memory intensive task of recording wave-forms for all CsI(Tl) channels. A further development being considered is the use of segmented silicon photomultipliers. A higher angular resolution especially for the α-particle detection would allow a better reconstruction of the evaporation kinematics. In this way, the velocity vector of the recoil can be determined more accurately and consequently a better resolution in the γ-ray spectrum could be achieved.

4.2.2 A highly-pixelated DSSD

In the original RBT work, two 700-μm thick DSSDs were used for implantation and decay measurements at the focal plane of the RITU separator. As already mentioned in sections 2.2.3 and 3.2.1, the performance of RITU is not optimal for studies at and below the $A = 100$ mass region so it was challenging to separate the fusion evaporation residues from scattered beam. The consequence of this was that the residues could only effectively be implanted on one of the two DSSDs and the second DSSD was essentially redundant as illustrated in Fig. 4.3. In order to achieve a higher pixelation over a concentrated area, a new DSSD was purchased. This detector was a 500-μm thick Micron BB13 with dimensions of 60 $\times$ 60 mm and a strip pitch of 0.48 mm in both the x- and y-directions. However, only the centre 80 strips were read out of the horizontal strip side as the DSSD cooling block was shadowing the outermost edges of the detector. The new DSSD represents a reduction of pixel size by a factor of four compared to the previous device. The DSSD is positioned so as to be centered on the region of high intensity on the old DSSD. The measured recoil distribution with the new DSSD is shown in Fig. 4.4 and the photograph of the new detector is shown in Fig. 4.5.

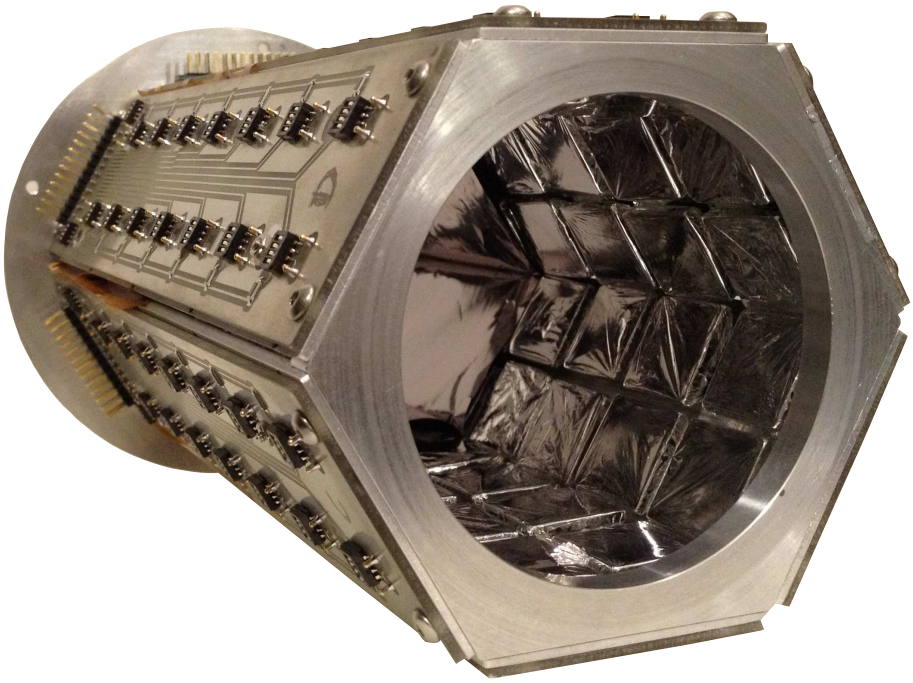

Figure 4.1: Photograph of the UoYtube charged particle veto box from beam direction. 96 CsI(Tl) crystals are arranged around the 6 sides of a hexagonal barrel. Each crystal is sealed within thin mylar foil and Ni foils with thickness of 2.5 μm were applied to all surfaces at forward angles covering the first four pairs of crystals.

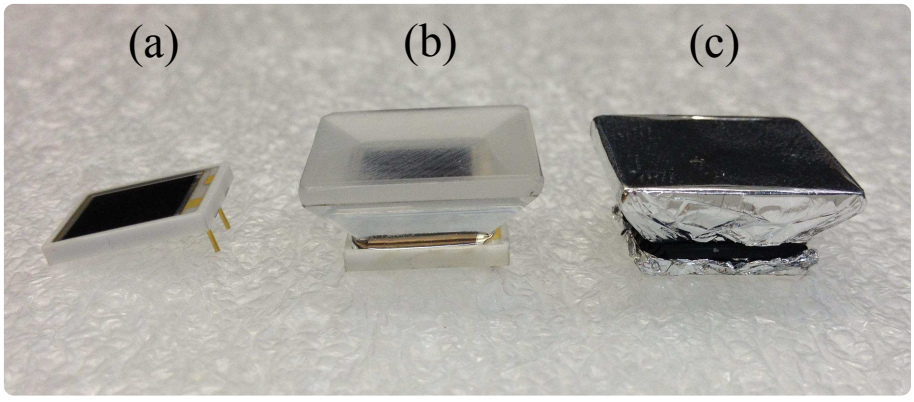

Figure 4.2: Photograph of (a) S3590-08 PIN diode, (b) CsI(Tl) crystal glued on top of a light guide and (c) detector element at the ready.

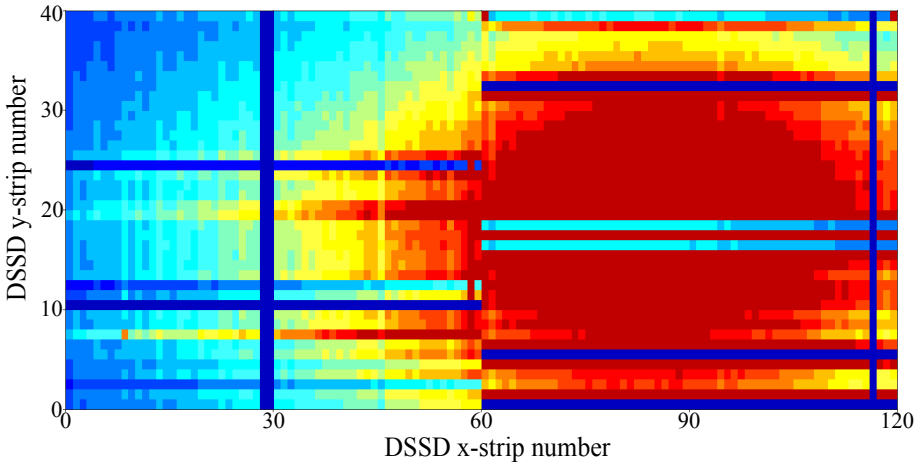

Figure 4.3: Typical pixel map for the original GREAT configuration of two adjacent DSSDs when studying the ^{40}Ca(^{28}Si,pn)^{66}As reaction. Low-rate region is indicated in blue whereas high-rate regions are in yellow→red. It should be noted that the 120 vertical strips correspond to the detector width of 120 mm.

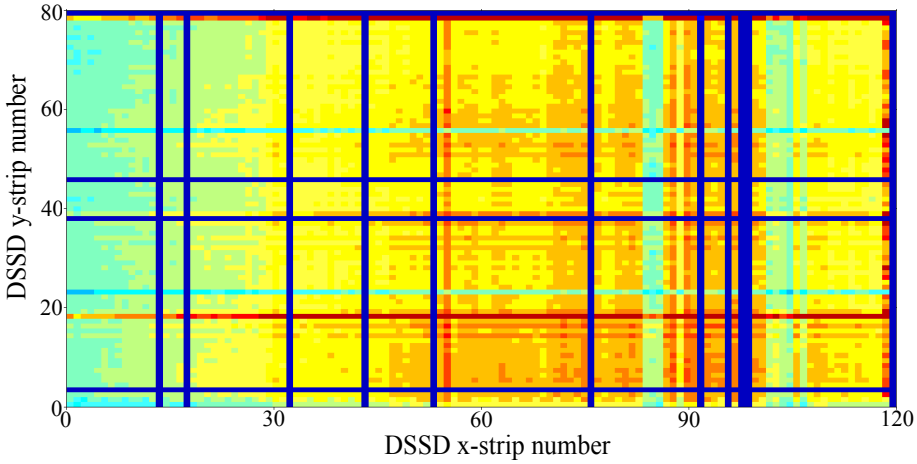

Figure 4.4: Typical pixel map for the new highly-pixelated DSSD when studying the ^{40}Ca(^{28}Si,pn)^{66}As reaction. Low-rate region is indicated in blue whereas high-rate regions are in yellow→red. It should be noted that the 120 vertical strips correspond to the detector width of 60 mm.

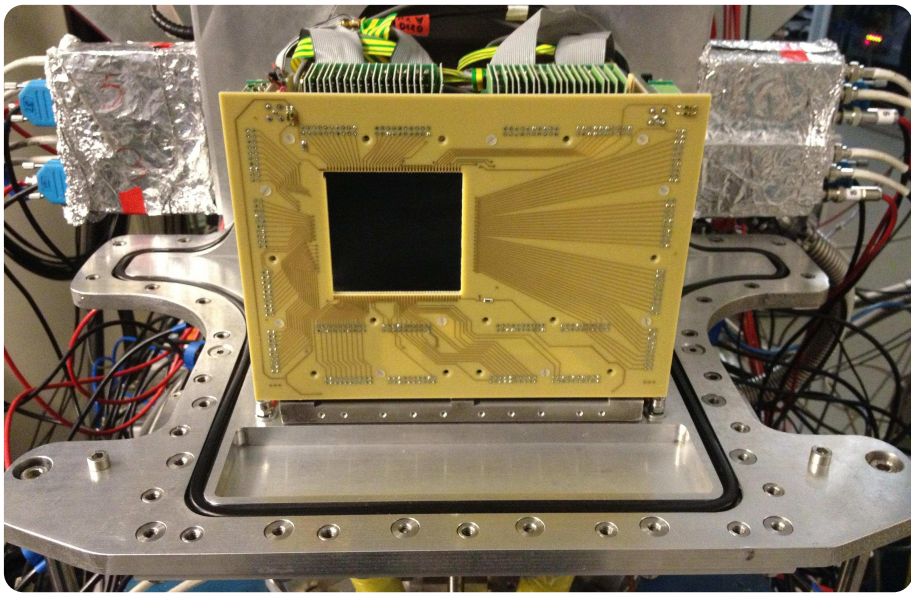

Figure 4.5: Photograph of the new DSSD installed at the focal plane of RITU.

4.2.3 A phoswich detector for high-energy β-particle selection

In developing the RBT methodology from the initial demonstration, the planar germanium detector was replaced with a plastic scintillator detector of a similar size [89]. The plastic scintillator was fast and a good signal could be obtained for high-energy β particles. A phosphor-sandwich (phoswich) detector is an attractive replacement for this simple detector as a better means of discriminating different types of ionising radiation. Such detectors are widely used for particle identification [90, 91]. They are typically made up of two or more blocks of scintillator material with different timing properties. Through the analysis of pulse shapes, one can identify where the interaction occurred within the detector, allowing for their use as $\Delta E - E$ devices.

To better characterise high-energy β particles for the RBT application, the simple plastic scintillator was replaced with a phoswich detector comprising a 10-mm thick fast-response plastic scintillator (BC-404, total pulse length $\sim$80 ns) optically coupled to a 31.5-mm thick slow-response plastic scintillator (BC-444, total pulse length $\sim$700 ns). These are then attached to a light guide below the scintillators, which couples to three 10 stage Hamamatsu R3318-01 photomultiplier tubes (PMT) (see Fig. 4.6). To conserve the different pulse shapes, signals from the PMTs have to be extracted directly from the anode.

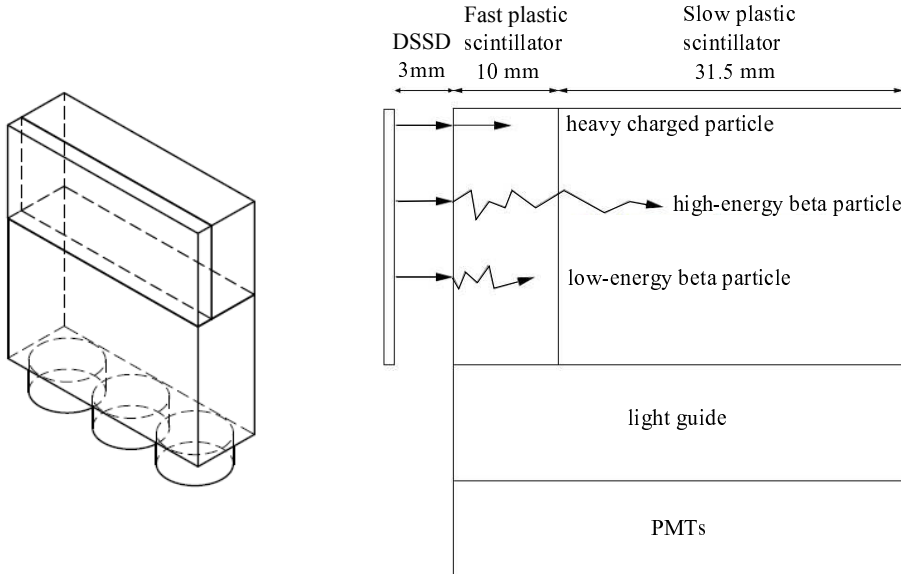

Figure 4.6: (Left) A schematic of the phoswich. A 10 mm fast-response plastic scintillator (BC-404) is coupled with a 31.5 mm slow-response plastic scintillator (BC-444). The photomultiplier tubes are attached to a light guide, which is coupled with the scintillators. (Right) Heavy charged particles and low-energy β particles are stopped within the fast plastic, whereas high-energy β particles pass through the fast plastic to the slow plastic scintillator.

It was found that the Hamamatsu C7319 preamplifiers, previously used with the PMTs, caused the loss of the pulse-shape information due to a long current-to-voltage conversion time. To ensure that the pure anode signal exceeds the trigger threshold set in the Lyrtech ADCs, the outputs of the PMTs were coupled together to provide one linearly summed signal. The phoswich is placed into the original position of the planar germanium detector, with the fast plastic abutting the DSSD. High-energy β particles continuously deposit energy along their track, penetrating to the slow plastic scintillator at the rear. In contrast, β particles with energies lower than 2−3 MeV will only deposit energy in the front fast plastic, while γ rays interact discretely and would typically register only in one of the two sections, preferentially in the slow element due to the larger physical size.

4.3 In-beam experiments

Two in-beam experiments have been conducted to evaluate the performance of the new detector elements. The first one was to inaugurate UoYtube in August 2011. The second one was to study the new DSSD and phoswich detectors in May 2012. For both experiments, recoils were identified using RITU and the GREAT focal plane spectrometer. Emitted γ rays were detected at the target position by the JUROGAM II array. However, for both experiments described below, 5 upstream Phase 1 type detectors were not mounted, which led to a γ-ray detection efficiency of 5.5 % at 1.3 MeV. Both experiments utilised 75 MeV ^{28}Si beam provided by the K-130 cyclotron, which was bombarded on a ^{nat}Ca target of thickness 0.65 mg/cm^2. A ^{nat}C charge-reset foil of thickness 0.05 mg/cm^2 was set directly behind the target. Beam intensities were maintained at between 2−7 pnA, which led to DSSD rates of between 3−10 kHz. The channel of interest for the following experiments was ^{40}Ca(^{28}Si,pn)^{66}As in order to make a direct comparisons of the data quality with the first ^{66}As experiment, which was successfully conducted in July 2009 (see chapter 3). In addition, this reaction was a natural choice as the cross-section was known to be high enough for tests to be completed with short run-times.

The remainder of the setup was made up of the GREAT MWPC and, for the UoYtube experiment, the GREAT DSSD and segmented planar germanium detector. Recoils were again selected using $\Delta E-$ToF and $E-$ToF information. Here E is the energy of the recoiling nucleus deposited in the DSSD, ΔE is extracted from the MWPC and the ToF is extracted from the MWPC and DSSD signals. The UoYtube experiment had a duration of 2 days. The phoswich/DSSD study duration was also 2 days with an additional 1.8 days running with the new DSSD in combination with the planar germanium detector. It should be noted that in these experiments JUROGAM II was fully digitized with Lyrtech electronics as opposed to the first ^{66}As experiment, where all phase 1 type of germanium detectors were instrumented with analogue electronics. To summarise, the relevant details of all experiments presented and discussed in this thesis are shown in Table 4.1.

4.3.1 A study of UoYtube

The UoYtube veto-box was mounted at the target position of JUROGAM II in the Light Ion Spectrometer Array (LISA) target chamber [92]. This chamber was designed for the mounting of Si detectors for fast proton- and α-decay studies and was used, most importantly, because it was already existing and large enough to accommodate UoYtube. The use of the LISA chamber came at the expense of the first JUROGAM II ring housing 5 phase 1 type detectors, which was due to the large physical size of the chamber. All CsI(Tl) crystals

Table 4.1: Experimental details of the different recoil-β tagging measurements presented and discussed in this thesis. The ^{28}Si + ^{nat}Ca reaction has been employed in the first four experiments, whereas ^{36}Ar + ^{nat}Ca was used in the ^{74}Sr experiment.

Exp.	ancillary detectors	β detector	digital electronics	target [μg/cm^2]	E_b [MeV]	I_b [pnA]	duration [h]	year
^{66}As	–	-planar Ge	-JII clovers (TNT2)	800	83 75	3 7	40 120	2009
^{66}Se	-UoYtube	-planar Ge	-full JII (Lyrtech) -UoYtube	650	75	2–3	36	2011
new DSSD	–	-phoswich	-full JII (Lyrtech) -FP clovers -new DSSD -PMTs	650	75	2–4	46	2012
new DSSD	–	-planar Ge	-full JII (Lyrtech) -FP clovers -new DSSD	650	75	3,5,7	40	2012
^{74}Sr	-UoYtube II	-phoswich	-full JII (Lyrtech) -UoYTube II -FP clovers -new DSSD -PMTs	600	95	5–6	130	2013

were sealed within thin aluminised mylar foils in order to prevent the scintillation light escaping from the crystals and also, to protect the photodiodes from external light. In addition, the four downstream pairs of CsI(Tl) crystals at each flange were covered with 2.5-μm thick nickel foils to stop scattered ^{16}O (from target oxidation) and ^{12}C (from reset foil) particles. During the study it was found that the thickness of the nickel foil was not enough to stop all scattered particles. For this reason 9.0-μm thick tantalum foils were added on top of the Ni foils. It should be noted that a certain amount of scattering was observed at backward angles, which implies that stopper foils should also be applied to upstream surfaces in the future.

Due to an error in the design of UoYtube, there were ∼5-mm gaps between each crystal at longitudinal direction. This resulted in incomplete angular coverage (62 % of 2π), which is illustrated in Fig. 4.7 as dashed grey regions. The calculated geometrical charged-particle detection efficiency of the UoYtube for the beam and target used is approximately 73 % (see Fig. 4.7). This value is approximately valid for both protons and α-particles as the shapes of their respective angular distributions are almost identical. The calculated geometrical detection efficiency value leads to a theoretical suppression factor of 51 for the 3p channel, which in turn correponds to a detection probability of 98 % for the case that at least one out of the three evaporated protons is detected. The experimental value for the charged-particle suppression can be derived by comparing vetoed and non-vetoed prompt recoil-gated γ-ray spectra. Using the ratio of the 191-keV lines originating from the ^{40}Ca(^{28}Si,3p)^{65}Ga channel in these two cases leads to a suppression factor of 22(3), which is equivalent to the detection probability of 95(1) % for the case that at least one out of three protons is detected. The detection probability for two protons and detection efficiency for a single proton can be derived from this value and they are 86(2) % and 63(3) %, respectively. As the latter value shows, there seems to be an additional 10 % drop in the measured detection efficiency for one charged particle. This might be explained by the performance issues of individual crystals, scattering effects and possible losses in signal processing. In addition, it was found that the inclusion of the UoYtube suppressed the amount of contaminant statistics by more than a factor of three for events in which a single charged particle was detected in the UoYtube, depending on the energy and timing gates applied to UoYtube. Due to incomplete angular coverage and other reductions in efficiency, a veto strategy requiring ≤ 1 charged-particle events was found to provide the best contaminant suppression for the pn channel whilst maintaining good statistics, as shown in Fig. 4.8. The channels with no charged-particle evaporation are those, which are of most interest for studies of $N < Z$ nuclei in the $A \approx 70$ mass region, so the high suppression factor for such channels is vital. Indeed, the identification of excited states in ^{66}Se (the 2n channel), was achieved during the study of the UoYtube and these results are presented and discussed in chapter 5.

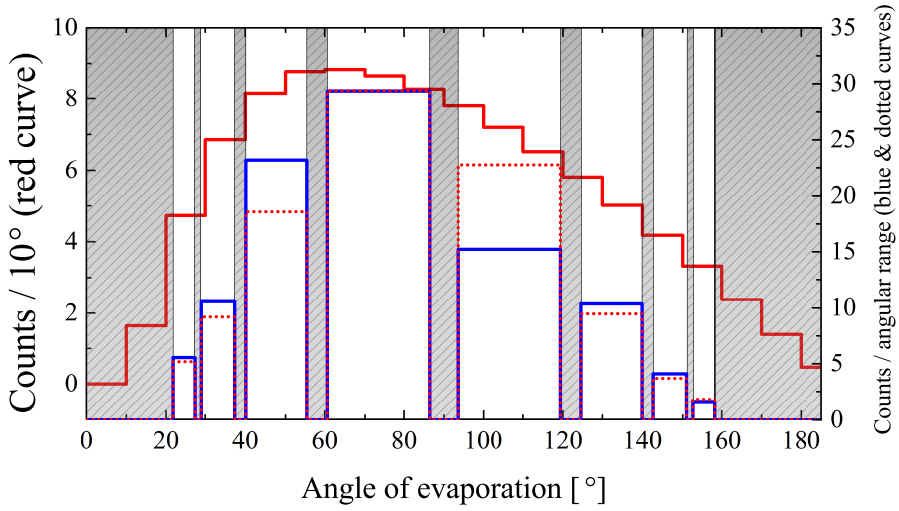

Figure 4.7: Calculated (solid red curve) and experimental (blue curve) angular distributions of emitted protons and α particles for a 75-MeV ^{28}Si beam bombarded on a ^{40}Ca target. Angular intensities are calculated with the PACE4 code [57]. The dashed regions indicate angular regions at which the UoYtube is insensitive due to gaps between detector elements. The dotted red curve illustrates the calculated angular distribution of evaporated charged particles in the sensitive regions. This graph indicates that 73 % of charged particles are emitted at angles which the UoYtube is sensitive to. The measured detection efficiency for one charged particle is 63(3) % .

4.3.2 A study of the highly-pixelated DSSD and phoswich detector

The new DSSD was mounted in place of the previous pair of DSSDs in the GREAT chamber. The phoswich detector was mounted in the original position of the planar germanium detector. Pulse shapes were recorded for the phoswich detector with digital Lyrtech ADCs. It was the intention that, ultimately, pulse shape analysis for the phoswich could be achieved online using the field-programmable gate array (FPGA) hardware on the Lyrtech cards, which would permit high rates. In the test, analysis of the pulse shapes was carried out offline. The first stage of the analysis was a constant background approximation and subtraction. An average signal height is taken in the region before the pulse and then subtracted throughout the length of the signal. A 100-ns window was then integrated over the fast element of the pulse, with an integration over the remainder of the pulse being used to determine the slow elements. The phoswich matrix generated from pulse shapes recorded for interactions in

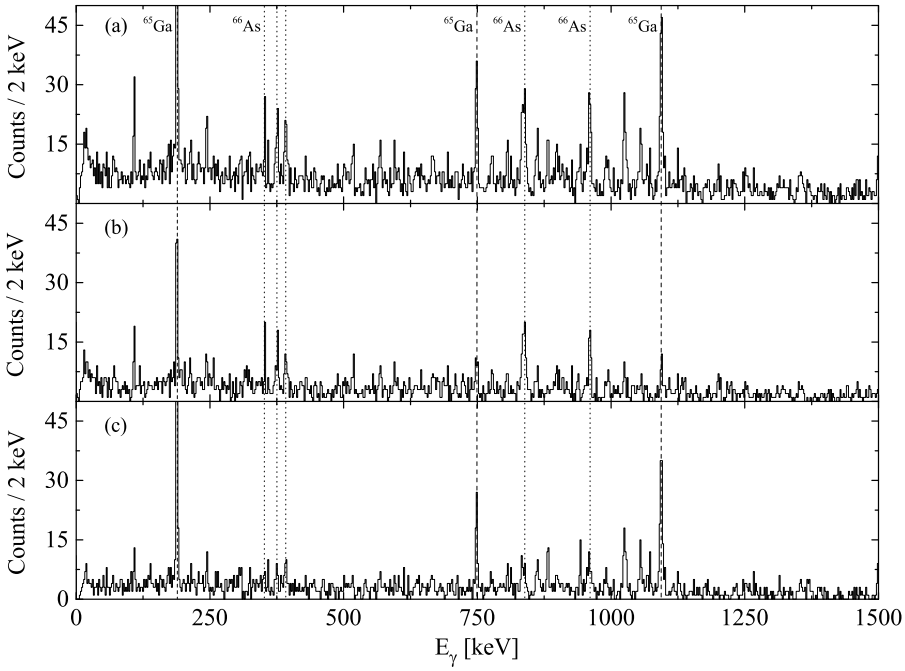

Figure 4.8: Recoil-β tagged JUROGAM II singles γ-ray spectra using a 300 ms correlation time and 1.5−10-MeV β gate with (a) no requirements for the charged particles (cp), (b) requiring ≤ 1 cp events and (c) requiring > 1 cp events. The γ rays corresponding to ^{66}As (pn channel) are indicated by the dotted lines, whilst γ rays originating from ^{65}Ga (3p channel) are indicated by the dashed lines. Contaminants are reduced by more than a factor of 3 by the vetoing strategy in (b). As the detected cp fold distribution peaks at value of 2 with the current β gate, the ^{66}As γ-ray lines are also visible in (c) *i.e.,* the ^{66}As recoils are accidentally correlated with 2 cp evaporation.

the fast plastic, slow plastic and the combined system are shown in Fig. 4.9. Analysis of the data was carried out using GRAIN in the same manner as that described in section 2.4. Events which are not valid recoils are considered as candidates for β decays, and their validity is assessed by passing them through a β-selection gate from the phoswich matrix such as that shown in Fig. 4.9 as a blue tetragon. This gate requires that the phoswich signal had strong fast and slow components, corresponding to the β particle punching through the fast phoswich element. A time window of 200 ns was placed on the phoswich-DSSD coincidences. By using the sum of the fast and slow elements of the signal, an alternative β-particle selection method is also possible with the phoswich used in a similar manner to the planar detector.

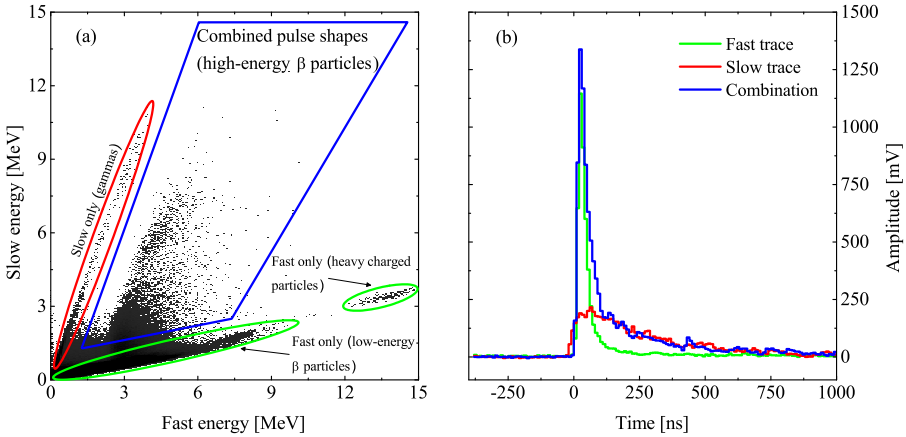

Figure 4.9: (a) Slow against fast phoswich signals, where fast signals are those resulting from an integral over the first 100 ns after the trigger, and slow signals are the integral over the remainder of the pulse. High-energy β particles can be identified as the region protruding above the line corresponding to the fast only signals. A typical high-energy β-particle gate is indicated by the blue tetragon. (b) Typical pulse shapes for interaction in the fast plastic (green), slow plastic (red) and in both elements (blue).

As mentioned earlier, data with the new DSSD were also collected in conjunction with the planar germanium detector. This enabled an one-to-one comparison with the original ^{66}As data, which was taken with the old 700-μm thick DSSD. In this part of the test, the data were collected with various beam intensities to study the evolution of false correlations. Three different beam intensities were used representing low (I_b = 3 pnA), medium (I_b = 5 pnA) and high (I_b = 7 pnA) running speeds. The comparison of these data and quantitative analysis is carried out in the next section.

4.4 Characterisation of the new setup

The UoYtube veto analysis was carried out offline utilising the GRAIN analyzer. This allowed comparisons to be made between the vetoed and non-vetoed spectra revealing any improvements. Two different reaction exit channels were considered as two different types of background events. As was discussed in section 2.4, the ^{40}Ca(^{28}Si,3p)^{65}Ga channel was found to give rise to the false correlations as it is populated with very high cross-section. The ^{40}Ca(^{28}Si,2p)^{66}Ge channel was populated with a lower cross-section and it was found to behave according to the set tagging conditions *i.e.,* it was not falsely correlated. There-

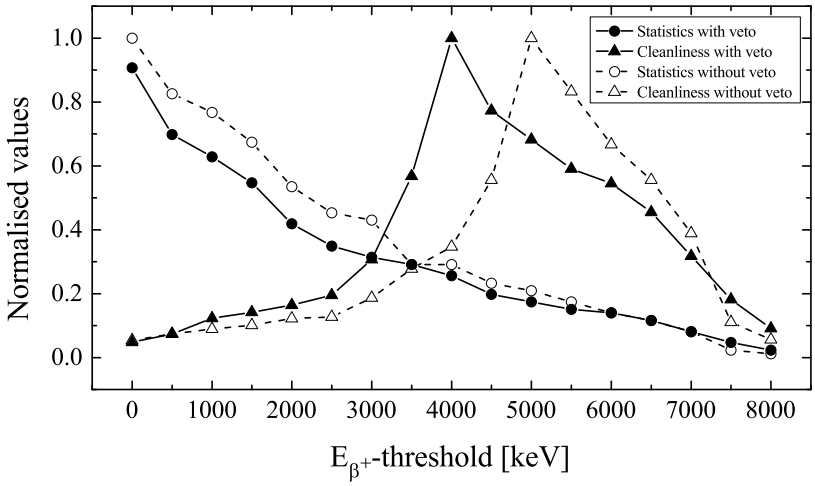

Figure 4.10: The cleanliness (triangles) and amount of statistics (circles) for the UoYtube setup without a vetoing strategy (unfilled points) and with a requirement that ≤ 1 charged particle is detected in the UoYtube (filled points). The trend indicates a lower β-energy threshold can be used with the UoYtube to achieve optimal cleanliness, which in turn allows the use of a higher amount of γ-ray data in the analysing process.

fore, it was used to define the cleanliness of the setup. The cleanliness was defined as the ratio of intensities of the 963-keV γ rays corresponding to the $2^+ \rightarrow 0^+$ transition in ^{66}As and the 957-keV γ rays corresponding to the $2^+ \rightarrow 0^+$ transition in ^{66}Ge. The cleanliness achieved with the UoYtube setup is shown in Fig. 4.10. Here, the amount of statistics corresponds to the number of events in the ^{66}As 963-keV peak. It can be seen that the addition of the UoYtube veto reduces the optimal threshold energy for the β particles - that where the maximum cleanliness is achieved - by approximately 1 MeV. This reduction makes a larger fraction of the β-particle energy distribution available with cleaner correlations, leading in turn to greater and cleaner γ-ray statistics. It must be noted that the use of the UoYtube veto reduces good events as well as bad, with at least a 10 % reduction in good events for the same threshold energy. This can be slightly more if timing and energy conditions are loosened, because more uncorrelated target position charged particles are accepted in the gates. However, any loss is offset by the increased number of good events, which occur above the new lower threshold energy.

As mentioned earlier, β-decay selection with the phoswich detector can be made in two different ways, a selection on the fast element vs. the slow element of the signal. Alternatively, one can use the sum of the fast and slow elements as a threshold energy, in the same manner as for the planar germanium detector.

Figure 4.11 shows the result of the different tagging techniques with 200 ms correlation time. The spectrum illustrated in Fig. 4.11(a) does not have an energy requirement for the detected β particles. The spectrum shown in Fig. 4.11(b) uses the sum of the fast and slow signals as a gate and the threshold is set approximately at 2 MeV. In the case of the spectrum shown in Fig. 4.11(c), the tagging is performed with β particles falling within the 2D phoswich gate shown in Fig. 4.9(a). The threshold energy selected for spectrum (b) was chosen to be approximately equivalent to the lowest energy accepted by the 2D phoswich gate used in spectrum (c). It can be seen from Fig. 4.11(c) that, whilst the use of pulse shapes from the phoswich device probably helps reducing the false correlations originating from two randomly coinciding low-energy β particles, it does so at the expense of good events in the 836-keV ^{66}As peak. However, this might be also due to the fact that the two tagging conditions used in Fig. 4.11(b) and (c) are not perfectly equivalent and the one used in Fig. 4.11(c) is actually more restrictive.

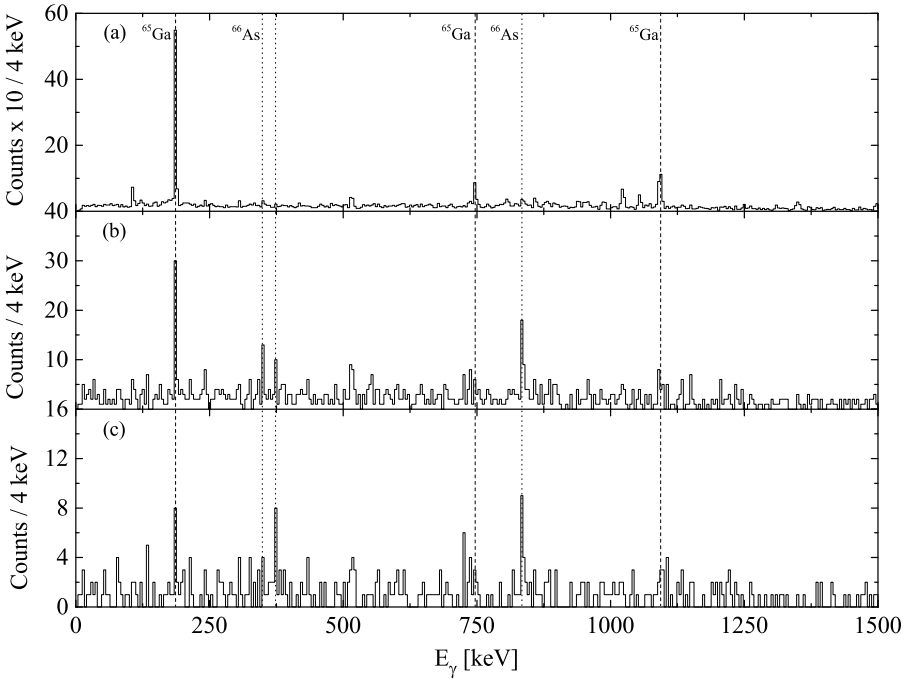

Figure 4.11: Recoil-β tagged JUROGAM II singles γ-ray spectra with 200 ms correlation time: (a) no requirement for β-particle energy, (b) a threshold energy requirement of $\sim$2 MeV was applied to the sum of the fast and slow signals and (c) 2D fast vs. slow phoswich gate was employed. The dashed lines correspond to the γ decays of excited states in ^{65}Ga, whereas the dotted lines correspond to the decays of excited states in ^{66}As.

Another source for the reduction in good events is due to β particles interacting with a large angle of incidence to the phoswich detector and therefore not passing into the slow element. One-to-one comparison with the data collected with the planar detector was not carried out since the equivalence in the β-particle energy measurement in these two data sets could not be established precisely enough. To conclude, the phoswich provides a firm identification of the high-energy β particles and thereby, it can be employed in the β-tagging experiments. However, currently it is not known if the use of a scintillator detector provides a significant increase in the β-particle detection efficiency over the planar detector. In any case, a major drawback with the phoswich is that the possibility for the detection of delayed low-energy γ rays is lost. In the future, the thickness of the fast-plastic layer could be reduced to allowing a lower hardware energy threshold, which would permit a greater variation in the tagging conditions, especially for the low-energy β threshold.

Three different DSSD tagging strategies are possible in GRAIN and two of these are known as the SINGLE and SQUARE strategies. For the SQUARE strategy, all surrounding pixels in the DSSD are considered when looking for the β decay of a recoil, whereas in the SINGLE strategy, only the implantation pixel is considered. The effect on the γ spectra of using the SINGLE and SQUARE strategies with the new highly-pixelated DSSD is shown in Fig. 4.12. The (a) panel corresponds to the SQUARE strategy, whereas the (b) panel corresponds to the SINGLE strategy. Analysis of these data shows only a small increase above background in valid ^{66}As events for the larger tagging scheme involving the neighbouring pixels alongside a significant increase in contaminant events. This demonstrates that the single pixel tagging strategy is optimal and emphasises the necessity for a reduction in pixel size in order to reduce the amount of falsely correlated events. As can be seen in Fig. 4.12(a), the increase in background for a larger effective pixel size is significant when compared to the increase in good ^{66}As events.

The effect of false correlations is investigated by considering the 191-keV peak resulting from the decay of the second excited state in ^{65}Ga. Here, an index of false correlations is defined as being the ratio between the intensity of the 191-keV line and the number of β particles included in the β gate (see section 2.4). Figure 4.13 shows this false correlation index for varying β threshold energies in the case of the new DSSD and the planar detector. The SQUARE strategy was used to simulate larger pixel size within the same experiment. For comparison there are also data included in Fig. 4.13 taken with the less finely segmented DSSDs from the high beam intensity ($I_b = 6-7$ pnA) part of the first ^{66}As experiment and from the UoYtube study, in which a lower beam intensity ($I_b = 2-3$ pnA) was used (these use SINGLE tagging strategy only). Analysis of the data from the first ^{66}As experiment was challenging due to the large amount of false correlations. The UoYtube data clearly show a reduced index of false correlations as the beam intensity used was lower, which produced lot

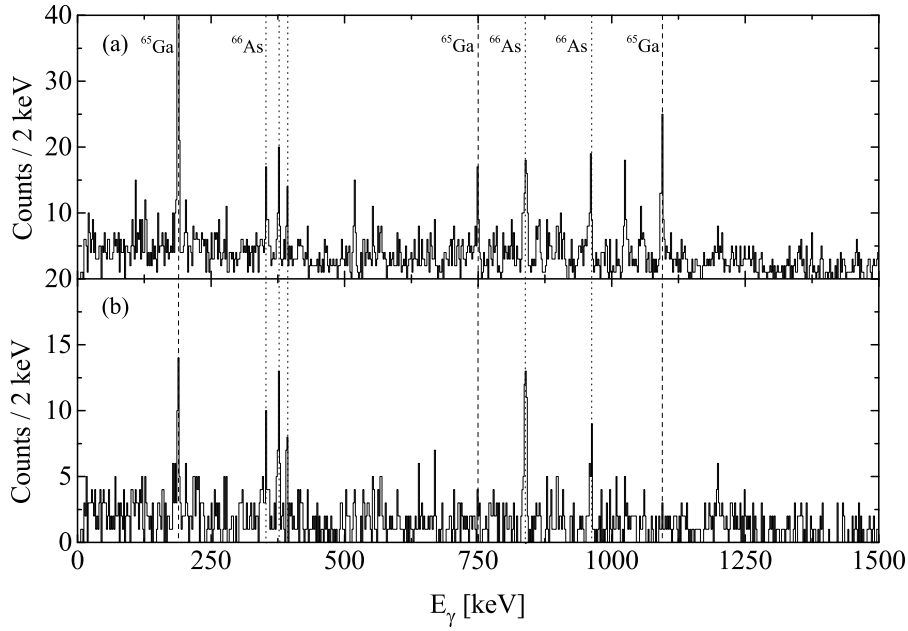

Figure 4.12: Recoil-β tagged JUROGAM II singles γ-ray spectra using the new highly-pixelated DSSD and planar germanium detector with 3.5−10-MeV β gate and 300-ms correlation time. Two different recoil-to-decay DSSD correlation strategies have been used, the top spectrum uses the SQUARE tagging strategy, whilst the bottom spectrum uses the SINGLE strategy (see text for tagging strategy definitions). While there is a slight increase in the number of genuine ^{66}As events (indicated by the dotted lines) using the SQUARE tagging strategy, it comes at the expense of a significant increase in the ^{65}Ga contaminant lines (indicated by the dashed lines).

cleaner β-tagged γ-ray spectra (see chapter 5). It can be considered that these two experiments set an upper (old DSSD with $I_b = 6-7$ pnA) and lower (old DSSD with $I_b = 2-3$ pnA) limit for a safe region, which dictates a suitable running speed.

The lowest index of false correlations is achieved with the new DSSD in the case where the low beam intensity of 3 pnA is used as illustrated in Fig. 4.13. When the beam intensity is increased to 5 pnA, the obtained index of false correlations increases accordingly. However, the highest intensity of 7 pnA, which was used in the test, does not add much to the false correlations as the curve is basically overlapping with the 5 pnA case. From this it can be verified that the new higher-pixelated DSSD can be used with a reasonably high running speed while still maintaining the index of false correlations below the

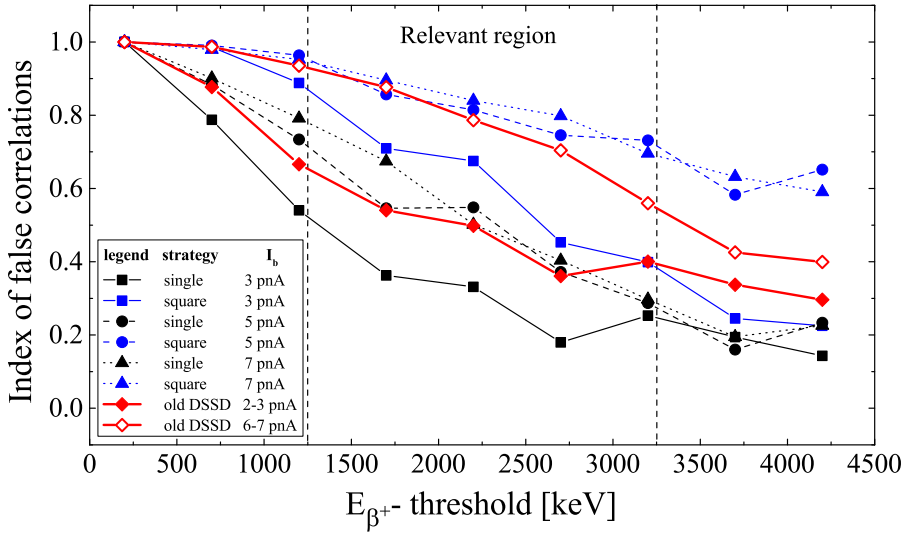

Figure 4.13: False correlation index for different tagging strategies (explained in the text) with the new DSSD (black and blue curves). Also included are data taken with the old DSSD with two different beam intensities (red curves). The higher intensity data taken with the old DSSD represents an upper limit for false correlations, whereas the lower intensity data resulted in index of false correlations, which were manageable during the analysis of the data. The highlighted relevant region represents the typical β-energy thresholds used in the RBT analysis and therefore the region in which improvements are most significant. It can be seen that the new DSSD with the SINGLE tagging strategy can manage higher beam intensities whilst maintaining manageable false correlations. Error bars are excluded for clarity.

upper limit *i.e.*, the curve corresponding to the old DSSD with $I_b = 6-7$ pnA. It can be seen, therefore, that data from the new DSSD, even at beam intensities, which would have caused problems for the less finely segmented DSSD, are not dominated by false correlations. It then seems reasonable that higher beam intensities of 5−7 pnA are practical for RBT studies with the new highly-pixelated DSSD. When the SQUARE tagging strategy is applied to the data collected with the 7 pnA intensity, the false correlations curve overlaps with the one corresponding to the old DSSD and high beam intensity as shown in Fig. 4.13. This behaviour confirms the validity of the SQUARE tagging strategy method to simulate a larger pixel size, which has been used in these comparisons.

For completeness, the cleanliness technique was applied to data obtained using the new DSSD and the planar detector for both the SINGLE and SQUARE

strategies. It was found that, as was expected that the reduction in pixel size had no significant effect on the cleanliness of genuine ^{66}Ge correlations because this background channel was not dominated by false correlations. This verifies the distinction between the two types of backgrounds considered, the falsely correlated events and those originating from genuine β decays. Finally, tests were carried out using the new DSSD along with the planar detector to investigate how the production rates responded to various beam intensities in order to help determine the optimal beam intensity for any future runs. It was found that for beam intensities between 3−7 pnA, rates increased linearly, as would be expected. This indicates that false correlation rates were not high enough at these intensities to significantly inhibit the tagging process. Strictly speaking, these conclusions are only valid for the ^{28}Si + ^{nat}Ca reaction studied here. The cross-section of the most intense reaction channel depends on the beam - target combination and thus sometimes can be even higher than the one for ^{65}Ga. This implies that the upper limit for the beam intensity may lie lower than 7 pnA in those cases. On the other hand, if the scenario is reversed, beam intensity higher than 7 pnA may be acceptable.

Chapter 5

Spectroscopy of the neutron-deficient nucleus ^{66}Se

In this chapter the experimental results regarding the study of the exotic neutron-deficient $N = Z - 2$ nucleus ^{66}Se will be presented. Candidates for three excited states in ^{66}Se have been identified using the recoil-β tagging method with improved sensitivity through the implementation of the UoYtube veto detector for charged-particle evaporation channels. Combining these results with the observation of $T = 1$ states up to $J^{\pi} = 6^{+}$ in ^{66}As, which are presented in chapter 3, allows for a comparison of the mirror and triplet energy differences across the full $A = 66$ triplet as a function of angular momentum. This constitutes the only system above ^{56}Ni for which such data presently exists at intermediate spin. The TED follow the negative trend previously observed in the $f_{7/2}$ shell [13] as a function of angular momentum. The present simplistic shell-model calculations indicate that, as in the $f_{7/2}$ shell, the Coulomb isotensor part accounts for only half of the observed trend, pointing to a continued need for an additional isospin non-conserving interaction as a function of mass. The full experimental details regarding this study are explained in sections 4.3 and 4.3.1.

5.1 Data-analysis and results

The analysis of this experimental data is based on the same ideas presented throughout this thesis so the finer details will not be repeated here. Instead, the two new ideas regarding the suppression of charged-particle evaporation channels and the focal plane delayed γ-ray veto will be discussed. To summarise, a reaction of ^{40}Ca(^{28}Si,2n)^{66}Se was used for 36 h with a beam energy of 75 MeV. The set-up was a combination of JUROGAM II + UoYtube + RITU + GREAT, which was used to identify the reaction products and their decays. The planar germanium detector was used to detect β particles and delayed γ rays. Two additional JUROGAM II clovers were installed at the RITU focal plane to increase the detection efficiency for the delayed γ rays.

5.1.1 Charged-particle veto

The identification of ^{66}Se γ rays is facilitated by its Fermi superallowed β-decay nature and by the fact that ^{66}Se is produced via 2n evaporation, while the other products involve emission of at least one charged particle. With these features in mind, a step-wise procedure was followed to search for γ rays originating from ^{66}Se. In the first instance, the RBT method was applied by correlating 0.5−10-MeV β particles to recoils within a correlation time of 106 ms, which is approximately three times the β-decay half-life of ^{66}Se reported in Ref. [93]. In addition, an area containing 20 × 20 strips at the center of the right hand side DSSD, which contained the highest counting rate per pixel (see Fig. 4.3), was not used in the tagging process. This was done to reduce the amount of randomly correlated recoil-β pairs, similar to a method first used by Joss *et al.* [94]. Figure 5.1(a) shows the observed γ rays when these tagging conditions are applied. As expected, transitions from ^{66}As are identified along with contaminants such as ^{65}Ga and ^{65}Ge corresponding to 3p and 2pn channels, respectively. Since ^{66}Se is produced via 2n evaporation, the analysis may be refined by vetoing recoils from the correlations if an associated charged particle had been detected in UoYtube. Figure 5.2 shows the energies of the UoYtube events (x axis) plotted against the time differences between recoils and UoYtube events (y axis). Here, the group of events (enclosed within the dashed red region), which have nearly constant time difference due to the well-defined flight time of recoils, are evaporated charged particles. At lower energies, the timing properties of the UoYtube elements (photodiode + CsI(Tl) crystals) deteriorate, which leads to a deviation from the constant time difference value. If the recorded recoil event preceding the β-decay event in the same pixel of the DSSD is associated with a charged-particle event falling inside the two dimensional gate, the recoil is omitted from the tagging process. Therefore, the prompt γ rays originating from this particular recoil are not tagged and thus, not incremented in the tagged γ-ray spectrum.

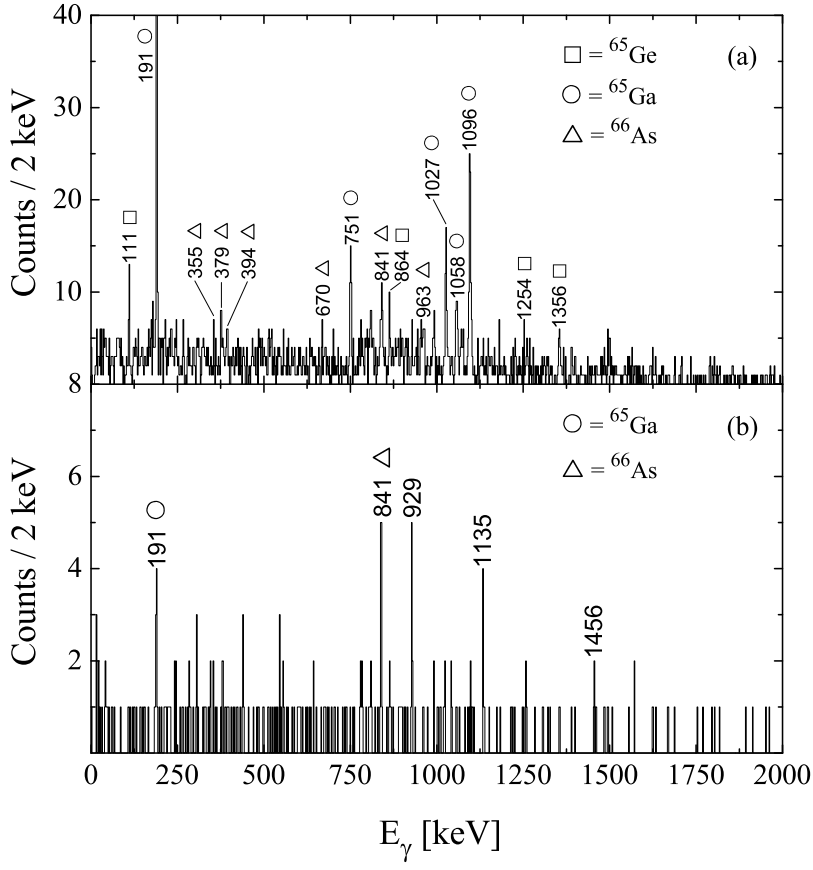

Figure 5.1: (a) Recoil-β tagged JUROGAM II singles γ-ray spectrum using 106 ms correlation time and 0.5−10-MeV β gate. (b) Same as (a) but with charged-particle suppression.

Figure 5.1(b) demonstrates how successful the vetoing process is - the suppression of charged-particle evaporation leaves five peaks at 191 keV, 841 keV, 929 keV, 1135 keV and 1456 keV, where the first two can be associated with ^{65}Ga and ^{66}As, respectively. It is possible to reduce these contaminant lines by applying an additional veto condition obtained from delayed γ-ray transitions detected at the focal plane of RITU as described in the next section.

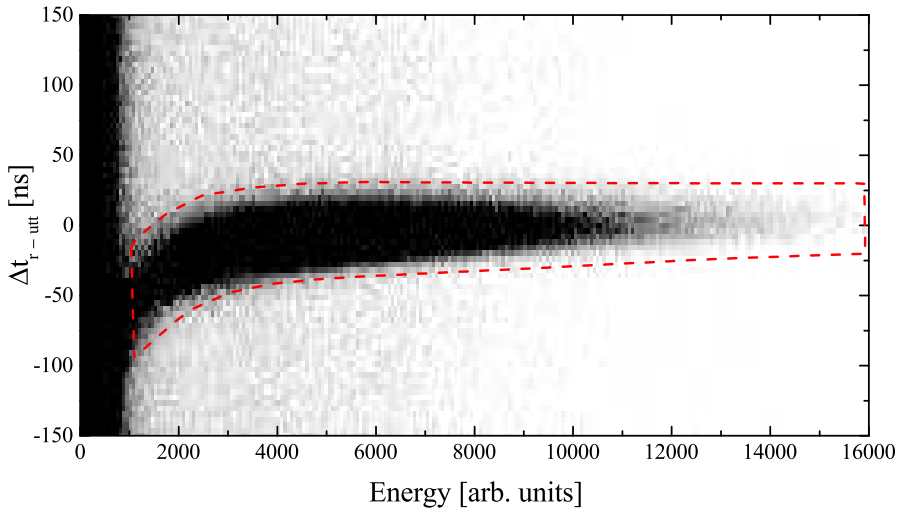

Figure 5.2: Energy of events detected in the UoYtube (x axis) against recoil-UoYtube event time difference (y axis). The dashed red region illustrates the two dimensional energy-time gate to select the charged-particle events, which will be used to veto associated recoils. See text for details of the vetoing process.

5.1.2 The delayed γ-ray veto

The γ rays, detected at the focal plane in delayed coincidence with a recoil implantation or in prompt coincidence with β decay, can be utilised as an additional veto, in similar manner as the charged particles at the target position. For example, the β decay of ^{65}Ga feeds excited states in ^{65}Zn, which are de-excited by various γ rays such as the intense 61-keV and 115-keV transitions. These γ rays are observed in the focal plane germanium detectors in prompt coincidence with the β decay with high efficiency ($\epsilon_{61\ \mathrm{keV}} = 23$ %, $\epsilon_{115\ \mathrm{keV}} = 20$ %). If at least one of these γ rays has been detected, the associated recoil event preceding the β decay is omitted from the tagging process, hence it is not correlated with the prompt γ-ray transitions in a similar manner as in the case of charged-particle veto. The 841-keV transition in Fig. 5.1(b) feeds an isomeric state in ^{66}As de-excited by a 114-keV transition, which is followed by the emission of eight other γ rays (see sections 3.2.1 and 3.2.2). In this case, if any of these nine transitions is observed in the focal plane germanium detectors, the associated ^{66}As recoil is removed from the tagging process. When all known delayed γ rays, either following a recoil or β decay, are considered, the resulting total focal plane veto efficiency is sufficiently high and results in a tagged γ-ray spectrum with three lines at 929 keV, 1135 keV and 1456 keV as shown in Fig. 5.3. The behaviour of this data was investigated in detail to rule out possible artificial effects. Firstly, it turned out that the

observed γ-ray events are distributed over the whole data volume. Moreover, they are observed in different germanium detectors. Lastly, the analysis was carried out with two different sets of JUROGAM II calibration coefficients (see section 2.2) computed from standard ^{152}Eu + ^{133}Ba calibration source data (in Fig. 5.3 these have been used) and from the measured in-beam data. In both cases almost identical tagged γ-ray spectra were obtained, which eliminates the possibility of effects induced by the false Doppler correction.

5.1.3 β-decay half-life of ^{66}Se

The half-life of the β decay events correlated to the 929-, 1135- and 1456-keV γ rays can be deduced from gated β-recoil time differences as illustrated in Fig. 5.4. Here, the gates are set on the three aforementioned transitions and the resulting time differences are plotted on a logarithmic scale. Using the method of maximum likelihood, as presented in Ref. [71], the β-decay half-life of 38^{+13}_{-8} ms is obtained from the individual decay times. The validity of this method has been tested independently in the cases of ^{199}At [95] and ^{175}Pt [96] nuclei, where the α-decay half-lives have been determined in agreement with the literature values using prompt γ rays as a selective means instead of the α-decay energy. Most importantly, the calculated standard deviation $\sigma_{\Theta_{exp}} = 1.07$ of the logarithmic β-recoil time distribution falls between the recommended lower and upper limits of $\sigma^{\text{lower}}_{\Theta_{exp}} = 0.77$ and $\sigma^{\text{upper}}_{\Theta_{exp}} = 1.75$ for 16 events [72]. This leads to the fact that the observed activity originates from the decay of one radioactive species with 90 % confidence. In addition, the derived β-decay half-life of 38^{+13}_{-8} ms is in good agreement with the literature value of 33(12) ms reported in Ref. [93]. This is a true indication that the newly observed γ rays originate from ^{66}Se.

5.2 Discussion

Recently, Obertelli *et al.,* [97] identified the 2^+ state in ^{66}Se in a study of two-nucleon removal from a secondary beam of ^{68}Se at Michigan State University. This constitutes the only definite identification of an excited 2^+, $T = 1$ state in the upper *fp* shell (although tentative transitions have been reported for ^{62}Ge [98]). The newly observed γ ray at 929(2) keV de-excites the 2^+ state in ^{66}Se, since it is consistent with the transition energy of 929(7) keV reported in Ref. [97]. The other two peaks at 1135(2) keV and 1456(2) keV are assigned to de-excite the 4^+ and 6^+ levels at 2064 keV and 3520 keV, respectively, as the observed pattern represents a typical spectrum of the strongest yrast transitions in an even-even nucleus. The relative intensities of the transitions depopulating the 2^+ [$I_{929\ \text{keV}}$=100(40)], 4^+ [$I_{1135\ \text{keV}}$=70(40)] and 6^+ [$I_{1456\ \text{keV}}$=50(30)]

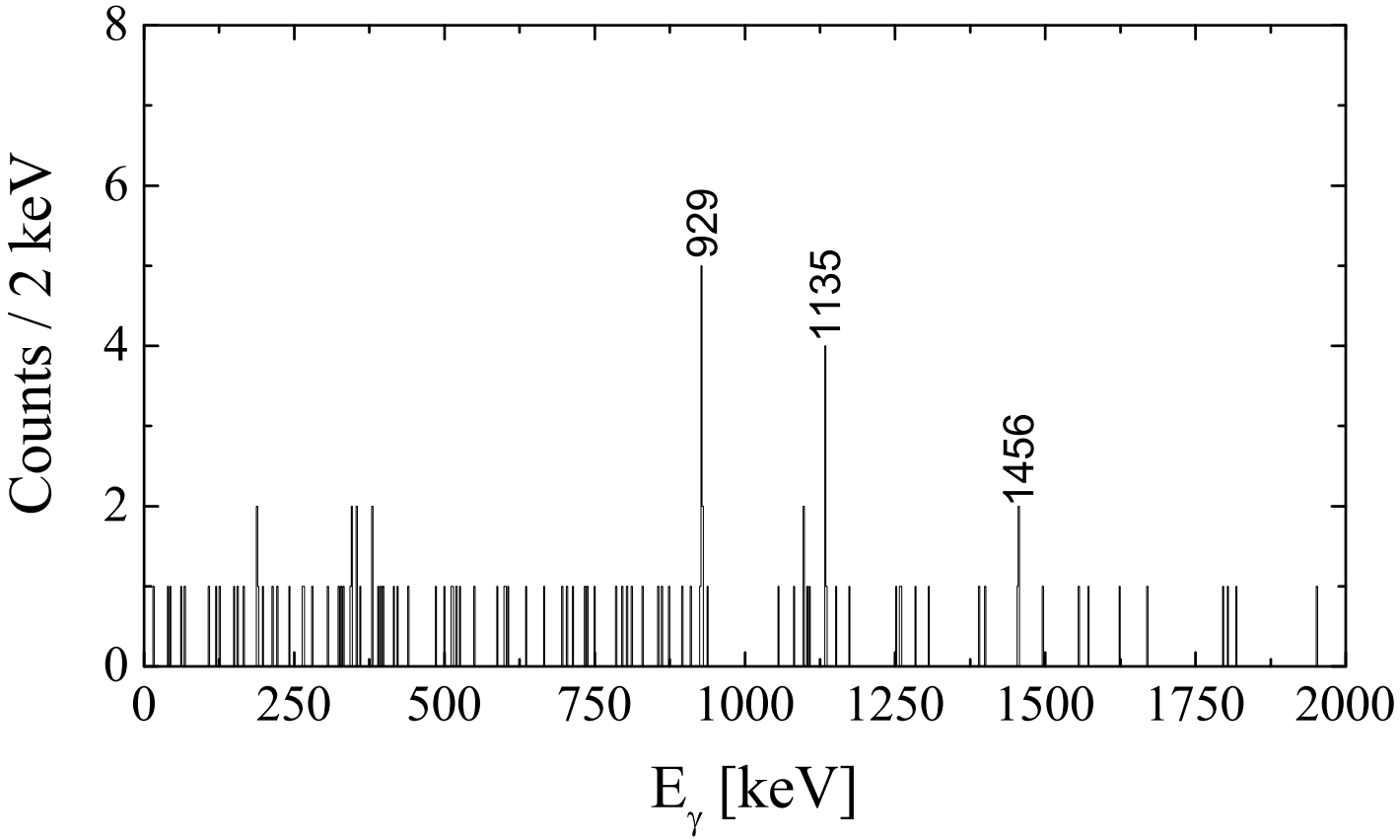

Figure 5.3: Same as Fig. 5.1(b) but with an additional veto condition obtained from delayed γ rays detected at the focal plane of RITU (see text for details).

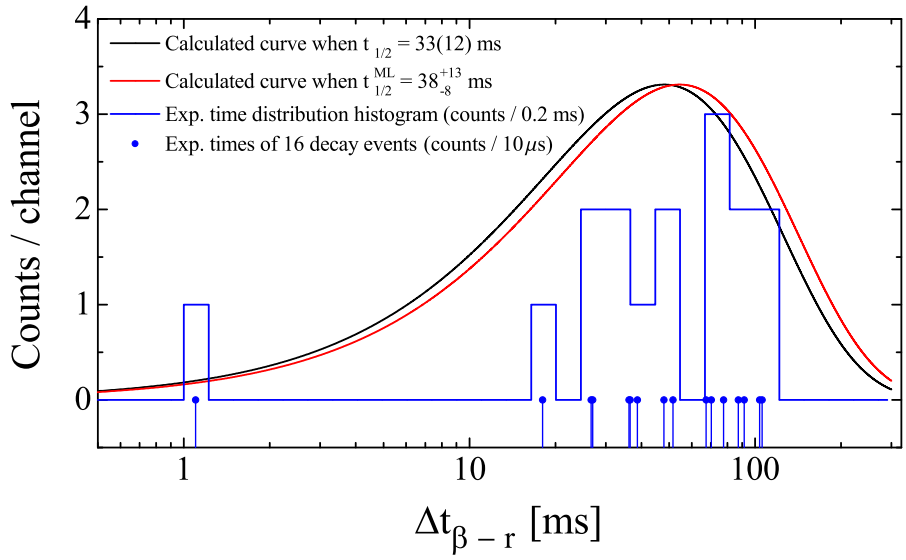

Figure 5.4: Experimental time distribution of ^{66}Se β decay (blue dots and blue histogram). The β-recoil time differences are obtained by gating on the prompt 929-, 1135- and 1456-keV γ-ray transitions. Experimental half-life value of $t_{1/2} = 38^{+13}_{-8}$ ms is extracted from the data using maximum likelihood method [71]. This value is used to generate the logarithmic decay-time curve (red), which is compared to the calculated curve (black) using literature value of $t_{1/2} = 33(12)$ ms [93].

states are very similar to the corresponding yrast cascade in ^{66}Ge [79]. However, it should be noted that in ^{66}Ge the intensities of the $6^+ \rightarrow 4^+$ (1481 keV) and $5^- \rightarrow 4^+$ (1510 keV) transitions are almost identical in addition to the fact that the 5^- state lies only 29 keV higher in excitation energy than the 6^+ state [79]. In light of this fact, the observed 1456 keV transition may originate from the 5^- state in ^{66}Se, but several facts are against this scenario. Firstly, as the γ-ray energy of 1456 keV is closer to the energy of $6^+ \rightarrow 4^+$ transition than $5^- \rightarrow 4^+$ transition in ^{66}Ge, the isospin symmetry implies a 6^+ assignment for the state at 3520 keV. Secondly, according to the systematics of Se isotopes (see Fig. 5.5), the 5^- state should remain well above the 6^+ state in excitation energy, making the population of 6^+ state more probable as it is yrast. Thirdly, the possible population of the 5^- state would imply other intensive γ-ray transitions around energies of 500 keV and 900 keV as is the case in ^{66}Ge, but clearly such transitions were not observed.

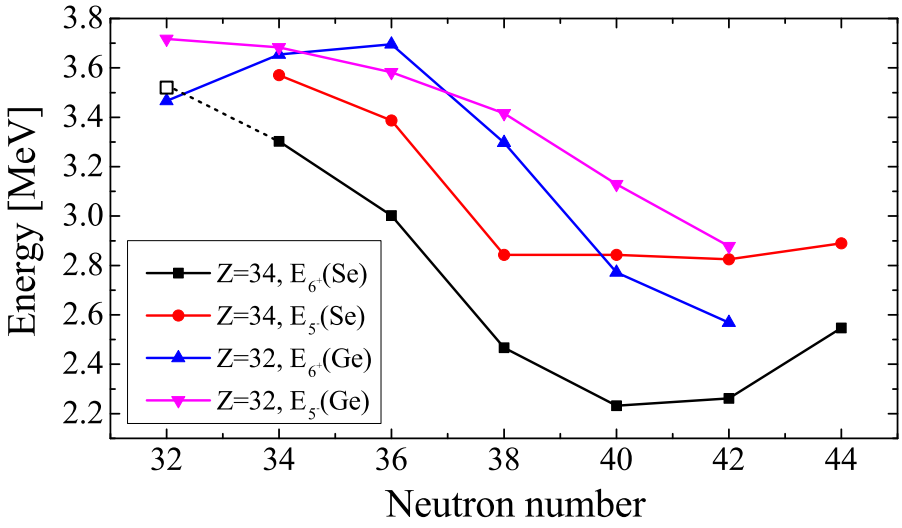

Figure 5.5: Systematics of 6^+ and 5^- level energies in light Se and Ge isotopes. The newly observed state at 3520 keV is illustrated with open square and the assignment of 6^+ is supported by the systematics together with other arguments presented in the text. Data are obtained from [58].

5.2.1 Mirror energy differences

The MED data for $A = 66$ are plotted in Fig. 5.6 along with the experimental data for nuclei in the $f_{7/2}$ shell. The MED is evaluated with Eq. 1.7. The significant variation of the MED reflects the fact they depend strongly on Coulomb multipole effects associated with recoupling the angular momenta of pairs of particles as a function of spin. Thus, the sign of the MED depends on whether it is protons or neutrons that are active in a particular member of the mirror pair. In addition, the Coulomb monopole effects (discussed in sections 1.2 and 1.4) will also contribute and again these will vary in sign from case to case. As pointed out earlier, the effect of the monopole contributions are difficult to identify without a devoted calculation, which has not been carried out for the $A = 66$ pair (^{66}Se/^{66}Ge) in this work.

In the case of the $^{42}_{22}$Ti$_{20}$/$^{42}_{20}$Ca$_{22}$ pair, the MED trend can be explained qualitatively on the basis of the Coulomb multipole term. The ^{42}Ti has two protons and ^{42}Ca has two neutrons in the $f_{7/2}$ orbital. Thereby, as the proton pair in ^{42}Ti starts to recouple their angular momenta, the Coulomb energy is decreased. The same does not happen in the ^{42}Ca, where the neutron pair is aligned and so an overall negative MED trend results. The positive kink at $J = 2$ can not be explained by this mechanism. The mirror pair $^{54}_{28}$Ni$_{26}$/$^{54}_{26}$Fe$_{28}$

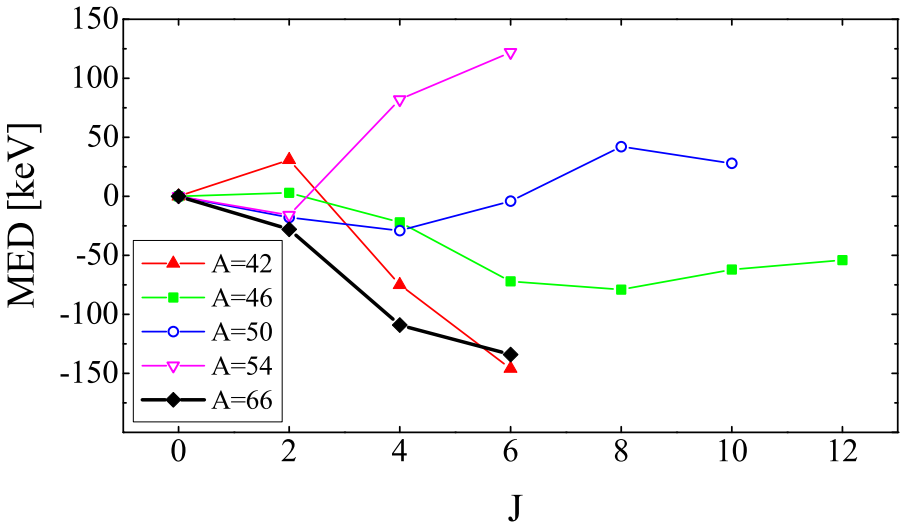

Figure 5.6: The MED for the nuclei between mass $A = 42 - 66$. Data are taken from the present work and from Refs. [99, 28, 100, 17, 101, 29, 102, 79].

are cross-conjugate partners of the ^{42}Ti/^{42}Ca pair, hence, their basic configuration is two neutron holes in ^{54}Ni and two proton holes in ^{54}Fe in the $f_{7/2}$ orbital. As it is the neutron hole pair in ^{54}Ni and the proton hole pair in ^{54}Fe, which align first, an overall positive MED trend is expected. This assumption is confirmed by the experimental data in Fig. 5.6. Again, it should be noted that the data point at $J = 2$ does not fit into this picture. In the case of the mirror pair $^{50}_{26}$Fe$_{24}$/$^{50}_{24}$Cr$_{26}$ one would expect a negative MED trend due to the aligning proton hole pair in ^{50}Fe and a neutron hole pair in ^{50}Cr. Owing to the cross-conjugate symmetry, the MED ought to be the opposite for the $^{46}_{24}$Cr$_{22}$/$^{46}_{22}$Ti$_{24}$ pair. However, as can be observed from Fig. 5.6, the alignment processes in these two mirror pairs are not that straightforward. In the $A = 50$ pair, the MED is initially negative up to spin $J = 4$ after which it turns into positive. The role of the radial term V_{Cr} is found to be important here. According to shell-model calculations in Ref. [13], the occupation of the $p_{3/2}$ orbital decreases while the occupation of the $f_{7/2}$ orbital increases when going towards higher spin. As the $f_{7/2}$ orbital has a smaller radius than the $p_{3/2}$ orbital, the Coulomb energy is increased in ^{50}Fe finally leading to a positive MED. The situation with the $^{66}_{34}$Se$_{32}$/$^{66}_{32}$Ge$_{34}$ mirror pair is clearer as two protons in ^{66}Se and two neutrons in ^{66}Ge occupy the $f_{5/2}$ orbital. Indeed, the observed MED is very similar as in the case of the $A = 42$ pair, but the magnitude is larger. It is difficult to speculate without a calculation how the monopole effects contribute here. However, it is interesting to note that there are no peculiarities with the $J = 2$ value like in the $A = 42$ and $A = 54$ pairs.

5.2.2 Triplet energy differences

The TED data for $A = 66$ are plotted in Fig. 5.7 along with the experimental data for nuclei in the $f_{7/2}$ shell. The TED are computed with Eq. 1.8. The TED are remarkably consistent in sign and, to a large extent, magnitude. This is partly associated with the fact that multipole effects will dominate the TED. Indeed, under the assumption of identical wave functions across the triplet, the monopole contributions discussed earlier would effectively cancel in the calculation of the TED. Identical wave functions is a reasonable assumption for well-bound states, although in heavier systems, there are predictions of different shape-driving effects that will destroy this symmetry [103].

The fact that the TED are negative can be explained in a simple picture when it is considered that the TED are directly dependent on the isotensor part of the two-body interaction - *i.e.,* $v^{(pp)} + v^{(nn)} - 2v^{(np)}$. The TED, thereby, depend on the difference between the np interaction and the average of the pp and nn interactions. The negative TED behaviour with spin has its origin in two separate effects. Firstly, the number of $T = 1$, np pairs, for a given analogue state, is always larger in the odd-odd $N = Z$ nucleus than in the two even-even nuclei. This has been demonstrated both analytically [5] and with shell-model calculations in the $f_{7/2}$ shell [104]. Secondly, the Coulomb isotensor interaction is positive, but reduces relative to the ground state for increasing angular momentum coupling. The combination of these two effects leads to the negative TED in all cases studied so far. However, in the $f_{7/2}$ shell, it was found that the Coulomb isotensor interaction (CM) alone was not sufficient to account for the TED magnitude [13, 15, 29]. An additional nuclear isotensor component (VB) of +100 keV for $J = 0$ couplings of $f_{7/2}$ particles was identified based on the empirical TED of the $A = 42$ triplet [15]. The inclusion of this term gave a much better description of the TED in the shell-model prescription. This is also demonstrated in Figs. 5.8(a) and (b) where the experimental and predicted TED are shown for states up to 6^+ in the $A = 46$ and $A = 54$ triplets. The shell-model results presented here have been performed using the procedure previously applied for these nuclei in Refs. [13, 15, 29] using the code ANTOINE [105] and the KB3G interaction [106]. The full *fp* space was used for $A = 46$ and for $A = 54$ and the number of excitations out of the $f_{7/2}$ shell was restricted to six. A total isotensor component of +100 keV was used, which is equivalent to making the np interaction 50 keV stronger than the average of pp and nn interactions. The results reproduced here are for completeness and comparison, and are the same as previously published for $A = 46$ [15] and $A = 54$ [13]. The inclusion of the VB term clearly leads to a better agreement with the data in these cases. For $A = 54$, Gadea *et al.,* [29] showed that a reduced isotensor component of +50 keV gave results that match the experimental data more closely. It should be emphasized that the fundamental origin of this additional INC term has not been explained and furthermore, there are no predictions for its requirement in the upper *fp* shell.

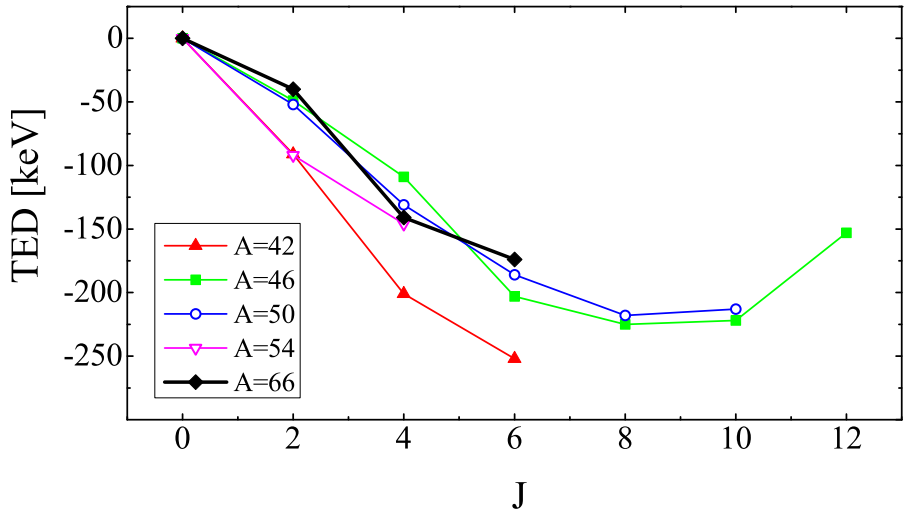

Figure 5.7: The experimental TED for the isobaric triplets between mass $A = 42 - 66$ regions. Data are taken from the present work and from Refs. ^{42}Sc [107], ^{42}Ti and ^{42}Ca [99], ^{46}V [22], ^{46}Cr [28], ^{46}Ti [100], ^{50}Mn [108], ^{50}Fe [17], ^{50}Cr [101], ^{54}Co [109], ^{54}Ni [29], ^{54}Fe [102], ^{66}As [36] and ^{66}Ge [79].

It is obvious that in the case of the $A = 66$ triplet studied here, the consistent negative TED behaviour continues, as observed in the $f_{7/2}$ shell. In addition, it appears that the CM component alone will not account for the observed TED. This is illustrated in Fig. 5.8(c), which shows a prediction of the TED for $A = 66$ assuming a Coulomb isotensor interaction alone [106]. The calculation was performed using ANTOINE in the *fp* space with KB3G and GXPF1A interactions, allowing at most five excitations from the $f_{7/2}$ and $p_{3/2}$ orbitals into the $f_{5/2}$ and $p_{1/2}$ orbitals. This should be viewed as a simplistic calculation, as it does not include the $g_{9/2}$ orbital, which is a weak point of the calculation. The VB component has not been included since, unlike in the $f_{7/2}$ shell, there is no empirical estimate of the strength available. In the case of the $A = 66$ triplet one would need to add the VB component into at least three different orbitals, namely into the $f_{5/2}$, $p_{3/2}$ and $p_{1/2}$. Furthermore, there are no solid grounds, which would dictate how the VB strength should be distributed between the above-mentioned orbitals. Nevertheless, even this simple calculation shows that the Coulomb part alone is insufficient to explain the experimental TED magnitude. It should be noted that the missing $(g_{9/2})^2$ components in the wave functions would only change the prediction for the TED by virtue of the different spin-dependent changes of the Coulomb energy for $g_{9/2}$ wave functions compared with the *fp* orbitals. It seems unlikely that this would be sufficient to account for the large TED seen at high spins.

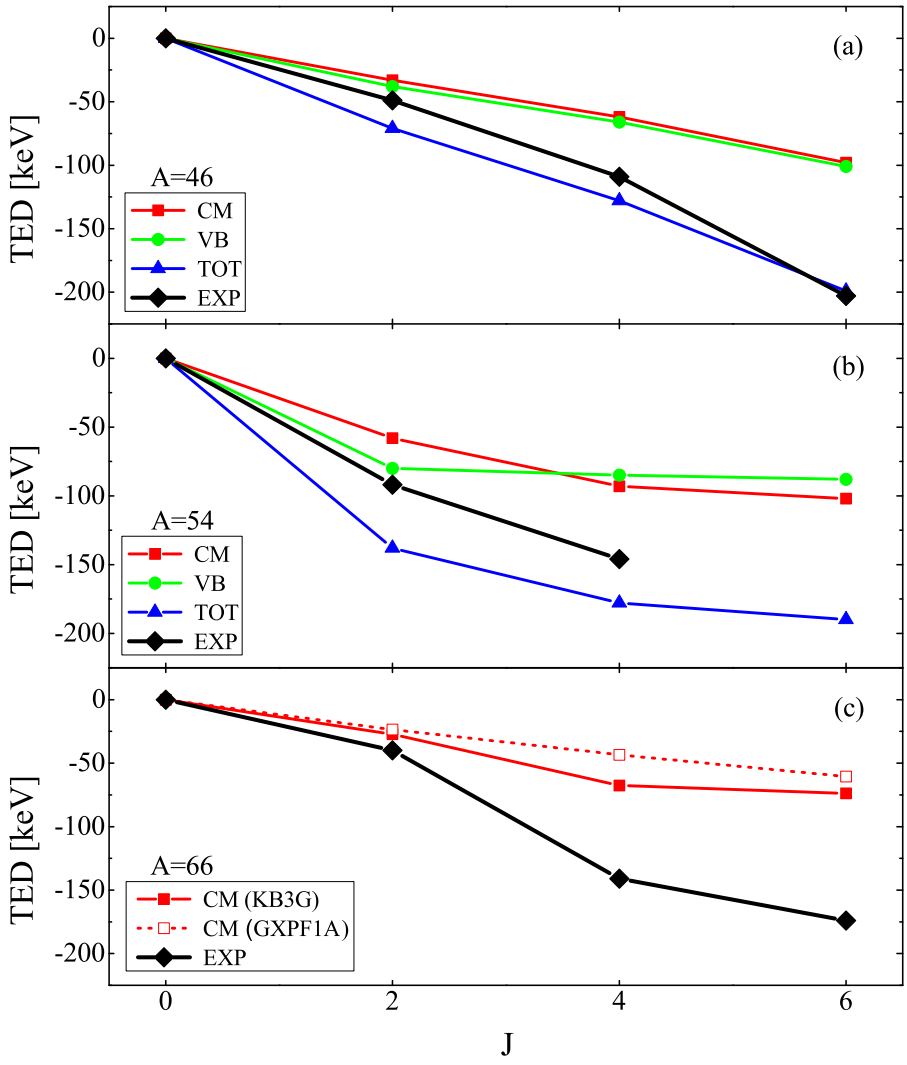

Figure 5.8: The experimental and shell-model predicted TED for (a) $A = 46$, (b) $A = 54$ and (c) $A = 66$ triplets (see text for details).

In a recent theoretical study by Kaneko *et al.,* [110] a shell-model analysis of displacement energies was performed in order to study the effect of INC nuclear forces. In particular, they considered triplet displacement energies for the ground states. In general they found that the agreement with the data was much improved in the $f_{7/2}$ shell, when the additional isotensor interaction of +165 keV for the $J = 0,\ T = 1$ coupling was introduced. It is interesting to note that the isotensor interaction used is larger than previously considered in this region. In addition, it was found in Ref. [110] that the INC forces were less important for nuclei in the upper *fp* shell, which stands in contrast with the shell-model results presented in the current study.

Other factors such as deformation effects and Thomas-Ehrman shifts, which could lead to the observed experimental TED behaviour, should be considered as well. In the calculation of TED, it can be shown that the Z dependency is removed completely from the difference in Coulomb energy terms, which reduces the importance of the deformation effects by a factor of $\sim 60-70$. This differs significantly from the calculation of CED, where the linear dependency on Z remains in the difference of Coulomb energy terms; hence, CED are more sensitive to the nuclear shape related effects, as discussed in Ref. [23], than TED. The Thomas-Ehrman shifts [25, 26] are known to be strong in the case of weakly or unbound s-orbital protons, due to the extended radial part of the proton single-particle wave function, which originates from the absence of the centrifugal barrier. This, in turn, leads to a reduced Coulomb energy as the Coulomb repulsion is attenuated between the core and the odd proton in the s-orbital [111]. However, in ^{66}Se the single-particle configurations of the excited 4^+ and 6^+ states are unlikely to be dominated by low l-orbitals; thus, the zeroth order approximation is that the Thomas-Ehrman shifts in this case ought to be small. To be exact, the amount of the Thomas-Ehrman shift in terms of energy should be quantitatively calculated in this particular case of the $A = 66$ triplet in order to verify its effect. As a final remark, the possibility of Thomas-Ehrman shifts playing a role in the observed TED trend cannot be ruled out completely, but is highly unlikely.

Chapter 6

Summary, present status and future prospects

The self-conjugate odd-odd $N = Z$ nucleus ^{66}As has been experimentally studied in detail. Prompt and delayed structures have been observed utilising recoil-β tagging and recoil-isomer tagging methods. The half-lives of two isomeric states and the internal conversion coefficients of the transitions de-exciting these levels were measured with improved accuracy yielding the experimental $B(E2)$ values. Some of the newly observed prompt γ-ray transitions were also identified in [70]. The arrangement of the transitions differs slightly between these two studies, especially within $T = 0$ structures. The level energies of the $T = 1$, 2_1^+ and 4_3^+ states are established in agreement with the ones reported in Ref. [70]. However, the candidates for the $T = 1$, 6_1^+ state differ in terms of level energy. Depending on which one of the experimental 6_1^+ energies is used, a somewhat different behaviour in the CED trend is obtained. The current work suggests a moderate and positive CED trend, which is in agreement with the theoretical shell-model prediction using the effective JUN45 interaction in the full fpg model space. Moreover, this trend can be explained on the basis of the combined effects of the Coulomb multipole interaction (positive trend as a function spin) and a electromagnetic spin-orbit interaction ϵ_{ls} (negative trend as a function of spin). Low-lying $T = 0$ states are described well by theory in terms of excitation energy when compared to the experimental counterparts. The same holds for the $T = 1$ band members.

Three new pieces of apparatus have been constructed and tested for use in conjunction with the RITU + JUROGAM II + GREAT set-up for the RBT method. These were a charged-particle veto detector UoYtube, a new highly-segmented DSSD and a phosphor-sandwich device. Tests have been performed

on these devices and their impact on the cleanliness of the RBT technique has been characterised. It is found that UoYtube makes a reduction in contaminant events to approximately 1/3 for a vetoing strategy of one charged-particle event acceptance and down to 1/22 for a strategy, which allows for no charged-particle events. The phoswich device has been tested and used in conjunction with the new DSSD. The phoswich was found to provide a firm identification of the high-energy β particles based on the pulse shape analysis. In addition, the use of a new highly-segmented DSSD has also been validated and is found to reduce the false correlations by 65 %. The effect of varying beam intensities was also investigated for the new DSSD, allowing for beam intensities to be selected in order to optimise for both cleanliness and event rates. A complete RBT setup is therefore ready for use, with significantly improved cleanliness over the original set-up used in the study of ^{66}As.

Owing to the development work described above, excited states in the exotic neutron-deficient nucleus ^{66}Se have been identified using the recoil-β tagging method in conjunction with the charged-particle veto device UoYtube. This data allowed the TED across the full $A = 66$ triplet to be examined for the first time and constitutes the heaviest case where the TED are currently known. The observed TED mirrors the negative trend of the triplets in the $f_{7/2}$ shell. Shell-model calculations in the present work reveal that the Coulomb isotensor component alone is insufficient to account for the experimental TED, pointing to a need for an additional nuclear isospin INC interaction, whose origin is not clear. A need for an additional INC interaction has been previously demonstrated for the triplets in the $f_{7/2}$ shell. The current study necessitates that further experimental and especially theoretical studies are undertaken, which could clarify the origin of the missing TED magnitude.

The newly obtained results with the charged-particle suppression were very encouraging, but during the ^{66}Se experiment, some design flaws with UoYtube were identified. This led into a revised design and building of UoYtube II. One of the most obvious issues was the 5 mm gaps between the crystals causing unnecessary losses in the charged-particle detection efficiency. Secondly, the detection efficiency especially at forward angles needed to be increased as the evaporated particles are forward focused (see Fig. 4.7). Thirdly, the target holding mechanism had to be simple and quick in order to allow for fast installation of the ^{nat}Ca target (as it oxidizes rapidly) and maintain the correct alignment upon a target change. In addition, the LISA chamber was found to be unsuitable for the β-tagging purposes as it is gratuitously large and its operation *i.e.,* aligning, closing/opening and vacuum pumping is time consuming. This meant that a completely new target chamber was needed as well. The design criteria for the new target chamber were that it allows the use of the full JUROGAM II array, the coupling to the beam line and RITU would remain identical as in the case of the standard target chamber and it allows for the maximum flexibility in the new UoYtube design and operation. The obvious starting point was the

design of the existing JUROGAM chamber, which was only slightly modified. The new chamber, called the *"Jackpot"* after its chief designer Jack Henderson, has identical dimensions with the standard chamber, but is made out of steel. This allowed the electrical D-connector feedthroughs for the UoYtube signals to be welded on to the side of the chamber. It should be noted, however, that the material choice is not optimal for the γ-ray detection efficiency, which is slightly reduced according to recent measurements [112]. The UoYtube design was modified in such a way that the length/bore radius ratio was increased to enhance the angular coverage. Moreover, end caps with 6 pentagon-shaped crystals were added to both ends of the tube to increase the charged-particle detection efficiency at extreme angles. The tube splits in to two parts, which fulfills the requirements placed for the target holding mechanism. Figure 6.1 shows the photograph of UoYtube II and the end caps are shown in Fig. 6.2.

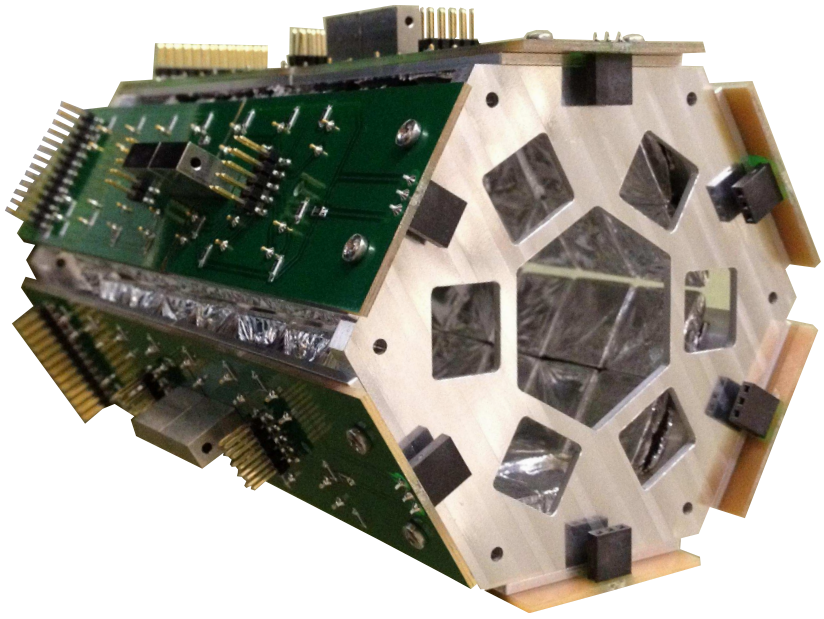

Figure 6.1: Photograph of UoYtube II. Three improvements in the design were made: 1. The 5 mm gaps between each crystal were removed, 2. the bore diameter was reduced to increase angular coverage at forward angles and 3. end caps with 6 pentagon-shaped crystals were added to each end of the tube (see Fig. 6.2). The total number of crystals in the new design is still 96.

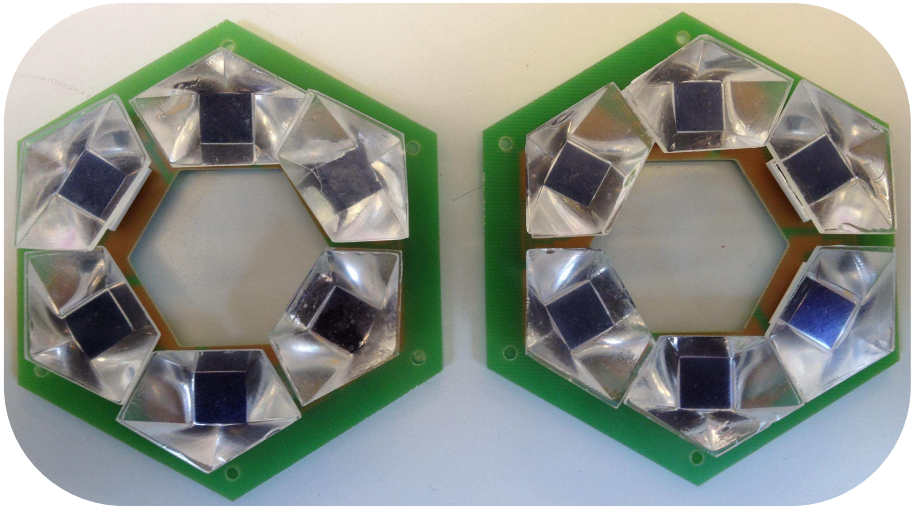

Figure 6.2: Photograph of the UoYtube II endcaps to increase the charged-particle detection efficiency especially at forward, but also at backward angles.

UoYtube II, housed by the new chamber, was in action for the first time in March 2013 together with the phoswich and the highly-segmented DSSD detectors. The aim was to identify excited states in the exotic neutron-deficient nucleus ^{70}Kr using the ^{40}Ca(^{32}S,2n)^{70}Kr reaction. However, like several times before, an unknown heavy contaminant was present in the ^{32}S beam making the clean separation of recoils impossible. For this reason, the beam was changed to ^{36}Ar to populate excited states in ^{74}Sr via the ^{40}Ca(^{36}Ar,2n)^{74}Sr reaction. Here, the separation between the primary beam/other unwanted reaction products and the recoils was clearly better and permitted a successful experiment. The analysis of this data is presently in progress, but the preliminary results are very promising as illustrated in Fig. 6.3 (courtesy of J. Henderson). The candidates for the $2^+ \rightarrow 0^+$ and $4^+ \rightarrow 2^+$ transitions in ^{74}Sr have been identified and are highlighted with dashed lines in Fig. 6.3(b), where the charged-particle veto in addition to the β tagging conditions has been employed.

Soon after the successful ^{74}Sr experiment, UoYtube was employed to study ^{113}Ba through a ^{58}Ni(^{58}Ni,3n)^{113}Ba reaction. One of the strongest evaporation channels was 1p2n leading into ^{113}Cs, which is a proton emitter with a 17 μs half-life. This allowed the precise measurement of the UoYtube detection efficiency for one proton yielding a value of 75 %. This corresponds to more than a 10 % increase in the dection efficiency for one charged particle in comparison to the original design. The calculated detection probability is 98 % for the 3p channel *i.e,* that at least one of the three evaporated protons is detected.

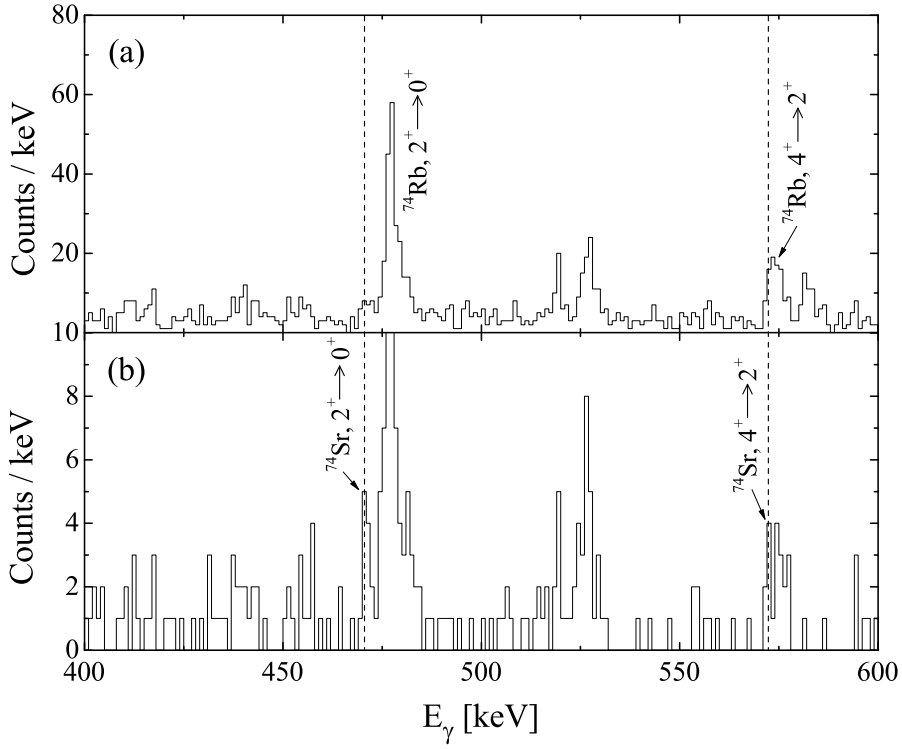

Figure 6.3: (a) Recoil β-tagged JUROGAM II γ-ray transitions from a ^{36}Ar + ^{nat}Ca reaction with a 150 ms correlation time. (b) Same as (a) but with charged-particle veto. The dashed lines illustrate the candidates for $2^+ \rightarrow 0^+$ and $4^+ \rightarrow 2^+$ transitions in ^{74}Sr. These results are preliminary as the analysis is still in progress [113].

Progress has been made on the theoretical front as well. Very recently, shell-model predictions for the MED and TED using the JUN45 interaction and full fpg model space in the case of the $A = 66$, $A = 70$, $A = 74$ and $A = 78$ triplets have been performed by K. Kaneko *et. al.,* [114]. These results and conclusions are very similar to those obtained with the simplistic shell-model calculation discussed in section 5.2.2. The recent calculations have investigated the separate effects of the multipole, monopole and spin-orbit terms (ϵ_{ll} and ϵ_{ls}) and the result is that the sum of these is not enough to reproduce the experimental MED and TED data within the $A = 66$ triplet, hence, an additional INC term is needed. Moreover, like previous theoretical investigations have shown in the $f_{7/2}$ shell [15], the experimental MED is reproduced by the theory if an additional isovector INC interaction especially for the $J = 2$, $T = 1$ coupling

is introduced. This is the so called $J = 2$ anomaly described in Ref. [13]. The assumption made earlier about the unimportance of the monopole effects in TED is supported by the recent calculation as both the ϵ_{ll} and ϵ_{ls} terms are nearly zero within the $A = 66$ and $A = 70$ triplets. Unfortunately, there is still no explanation for the origin of the INC term so it remains as an open question.

In the very near future, the peculiar contamination of the ^{32}S beam will be investigated together with the cyclotron group. As stated earlier, the origin of the contamination is not fully understood, but in principle the beam may contain other components if these happen to have the same charge-to-mass ratio as the beam. Therefore, different charge states for the ^{32}S will be examined in order to change its charge-to-mass ratio and consequently suppress the heavy component. If these tests are successful and sufficient recoil separation can be achieved, the study of ^{70}Kr will probably be performed fairly soon.

It goes without saying that the whole RBT collaboration is impatiently waiting for the commissioning of the new vacuum-mode recoil separator MARA. While preparing this thesis, the main component of MARA *i.e.,* the electric dipole is under construction at Danfysik, Denmark. The research station housing MARA is already built and the magnetic components are aligned and installed. The research program planned for MARA widely covers the same physics interests as discussed in this thesis, hence, the experimental studies will be mainly focused on the area around the $N = Z$ line up to ^{112}Ba. If the study of ^{70}Kr fails again with the RITU set-up, that will be one of the first nuclei in line to be studied with MARA. What makes the ^{70}Kr such an interesting object to investigate is the highly unusual negative CED trend observed in the ^{70}Br/^{70}Se pair. Moreover, refering to the recent advances on the theoretical front, for once we have a prediction for the TED trend in the case of the full $A = 70$ triplet, thus, the experimental data would set these state-of-the-art shell-model calculations to a strict test. Another novel approach would be to combine the life-time measurements carried out with the JYFL plunger [115] with the recoil-β tagging method. One interesting case would be the life-time measurement of the 3_2^+ state in ^{66}As as it is claimed to be isomeric (see section 3.3.2). In general, the quadrupole moments and the B($E2$) transition strengths computed from the life-time data would provide very interesting nuclear structure information as it does not yet exist at all in this region. Currently the schedule is such that MARA focal plane decay experiments will start in 2014, whereas the full in-beam experiments may take place in 2015 at the earliest [116]. These experiments will open up a new interesting era both for the Accelerator Laboratory of the University of Jyväskylä and experimental nuclear physics in general.

Bibliography

[1] J. Erler, N. Birge, M. Kortelainen, W. Nazarewicz, E. Olsen, A. M. Perhac and M. Stoitsov, "*The limits of nuclear landscape.*", *Nature* **486** (2012) 509.

[2] B. Cederwall *et al.*, "*Evidence for a spin-aligned neutronproton paired phase from the level structure of* ^{92}Pd.", *Nature* **469** (2011) 68.

[3] B. S. Nara Singh *et al.*, "16^+ *Spin-Gap Isomer in* ^{96}Cd.", *Phys. Rev. Lett.* **107** (2011) 172502.

[4] A. V. Afanasjev and S. Frauendorf, "*Description of rotating* $N = Z$ *nuclei in terms of isovector pairing.*", *Phys. Rev. C* **71** (2005) 064318.

[5] J. Engel, K. Langanke and P. Vogel, "*Pairing and isospin symmetry in proton-rich nuclei.*", *Phys. Lett. B* **389** (1996) 211.

[6] D. G. Jenkins *et al.*, "$T = 0$ *and* $T = 1$ *states in the odd-odd* $N = Z$ *nucleus,* $^{70}_{35}Br_{35}$.", *Phys. Rev. C* **65** (2002) 064307.

[7] M. Hasegawa, K. Kaneko, T. Mizusaki and Y. Sund, "*Phase transition in exotic nuclei along the* $N = Z$ *line.*", *Phys. Lett. B* **656** (2007) 51.

[8] J. Hardy and I. Towner, "*Superallowed* $0^+ \to 0^+$ *nuclear* β *decays: A critical survey with tests of the conserved vector current hypothesis and the standard model.*", *Phys. Rev. C* **71** (2004) 055501.

[9] H. Schatz, A. Aprahamian, J. Görres, M. Wiescher, T. Rauscher, J. Rembges, F.-K. Thielemann, B. Pfeiffer, P. Möller, K.-L. Kratz, H. Herndl, B. Brown and H. Rebel, "*rp-process nucleosynthesis at extreme temperature and density conditions.*", *Phys. Rep.* **294** (1998) 167.

[10] P. Ennis, C. Lister, W. Gelletly, H. Price, B. Varley, P. Butler, T. Hoare, S. Ćwiok and W. Nazarewicz, "*Triaxiality and isospin-forbidden E1 decays in the* $N = Z$ *nucleus* ^{64}Ge.", *Nucl. Phys. A* **535** (1991) 392.

[11] G. Coló, M. A. Nagarajan, P. V. Isacker and A. Vitturi, "*Isospin mixing in proton-rich $N \cong Z$ nuclei.*", *Phys. Rev. C* **52** (1995) R1175.

[12] M. Honma, T. Otsuka, T. Mizusaki and M. Hjorth-Jensen, "*New effective interaction for f_5pg_9-shell nuclei.*", *Phys. Rev. C* **80** (2009) 064323.

[13] M. A. Bentley and S. M. Lenzi, "*Coulomb energy differences between high-spin states in isobaric multiplets.*", *Prog. Part. Nucl. Phys.* **59** (2007) 497.

[14] E. Caurier, G. Martínez-Pinedo, F. Nowacki, A. Poves and A. P. Zuker, "*The shell model as a unified view of nuclear structure.*", *Rev. Modern Phys.* **77** (2005) 427.

[15] A. P. Zuker, S. M. Lenzi, G. Martínez-Pinedo and A. Poves, "*Isobaric Multiplet Yrast Energies and Isospin Nonconserving Forces.*", *Phys. Rev. Lett.* **89** (2002) 142502.

[16] K. Kaneko, T. Mizusaki, Y. Sun, S. Tazaki and G. de Angelis, "*Coulomb Energy Difference as a Probe of Isospin-Symmetry Breaking in the Upper fp-Shell Nuclei.*", *Phys. Rev. Lett.* **109** (2012) 092504.

[17] S. M. Lenzi, N. Mărginean, D. R. Napoli, C. A. Ur, A. P. Zuker, G. de Angelis, A. Algora, M. Axiotis, D. Bazzacco, N. Belcari, M. A. Bentley, P. G. Bizzeti, A. Bizzeti-Sona, F. Brandolini, P. von Brentano, D. Bucurescu, J. A. Cameron, C. Chandler, M. De Poli, A. Dewald, H. Eberth, E. Farnea, A. Gadea, J. Garces-Narro, W. Gelletly, H. Grawe, R. Isocrate, D. T. Joss, C. A. Kalfas, T. Klug, T. Lampman, S. Lunardi, T. Martínez, G. Martínez-Pinedo, R. Menegazzo, J. Nyberg, Z. Podolyak, A. Poves, R. V. Ribas, C. Rossi Alvarez, B. Rubio, J. Sánchez-Solano, P. Spolaore, T. Steinhardt, O. Thelen, D. Tonev, A. Vitturi, W. von Oertzen and M. Weiszflog, "*Coulomb Energy Differences in $T = 1$ Mirror Rotational Bands in ^{50}Fe and ^{50}Cr.*", *Phys. Rev. Lett.* **87** (2001) 122501.

[18] J. Duflo and A. P. Zuker, "*Mirror displacement energies and neutron skins.*", *Phys. Rev. C* **66** (2002) 051304(R).

[19] J. A. Nolen and J. P. Schiffer, "*Coulomb energies.*", *Annu. Rev. Nucl. Sci.* **19** (1969) 471.

[20] R. F. Casten, *Nuclear Structure from a Simple Perspective*, Oxford University Press Inc., New York, 2000.

[21] K. S. Krane, *Introductory nuclear physics*, John Wiley & Sons, Inc., United States, 1988.

[22] P. E. Garrett, W. E. Ormand, D. Appelbe, R. W. Bauer, J. A. Becker, L. A. Bernstein, J. A. Cameron, M. P. Carpenter, R. V. F. Janssens, C. J. Lister, D. Seweryniak, E. Tavukcu and D. D. Warner, "*Observation of ^{46}Cr and Testing the Isobaric Multiplet Mass Equation at High Spin.*", *Phys. Rev. Lett.* **87** (2001) 132502.

[23] B. S. Nara Singh, A. N. Steer, D. G. Jenkins, R. Wadsworth, M. A. Bentley, P. J. Davies, R. Glover, N. S. Pattabiraman, C. J. Lister, T. Grahn, P. T. Greenlees, P. Jones, R. Julin, S. Juutinen, M. Leino, M. Nyman, J. Pakarinen, P. Rahkila, J. Sarén, C. Scholey, J. Sorri, J. Uusitalo, P. A. Butler, M. Dimmock, D. T. Joss, J. Thomson, B. Cederwall, B. Hadinia and M. Sandzelius, "*Coulomb shifts and shape changes in the mass 70 region.*", *Phys. Rev. C* **75** (2007) 061301(R).

[24] W. E. Ormand and B. A. Brown, "*Empirical isospin-nonconserving Hamiltonians for shell-model calculations.*", *Nucl. Phys. A* **491** (1989) 1.

[25] J. B. Ehrman, "*On the Displacement of Corresponding Energy Levels of* ^{13}C *and* ^{13}N.", *Phys. Rev.* **81** (1951) 412.

[26] R. G. Thomas, "*An Analysis of the Energy Levels of the Mirror Nuclei,* ^{13}C *and* ^{13}N.", *Phys. Rev.* **88** (1952) 1109.

[27] D. G. Jenkins *et al.*, "*γ-ray spectroscopy of the $A = 23$, $T = 1/2$ nuclei* ^{23}Na *and* ^{23}Mg*: High-spin states, mirror symmetry, and applications to nuclear astrophysical reaction rates.*", *Phys. Rev. C* **87** (2013) 064301.

[28] P. E. Garrett, S. M. Lenzi, E. Algin, D. Appelbe, R. W. Bauer, J. A. Becker, L. A. Bernstein, J. A. Cameron, M. P. Carpenter, R. V. F. Janssens, C. J. Lister, D. Seweryniak and D. D. Warner, "*Spectroscopy of the $N = Z - 2$ nucleus* ^{46}Cr *and mirror energy differences.*", *Phys. Rev. C* **75** (2007) 014307.

[29] A. Gadea, S. M. Lenzi, S. Lunardi, N. Mărginean, A. P. Zuker, G. de Angelis, M. Axiotis, T. Martínez, D. R. Napoli, E. Farnea, R. Menegazzo, P. Pavan, C. A. Ur, D. Bazzacco, R. Venturelli, P. Kleinheinz, P. Bednarczyk, D. Curien, O. Dorvaux, J. Nyberg, H. Grawe, M. Górska, M. Palacz, K. Lagergren, L. Milechina, J. Ekman, D. Rudolph, C. Andreoiu, M. A. Bentley, W. Gelletly, B. Rubio, A. Algora, E. Nacher, L. Caballero, M. Trotta and M. Moszyński, "*Observation of* ^{54}Ni*: Cross-Conjugate Symmetry in $f_{7/2}$ Mirror Energy Differences.*", *Phys. Rev. Lett.* **97** (2006) 152501.

[30] K.-H. Schmidt, R. Simon, J.-G. Keller, F. Hessberger, G. Münzenberg, B. Quint, H.-G. Clerc, W. Schwab, U. Gollerthan and C.-C. Sahm, "*Gamma-Spectroscopic investigations in the radiative fusion reaction* $^{90}Zr + {}^{90}Zr$.", *Phys. Lett. B* **168** (1986) 39.

[31] E. S. Paul, P. J. Woods, T. Davinson, R. D. Page, P. J. Sellin, C. W. Beausang, R. M. Clark, R. A. Cunningham, S. A. Forbes, D. B. Fossan, A. Gizon, J. Gizon, K. Hauschild, I. M. Hibbert, A. N. James, D. R. LaFosse, I. Lazarus, H. Schnare, J. Simpson, R. Wadsworth and M. P.

Waring, "*In-beam γ-ray spectroscopy above ^{100}Sn using the new technique of recoil decay tagging.*", *Phys. Rev. C* **51** (1995) 78.

[32] D. M. Cullen, N. Amzal, A. J. Boston, P. A. Butler, A. Keenan, E. S. Paul, H. C. Scraggs, A. M. Bruce, C. M. Parry, J. F. C. Cocks, K. Helariutta, P. M. Jones, R. Julin, S. Juutinen, H. Kankaanpää, H. Kettunen, P. Kuusiniemi, M. Leino, M. Muikku and A. Savelius, "*Identification of the $K^{\pi}=8^{-}$ rotational band in ^{138}Gd.*", *Phys. Rev. C* **58** (1998) 846.

[33] C. Scholey, D. M. Cullen, E. S. Paul, A. J. Boston, P. A. Butler, T. Enqvist, C. Fox, H. C. Scraggs, S. L. Shepherd, O. Stezowski, A. M. Bruce, P. M. Walker, M. Caamaño, J. Garcés Narro, M. A. Bentley, D. T. Joss, O. Dorvaux, P. T. Greenlees, K. Helariutta, P. M. Jones, R. Julin, S. Juutinen, H. Kankaanpää, H. Kettunen, P. Kuusiniemi, M. Leino, M. Muikku, P. Nieminen, P. Rahkila and J. Uusitalo, "*Recoil isomer tagging in the proton-rich odd-odd $N = 77$ isotones, $^{142}_{65}Tb$ and $^{144}_{67}Ho$.*", *Phys. Rev. C* **63** (2001) 034321.

[34] A. Steer, D. Jenkins, R. Glover, B. N. Singh, N. Pattabiraman, R. Wadsworth, S. Eeckhaudt, T. Grahn, P. Greenlees, P. Jones, R. Julin, S. Juutinen, M. Leino, M. Nyman, J. Pakarinen, P. Rahkila, J. Sarén, C. Scholey, J. Sorri, J. Uusitalo, P. Butler, I. Darby, R.-D. Herzberg, D. Joss, R. Page, J. Thomson, R. Lemmon, J. Simpson and B. Blank, "*Recoil-beta tagging: A novel technique for studying proton-drip-line nuclei.*", *Nucl. Instrum. Methods Phys. Res. A* **565** (2006) 630.

[35] J. Henderson, P. Ruotsalainen, D. Jenkins, C. Scholey, K. Auranen, P. Davies, T. Grahn, P. Greenlees, T. Henry, A. Herzáň, U. Jakobsson, P. Joshi, R. Julin, S. Juutinen, J. Konki, M. Leino, G. Lotay, A. Nichols, A. Obertelli, J. Pakarinen, J. Partanen, P. Peura, P. Rahkila, M. Sandzelius, J. Sarén, J. Sorri, S. Stolze, J. Uusitalo and R. Wadsworth, "*Enhancing the sensitivity of recoil-beta tagging.*", *J. Inst.* **8** (2013) P04025.

[36] P. Ruotsalainen, C. Scholey, R. Julin, K. Hauschild, K. Kaneko, R. Wadsworth, D. Jenkins, B. N. Singh, T. Brock, P. Greenlees, J. Henderson, U. Jakobsson, P. Jones, S. Juutinen, S. Ketelhut, M. Leino, N. Lumley, P. Mason, P. Nieminen, M. Nyman, I. Paterson, P. Peura, M. Procter, P. Rahkila, J. Sarén, J. Sorri and J. Uusitalo, "*Recoil-β tagging study of the $N = Z$ nucleus ^{66}As.*", *Phys. Rev. C* **88** (2013) 024320.

[37] V. Toivanen, Ph.D. thesis, University of Jyväskylä (2013).

[38] G. Duchêne, F. Beck, P. Twin, G. de France, D. Curien, L. Han, C. Beausang, M. Bentley, P. Nolan and J. Simpson, "*The Clover: a new generation of composite Ge detectors.*", *Nucl. Instrum. Methods Phys. Res. A* **432** (1999) 90.

[39] C. Beausang, S. Forbes, P. Fallon, P. Nolan, P. Twin, J. Mo, J. Lisle, M. Bentley, J. Simpson, F. Beck, D. Curien, G. deFrance, G. Duchêne and D. Popescu, "*Measurements on prototype Ge and BGO detectors for the Eurogam array.*", *Nucl. Instrum. Methods Phys. Res. A* **313** (1992) 37.

[40] C. Rossi Alvarez, "*The GASP array.*", *Nuclear Physics News* **3** (1993) 10.

[41] P. Rahkila, private communication.

[42] D. C. Radford, "*ESCL8R and LEVIT8R: Software for interactive graphical analysis of HPGe coincidence data sets.*", *Nucl. Instrum. Methods Phys. Res. A* **361** (1995) 297.

[43] M. Leino, J. Äystö, T. Enqvist, P. Heikkinen, A. Jokinen, M. Nurmia, A. Ostrowski, W. Trzaska, J. Uusitalo, K. Eskola, P. Armbruster and V. Ninov, "*Gas-filled recoil separator for studies of heavy elements.*", *Nucl. Instrum. Methods Phys. Res. B* **99** (1995) 653.

[44] J. Sarén, J. Uusitalo, M. Leino and J. Sorri, "*Absolute transmission and separation properties of the gas-filled recoil separator RITU.*", *Nucl. Instrum. Methods Phys. Res. A* **654** (2011) 508.

[45] J. Sarén, Ph.D. thesis, University of Jyväskylä (2011).

[46] R. Page, A. Andreyev, D. Appelbe, P. Butler, S. Freeman, P. Greenlees, R.-D. Herzberg, D. Jenkins, G. Jones, P. Jones, D. Joss, R. Julin, H. Kettunen, M. Leino, P. Rahkila, P. Regan, J. Simpson, J. Uusitalo, S. Vincent and R. Wadsworth, "*The GREAT spectrometer.*", *Nucl. Instrum. Methods Phys. Res. B* **204** (2003) 634.

[47] S. Agostinelli *et al.*, "*Geant4 – a simulation toolkit.*", *Nucl. Instrum. Methods Phys. Res. A* **506** (2003) 250.

[48] J. Allison *et al.*, "*Geant4 Developments and Applications.*", *IEEE Trans. Nucl. Sci.* **53** (2006) 270.

[49] K. Hauschild, private communication.

[50] I. Lazarus, D. Appelbe, P. Butler, P. Coleman-Smith, J. Cresswell, S. Freeman, R. Herzberg, I. Hibbert, D. Joss, S. Letts, R. Page, V. Pucknell, P. Regan, J. Sampson, J. Simpson, J. Thornhill and R. Wadsworth, "*The GREAT triggerless total data readout method.*", *IEEE Trans. Nucl. Sci.* **48** (2001) 567.

[51] P. Rahkila, "*Grain – A Java data analysis system for Total Data Readout.*", *Nucl. Instrum. Methods Phys. Res. A* **595** (2008) 637.

[52] D. C. Radford, "*Background subtraction from in-beam HPGe coincidence data sets.*", *Nucl. Instrum. Methods Phys. Res. A* **361** (1995) 306.

[53] L. Arnold, R. Baumann, E. Chambit, M. Filliger, C. Fuchs, C. Kieber, D. Klein, P. Medina, C. Parisel, M. Richer, C. Santos and C. Weber, "*TNT digital pulse precessor.*", *IEEE Trans. Nucl. Sci.* **53** (2006) 723.

[54] J. Pakarinen, Ph.D. thesis, University of Jyväskylä (2005).

[55] A. Georgiev, W. Gast and R. Lieder, "*An analog-to-digital conversion based on a moving window deconvolution.*", *IEEE Trans. Nucl. Sci.* **41** (1994) 1116.

[56] S. Eeckhaudt, Ph.D. thesis, University of Jyväskylä (2006).

[57] A. Gavron, "*Statistical model calculations in heavy ion reactions.*", *Phys. Rev. C* **21** (1980) 230.

[58] "*National Nuclear Data Center*", http://www.nndc.bnl.gov/ (2013).

[59] R. H. Burch Jr, C. A. Gagliardi and R. E. Tribble, "*Lifetimes of $N = Z$ nuclei ^{66}As and ^{70}Br.*", *Phys. Rev. C* **38** (1988) 1365.

[60] D. E. Alburger, "*Half-lives of ^{62}Ga, ^{66}As, and ^{70}Br.*", *Phys. Rev. C* **18** (1978) 1875.

[61] M. J. López Jiménez, B. Blank, M. Chartier, S. Czajkowski, P. Dessagne, G. de France, J. Giovinazzo, D. Karamanis, M. Lewitowicz, V. Maslov, C. Miehé, P. H. Regan, M. Stanoiu and M. Wiescher, "*Half-life measurements of proton-rich ^{78}Kr fragments.*", *Phys. Rev. C* **66** (2002) 025803.

[62] C. N. Davids, "*New isotopes of interest to explosive nucleosynthesis.*", *IEEE Trans. Nucl. Sci.* **26** (1979) 1191.

[63] W. E. Ormand, "*Mapping the proton drip line up to $A = 70$.*", *Phys. Rev. C* **55** (1997) 2407.

[64] T. Yamazaki, "*Tables of coefficients for angular distribution of gamma rays from aligned nuclei.*", *Nucl. Data A* **3** (1967) 1.

[65] E. Der Mateosian and A. Sunyar, "*Tables of attenuation coefficients for angular distribution of gamma rays from partially aligned nuclei.*", *Atomic Data and Nuclear Data Tables* **13** (1974) 391.

[66] S. Törmänen, Ph.D. thesis, University of Jyväskylä (1996).

[67] S. Juutinen, E. Mäkelä, R. Julin, M. Piiparinen, S. Törmänen, A. Virtanen, E. Adamides, A. Ataç, J. Blomqvist, B. Cederwall, C. Fahlander, E. Ideguchi, A. Johnson, W. Karczmarczyk, J. Kownacki, S. Mitarai, L.-O. Norlin, J. Nyberg, R. Schubart, D. Seweryniak and G. Sletten, "*Coexistence of collective and quasiparticle structures in ^{106}Sn and ^{108}Sn.*", *Nucl. Phys. A* **617** (1997) 74.

[68] U. Jakobsson, J. Uusitalo, S. Juutinen, M. Leino, T. Enqvist, P. T. Greenlees, K. Hauschild, P. Jones, R. Julin, S. Ketelhut, P. Kuusiniemi, M. Nyman, P. Peura, P. Rahkila, P. Ruotsalainen, J. Sarén, C. Scholey and J. Sorri, "*Recoil-decay tagging study of* ^{205}*Fr.*", *Phys. Rev. C* **85** (2012) 014309.

[69] R. Grzywacz, S. Andriamonje, B. Blank, F. Boué, S. Czajkowski, F. Davi, R. D. Moral, C. Donzaud, J. Dufour, A. Fleury, H. Grawe, A. Grewe, A. Heinz, Z. Janas, A. Junghans, M. Karny, M. Lewitowicz, A. Musquére, M. Pfützner, M.-G. Porquet, M. Pravikoff, J.-E. Sauvestre and K. Sümmerer, "*Isomeric states in* ^{66}*As.*", *Phys. Lett. B* **429** (1998) 247.

[70] G. de Angelis, K. T. Wiedemann, T. Martinez, R. Orlandi, A. Petrovici, E. Sahin, J. J. Valiente-Dobón, D. Tonev, S. Lunardi, B. S. Nara Singh, R. Wadsworth, A. Gadea, K. Kaneko, P. G. Bizzeti, A. M. Bizzeti-Sona, B. Blank, A. Bracco, M. P. Carpenter, C. J. Chiara, E. Farnea, A. Gottardo, J. P. Greene, S. M. Lenzi, S. Leoni, C. J. Lister, D. Mengoni, D. R. Napoli, O. L. Pechenaya, F. Recchia, W. Reviol, D. G. Sarantites, D. Seweryniak, C. A. Ur and S. Zhu, "*Shape isomerism and shape coexistence effects on the Coulomb energy differences in the* $N = Z$ *nucleus* ^{66}*As and neighboring* $T = 1$ *multiplets.*", *Phys. Rev. C* **85** (2012) 034320.

[71] K.-H. Schmidt, C.-C. Sahm and H.-G. C. K. Pielenz, "*Some Remarks on the Error Analysis in the Case of Poor Statistics.*", *Z. Phys. A* **316** (1984) 19.

[72] K. H. Schmidt, "*A new test for random events of an exponential distribution.*", *Eur. Phys. J. A* **8** (2000) 141.

[73] R. Grzywacz, C. Yu, Z. Janas, S. Paul, J. Batchelder, C. Bingham, T. Ginter, C. Gross, J. McConnell, M. Lipoglavšek, A. Piechaczek, D. Radford, J. Ressler, K. Rykaczewski, J. Shergur, W. Walters, E. Zganjar, C. Baktash, M. Carpenter, R. Janssens, C. Svensson, J. Waddington, D. Ward and E. Dragulescu, "*In-beam study of the* $N = Z$ *nucleus* $^{66}_{33}As_{33}$ *using the decay tagging technique.*", *Nucl. Phys. A* **682** (2001) 41c.

[74] M. R. Bhat and J. K. Tuli, "*Nuclear Data Sheets for A = 69*", *Nucl. Data Sheets* **90** (2000) 269.

[75] E. Browne and J. K. Tuli, "*Nuclear Data Sheets for A = 65*", *Nucl. Data Sheets* **111** (2010) 2425.

[76] T. Kibédi, T. Burrows, M. Trzhaskovskaya, P. Davidson and C. Nestor Jr., "*Evaluation of theoretical conversion coefficients using BrIcc.*", *Nucl. Instrum. Methods Phys. Res. A* **589** (2008) 202.

[77] A. Andreyev, P. Butler, R. Page, D. Appelbe, G. Jones, D. Joss, R.-D. Herzberg, P. Regan, J. Simpson and R. Wadsworth, "*GEANT Monte Carlo simulations for the GREAT spectrometer.*", *Nucl. Instrum. Methods Phys. Res. A* **533** (2004) 422.

[78] M. Hasegawa, Y. Sun, K. Kaneko and T. Mizusaki, "*Structure of isomeric states in ^{66}As and ^{67}As.*", *Phys. Lett. B* **617** (2005) 150.

[79] E. A. Stefanova, I. Stefanescu, G. de Angelis, D. Curien, J. Eberth, E. Farnea, A. Gadea, G. Gersch, A. Jungclaus, K. P. Lieb, T. Martinez, R. Schwengner, T. Steinhardt, O. Thelen, D. Weisshaar and R. Wyss, "*Four-quasiparticle alignments in ^{66}Ge.*", *Phys. Rev. C* **67** (2003) 054319.

[80] R. Orlandi, G. de Angelis, P. G. Bizzeti, S. Lunardi, A. Gadea, A. M. Bizzeti-Sona, A. Bracco, F. Brandolini, M. P. Carpenter, C. J. Chiara, F. Della Vedova, E. Farnea, J. P. Greene, S. M. Lenzi, S. Leoni, C. J. Lister, N. Mărginean, D. Mengoni, D. R. Napoli, B. S. Nara Singh, O. L. Pechenaya, F. Recchia, W. Reviol, E. Sahin, D. G. Sarantites, D. Seweryniak, D. Tonev, C. A. Ur, J. J. Valiente-Dobón, R. Wadsworth, K. T. Wiedemann and S. Zhu, "*Coherent Contributions to Isospin Mixing in the Mirror Pair ^{67}As and ^{67}Se.*", *Phys. Rev. Lett.* **103** (2009) 052501.

[81] D. Rudolph, C. Baktash, C. J. Gross, W. Satula, R. Wyss, I. Birriel, M. Devlin, H.-Q. Jin, D. R. LaFosse, F. Lerma, J. X. Saladin, D. G. Sarantites, G. N. Sylvan, S. L. Tabor, D. F. Winchell, V. Q. Wood and C. H. Yu, "*Systematics of even-even $T_z = 1$ nuclei in the $A = 80$ region: High-spin rotational bands in ^{74}Kr, ^{78}Sr, and ^{82}Zr.*", *Phys. Rev. C* **56(1)** (1997) 98.

[82] G. de Angelis, T. Martinez, A. Gadea, N. Marginean, E. Farnea, E. Maglione, S. Lenzi, W. Gelletly, C. Ur, D. Napoli, T. Kroell, S. Lunardi, B. Rubio, M. Axiotis, D. Bazzacco, A. Bizzeti Sona, P. Bizzeti, P. Bednarczyk, A. Bracco, F. Brandolini, F. Camera, D. Curien, M. D. Poli, O. Dorvaux, J. Eberth, H. Grawe, R. Menegazzo, G. Nardelli, J. Nyberg, P. Pavan, B. Quintana, C. Rossi Alvarez, P. Spolaore, T. Steinhart, I. Stefanescu, O. Thelen and R. Venturelli, "*Coulomb energy differences between isobaric analogue states in ^{70}Br and ^{70}Se.*", *Eur. Phys. J. A* **12** (2001) 51.

[83] G. Rainovski, H. Schnare, R. Schwengner, C. Plettner, L. Käubler, F. Dönau, I. Ragnarsson, J. Eberth, T. Steinhardt, O. Thelen, M. Hausmann, A. Jungclaus, K. P. Lieb, A. Müller, G. de Angelis, A. Gadea, D. R. Napoli, A. Algora, D. G. Jenkins, R. Wadsworth, A. Wilson, W. Andrejtscheff and V. I. Dimitrov, "*Shape coexistence at high spin in the $N = Z + 2$ nucleus ^{70}Se.*", *J. Phys. G: Nucl. Part. Phys.* **28** (2002) 2617.

[84] F. Johnston-Theasby, A. V. Afanasjev, C. Andreoiu, R. A. E. Austin, M. P. Carpenter, D. Dashdorj, S. J. Freeman, P. E. Garrett, J. Greene, A. Görgen, D. G. Jenkins, P. Joshi, A. O. Macchiavelli, F. Moore, G. Mukherjee, W. Reviol, D. Sarantites, D. Seweryniak, M. B. Smith, C. E. Svensson, J. J. Valiente-Dobón, R. Wadsworth and D. Ward, "*Deformation of rotational structures in ^{73}Kr and ^{74}Rb: Probing the additivity principle at triaxial shapes.*", *Phys. Rev. C* **78** (2008) 034312.

[85] A. F. Lisetskiy, R. V. Jolos, N. Pietralla and P. von Brentano, "*Quasideuteron configurations in odd-odd $N = Z$ nuclei.*", *Phys. Rev. C* **60** (1999) 064310.

[86] A. Schmidt, I. Schneider, C. Frießner, A. F. Lisetskiy, N. Pietralla, T. Sebe, T. Otsuka and P. von Brentano, "*Low spin structure of the $N = Z$ odd-odd nucleus $^{50}_{25}Mn_{25}$.*", *Phys. Rev. C* **62** (2000) 044319.

[87] R. Lüttke, E. A. McCutchan, V. Werner, K. Aleksandrova, S. Atwater, H. Ai, R. J. Casperson, R. F. Casten, A. Heinz, A. F. Mertz, J. Qian, B. Shoraka, J. R. Terry, E. Williams and R. Winkler, "*Collectivity in ^{66}Ge and ^{68}Ge via lifetime measurements.*", *Phys. Rev. C* **85** (2012) 017301.

[88] J. Sarén, J. Uusitalo, M. Leino, P. Greenlees, U. Jakobsson, P. Jones, R. Julin, S. Juutinen, S. Ketelhut, M. Nyman, P. Peura, P. Rahkila, C. Scholey and J. Sorri, "*The new vacuum-mode recoil separator MARA at JYFL.*", *Nucl. Instrum. Methods Phys. Res. B* **266** (2008) 4196.

[89] P. Ruotsalainen, Master's thesis, University of Jyväskylä (2007).

[90] M. Bantel, R. Stokstad, Y. Chan, S. Wald and P. Countryman, "*A two-dimensional position-sensitive phoswich detector.*", *Nucl. Instrum. Methods Phys. Res.* **226** (1984) 394.

[91] F. Lidén, J. Nyberg, A. Johnson and A. Kerek, "*Identification of charged particles using plastic phoswich detectors.*", *Nucl. Instrum. Methods Phys. Res. A* **253** (1987) 305.

[92] D. O'Donnell, "*Light Ion Spectrometer Array.*", *http://ns.ph.liv.ac.uk/∼dod/LISA/home.html* (2013).

[93] B. Blank, "*Studies with one- and two-proton drip line nuclei.*", *Eur. Phys. J. A* **15** (2002) 121.

[94] D. Joss, S. King, R. Page, J. Simpson, A. Keenan, N. Amzal, T. Bck, M. Bentley, B. Cederwall, J. Cocks, D. Cullen, P. Greenlees, K. Helariutta, P. Jones, R. Julin, S. Juutinen, H. Kankaanp, H. Kettunen, P. Kusiniemi, M. Leino, M. Muikku, A. Savelius, J. Uusitalo and S. Williams, "*Identification of excited states in ^{167}Os and ^{168}Os: shape coexistence at extreme neutron deficiency*", *Nucl. Phys. A* **689** (2001) 631.

[95] K. Auranen, private communication.

[96] P. Peura, private communication.

[97] A. Obertelli, T. Baugher, D. Bazin, S. Boissinot, J.-P. Delaroche, A. Dijon, F. Flavigny, A. Gade, M. Girod, T. Glasmacher, G. Grinyer, W. Korten, J. Ljungvall, S. McDaniel, A. Ratkiewicz, B. Sulignano, P. V. Isacker and D. Weisshaar, "*First spectroscopy of* ^{66}*Se and* ^{65}*As: Investigating shape coexistence beyond the* $N = Z$ *line.*", *Phys. Lett. B* **701** (2011) 417.

[98] D. Rudolph, E. Johansson, L.-L. Andersson, J. Ekman, C. Fahlander and R. du Rietz, "*Exotic Decay Modes in Rotating Nuclei.*", *Nucl. Phys. A* **752** (2005) 241c.

[99] P. Endt and C. Van Der Leun, "*Energy levels of* $A = 2144$ *nuclei (VI).*", *Nucl. Phys. A* **310** (1978) 1.

[100] F. Brandolini, J. R. B. Oliveira, N. H. Medina, R. V. Ribas, J. Sanchez-Solano, D. Bucurescu, S. M. Lenzi, C. A. Ur, D. Bazzacco, M. De Poli, E. Farnea, A. Gadea, N. Mărginean and C. Rossi-Alvarez, "*Electromagnetic transitions and structure of* ^{46}*Ti.*", *Phys. Rev. C* **70** (2004) 034302.

[101] F. Brandolini, J. Sanchez-Solano, S. M. Lenzi, N. H. Medina, A. Poves, C. A. Ur, D. Bazzacco, G. De Angelis, M. De Poli, E. Farnea, A. Gadea, D. R. Napoli and C. Rossi-Alvarez, "*Bands and Coulomb effects in* ^{50}*Cr.*", *Phys. Rev. C* **66** (2002) 021302(R).

[102] D. Rudolph, C. Baktash, M. Brinkman, M. Devlin, H.-Q. Jin, D. LaFosse, L. Riedinger, D. Sarantites and C.-H. Yu, "*High-spin shell-model states near* ^{56}*Ni.*", *Eur. Phys. J. A* **4** (1999) 115.

[103] A. Petrovici, K. W. Schmid and A. Faessler, "*Microscopic description of the mirror nuclei* ^{70}*Se and* ^{70}*Kr.*", *Nucl. Phys. A* **728** (2003) 396414.

[104] S. M. Lenzi, D. R. Napoli, C. A. Ur, D. Bazzacco, F. Brandolini, J. A. Cameron, E. Caurier, G. de Angelis, M. De Poli, E. Farnea, A. Gadea, S. Hankonen, S. Lunardi, G. Martínez-Pinedo, Z. Podolyak, A. Poves, C. Rossi Alvarez, J. Sánchez-Solano and H. Somacal, "*Band termination in the* $N = Z$ *odd-odd nucleus* ^{46}*V.*", *Phys. Rev. C* **60** (1999) 021303.

[105] F. Nowacki and E. Caurier, "*Shell Model and Nuclear Structure Far from Stability.*", *Acta Phys. Pol.* **30** (1999) 749.

[106] M. A. Bentley, private communication.

[107] C. J. Chiara, M. Devlin, E. Ideguchi, D. R. LaFosse, F. Lerma, W. Reviol, S. K. Ryu, D. G. Sarantites, O. L. Pechenaya, C. Baktash, A. Galindo-Uribarri, M. P. Carpenter, R. V. F. Janssens, T. Lauritsen, C. J. Lister, P. Reiter, D. Seweryniak, P. Fallon, A. Görgen, A. O. Macchiavelli,

D. Rudolph, G. Stoitcheva and W. E. Ormand, "*Probing $sd - fp$ cross-shell interactions via terminating configurations in $^{42,43}Sc$.*", *Phys. Rev. C* **75** (2007) 054305.

[108] C. O'Leary, M. Bentley, S. Lenzi, G. Martínez-Pinedo, D. Warner, A. Bruce, J. Cameron, M. Carpenter, C. Davids, P. Fallon, L. Frankland, W. Gelletly, R. Janssens, D. Joss, C. Lister, P. Regan, P. Reiter, B. Rubio, D. Seweryniak, C. Svensson, S. Vincent and S. Williams, "*Isovector pairing in oddodd $N = Z$ ^{50}Mn.*", *Phys. Lett. B* **525** (2002) 49.

[109] D. Rudolph, L.-L. Andersson, R. Bengtsson, J. Ekman, O. Erten, C. Fahlander, E. K. Johansson, I. Ragnarsson, C. Andreoiu, M. A. Bentley, M. P. Carpenter, R. J. Charity, R. M. Clark, P. Fallon, A. O. Macchiavelli, W. Reviol, D. G. Sarantites, D. Seweryniak, C. E. Svensson and S. J. Williams, "*Isospin and deformation studies in the odd-odd $N = Z$ nucleus ^{54}Co.*", *Phys. Rev. C* **82** (2010) 054309.

[110] K. Kaneko, Y. Sun, T. Mizusaki and S. Tazaki, "*Variation in Displacement Energies Due to Isospin-Nonconserving Forces.*", *Phys. Rev. Lett.* **110** (2013) 172505.

[111] N. Auerbach and N. V. Mau, "*About Coulomb energy shifts in halo nuclei*", *Phys. Rev. C* **63** (2000) 017301.

[112] P. Greenlees, private communication.

[113] J. Henderson, private communication.

[114] K. Kaneko, Y. Sun, T. Mizusaki and S. Tazaki, "*Isospin nonconserving interaction in the $T = 1$ analogue states of mass-70 region.*", (2013), submitted Phys. Rev. Lett.

[115] M. Taylor, D. Cullen, A. Smith, A. McFarlane, V. Twist, G. Alharshan, M. Procter, T. Braunroth, A. Dewald, E. Ellinger, C. Fransen, P. Butler, M. Scheck, D. Joss, B. Saygi, C. McPeake, T. Grahn, P. Greenlees, U. Jakobsson, P. Jones, R. Julin, S. Juutinen, S. Ketelhut, M. Leino, P. Nieminen, J. Pakarinen, P. Peura, P. Rahkila, P. Ruotsalainen, M. Sandzelius, J. Sarén, C. Scholey, J. Sorri, S. Stolze and J. Uusitalo, "*A new differentially pumped plunger device to measure excited-state lifetimes in proton emitting nuclei.*", *Nucl. Instrum. Methods Phys. Res. A* **707** (2013) 143.

[116] J. Uusitalo, private communication.